

**Doppler Radar Observation of the Evolution  
of Downdrafts in Convective Clouds**

by  
Nehzat Motallebi

Department of Atmospheric Science  
Colorado State University  
Fort Collins, Colorado



**Department of  
Atmospheric Science**

Paper No. 355

DOPPLER-RADAR OBSERVATION OF THE EVOLUTION  
OF DOWNDRAFTS IN CONVECTIVE CLOUDS

by

Nehzat Motallebi

Research supported by the

National Science Foundation  
under Grant ATM76-83361

and

National Aeronautics and Space Administration  
under Grant NSG-5011

Department of Atmospheric Science  
Colorado State University  
Fort Collins, Colorado  
Fall 1982

Atmospheric Science Paper No. 355

## ABSTRACT

### DOPPLER-RADAR OBSERVATION OF THE EVOLUTION OF DOWNDRAFTS IN CONVECTIVE CLOUDS

A detailed analysis of the 20 July 1977 thunderstorm complex which formed and evolved over the South Park region in Central Colorado is presented. This storm, extensively analyzed using multiple Doppler radar and surface mesonet data, developed within an environment having very weak wind shear. In this environment of weak flow, the storm owed its intensification to the strength of the downdraft, which was nearly coincident with the region where the cloud had grown. Some of the noteworthy features of this storm were its motion well to the right of the cloud-level winds, its multicellular nature and discrete propagation, its north-south orientation, and its relatively large storm size and high reflectivity factor (55 dBZ).

The following scenario accounts for the observed mesoscale and cloud-scale event. During stage I, a line of convergence was generated at the interface between the easterly upslope winds and westerly winds. During stage II, the convergence line subsequently propagated down the slopes of the Mosquito Range, and was the main forcing mechanism for the development of updraft on the west flank of the storm. The formation of downdraft on the eastern side of updraft blocked surface inflow, and created a detectable gust front. During stage III, as the original downdraft intensified, the accumulation of evaporatively-chilled air caused the intensification of the mesohigh, which likely destroyed the

earlier convergence line and created a stronger convergence line to the east, which forced up-lifting of the moist, westerly inflow and caused the formation of updraft to the east. It is concluded that an organized downdraft circulation, apparently maintained by precipitation drag and evaporational cooling, was responsible in sustaining a well-defined gust front. The storm attained its highest intensity as a consequence of merging with a neighboring cloud. The interaction of downdrafts or gust fronts from two intense cells appeared to be the primary mechanism of this merging process as suggested by Simpson et al. (1980). Likewise, the merging process coincided with more rain than occurred in unmerged echoes.

Nehzat Motallebi  
Department of Atmospheric Science  
Colorado State University  
Fort Collins, Colorado 80523  
Fall, 1982

## ACKNOWLEDGMENTS

I would like to thank Dr. William R. Cotton for his support and manuscript review. I am also grateful to Mr. Ray L. McAnelly for numerous discussions. Thanks are also extended to Dr. Wayne Schubert and Dr. Gerald Taylor for their helpful suggestions, and to Mr. Carl Mohr (NCAR) for his programming assistance.

The efforts of Mahmood Sitarian, Brenda Thompson and Barbara Brumit in the preparation of the manuscript and of Judy Sorbie in the drafting of the figures are greatly appreciated.

This research was sponsored by National Science Foundation (NSF) under Grant ATM76-83361, and by the National Aeronautics and Space Administration (NASA) under Grant NSG-5011. Computer time was provided by the National Center for Atmospheric Research computing facility which is sponsored by NSF.

## TABLE OF CONTENTS

	Page No.
ABSTRACT . . . . .	iii
ACKNOWLEDGMENT . . . . .	v
1. INTRODUCTION . . . . .	1
2. BACKGROUND . . . . .	5
3. INSTRUMENTATION, ANALYSIS TECHNIQUE AND ERRORS . . . . .	22
3.1 Instrumentation . . . . .	22
3.2 Background on Radar and Doppler Radar . . . . .	26
3.3 Multiple Doppler Radar Analysis . . . . .	33
3.4 Nonrandom, Systematic Errors . . . . .	38
3.5 Method of Analysis . . . . .	41
4. CASE STUDY DESCRIPTION . . . . .	44
4.1 Synoptic Situation on 20 July 1977 . . . . .	44
4.2 Mesoscale Soundings . . . . .	48
4.3 General Echo Characteristics . . . . .	58
4.4 Overview of Storm and Mesoscale Surface Features. . . . .	62
5. STORM-SCALE ANALYSIS AND RESULTS . . . . .	76
5.1 Evolution of Reflectivity and Flow Fields . . . . .	76
5.2 Structure of the Updrafts, downdrafts, and- Divergence . . . . .	82
5.3 Precipitation Efficiency . . . . .	102
5.4 Conceptual Models . . . . .	107
5.5 Vorticity Structure . . . . .	112
6. SUMMARY AND CONCLUSION . . . . .	118
REFERENCES . . . . .	122
APPENDIX A . . . . .	132
APPENDIX B . . . . .	136

## 1. INTRODUCTION

The South Park Area Cumulus Experiment (SPACE) of Colorado State University (CSU) was a comprehensive summertime meteorological program. The field portion of the program was carried out in and east of South Park, Colorado as indicated in Fig. 1.1. The South Park scale is roughly 70 km square. The area is relatively flat and averages about 2.9 km MSL. To the northeast and southeast of South Park, the eastern slopes of the Front Range drop sharply towards the High Plains interface at about 1.6 km MSL, into the South Platte and Arkansas River valleys, respectively. Directly east of the Park, however, the Palmer Lake Divide, a broad, partially wooded ridge, extends another 100 km onto the High Plains, with elevations of up to 2.1 km MSL. The western edge of South Park, on the slopes of the Mosquito Range, has been recognized as a frequent genesis region for cumulus and cumulonimbus clouds. Cumulus clouds are initiated either directly over mountain ridges by induced ridge/valley solenoidal circulation, or indirectly over the flat region by convergent zones set up by the complex flow over mountainous terrain. The South Park experiment was designed to investigate the structure of mountain-generated convective clouds and their interaction with orographically-induced mesoscale systems. A second objective of the SPACE was to examine the impact of mountain-convective clouds upon convective precipitation over the High Plains of the U.S. Throughout the month-long experiment (from 10 July to 13 August), a variety of convective clouds were observed, ranging from lightly precipitating

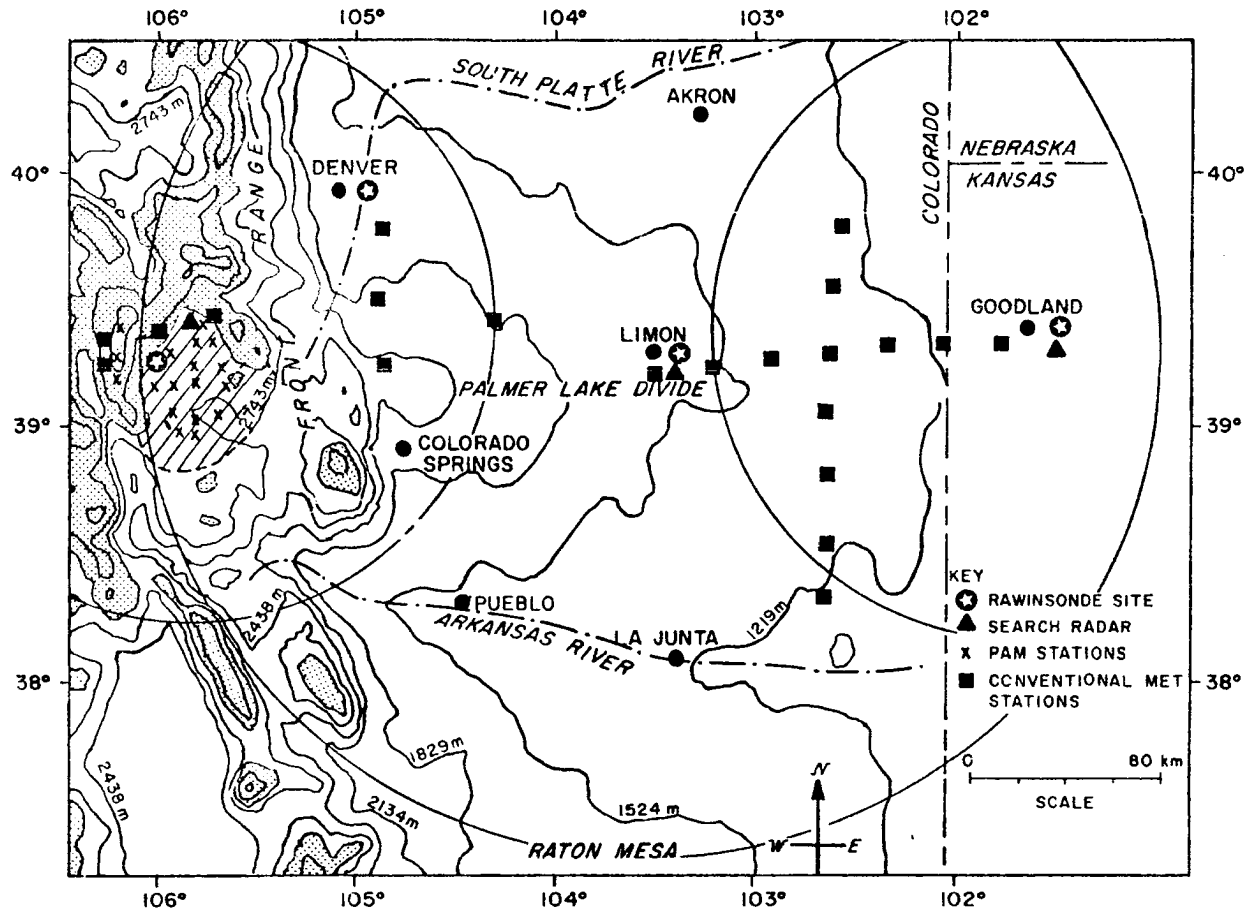


Fig. 1.1 Map of extended SPACE/HIPLEX experimental area, with average terrain contours every 304.8 m (1000 feet). The large circles represent radar effective coverage areas.

towering cumuli to propagating or translating individual thunderstorms and thunderstorm complexes, sometimes of severe intensity, to nearly stationary heavily precipitating thunderstorms.

Previous field programs conducted in the South Park area in 1973, 1974 and 1975 placed emphasis on physical processes occurring within high elevation continental cumulus clouds. These studies have included observations of radar echo characteristics and echo evolution of mountain cumuli (Huggins, 1975), visible cloud growth rates and raindrop size spectra beneath precipitating cumulus (Danielson, 1975), and the measurements of cloud microphysical structure (LeCompte, 1978; Breed, 1979). For 1977, the scope of the SPACE was extended. Much of the success of these programs was due to their ideal location. As an example, cumulus and cumulonimbus clouds formed with great regularity within a relatively small area. The time of first cumulus and first radar echo formation could be closely estimated using rawinsonde and surface data.

The case study day chosen for the SPACE target area analysis was 20 July 1977. The storm was selected as an ideal case for detailed analysis, because it was slow moving and remained over the relatively flat Park for much of its life cycle, where it was under the observation of multiple Doppler radar and automated surface mesonet stations. On this day, surface heating over the South Park area produced southeasterly upslope flow. Convective clouds first developed along the eastern slopes of the Mosquito range. As these clouds intensified and convergence increased, the intense downdraft spread out laterally beneath the convective cloud and a strong gust front marked its leading edge. The gust front provided low level convergence which sustained the

storm, and also propagated the system from the mountain slopes eastward over the flat regions of the South Park. Meanwhile, the environmental wind shear and speed were weak on this day, and the convective storm intensified as a result of the strong downdraft which was nearly coincident with the region where the cloud had grown.

The primary objective of this investigation is to examine the evolution of downdrafts within the storm which caused enhanced inflow, leading to more extensive clouds that last longer and merge with a neighboring cloud. The coupling of downdrafts and vorticity intensification in this storm will be considered also. Doppler radar and surface mesonet data are used to determine the kinematic structure of the intense slow moving storm.

This thesis is organized as follows: Section 2 provides a survey of the literature dealing with previous research on characteristics of downdrafts in convective storms. Section 3 describes the nature of the data, Doppler radar principles, analysis procedures, and sources of errors. Section 4 presents a general description of events on 20 July, and the low-level downdraft and gust front structure are considered in this section also. Section 5 discusses the evolution of the storm kinematic properties, including mean flow patterns. In addition, the physical interpretations and deductions from the Doppler radar observations concerning the downdrafts and vorticity in the storm are described in Section 5. Finally, Section 6 gives a summary of the thesis, along with conclusions.

## 2. BACKGROUND

Observations of cumulus clouds of all sizes have revealed convective-scale downdrafts to be important features of cloud circulations. The first extensive quantitative measurements of such downdrafts within cumulonimbus clouds were made during the Thunderstorm Project (Byers and Braham, 1949). Based on data gathered from nearly 1400 aircraft flights into cumulonimbi over Ohio and Florida, the downdraft was identified as a prominent feature in the thunderstorm life cycle. It was found that, in general, the most intense draft velocities occurred during the mature stage of thunderstorm development and that, except near cloud top, downdraft velocities and widths averaged only 15-20% less than those of the adjacent updraft (Braham, 1952). Braham computed average thunderstorm-cell vertical mass fluxes from aircraft measurements made during the project, finding that the downdraft mass flux increases from 400 to 900 mb, reaching at cloud base a magnitude equal to one-half the peak updraft mass flux that occurs at the 500 mb level. Further, with regard to the important role in the cloud water budget, he determined that over 45% of the total condensed water in the average storm was later reevaporated in precipitation downdrafts.

Riehl and Malkus (1958) proposed that cumulonimbus downdrafts play an important role in the total energy transport in tropical region. In an analysis of the heat budget in the equatorial trough region, they determined that saturated cumulonimbus downdrafts accompanying updrafts must be taken into account if a proper heat balance is to be achieved.

A more detailed examination of cumulus-scale downdrafts in tropical convective systems were made by Riehl and Pearce (1968) in the western Caribbean. By analyzing the equivalent potential temperature ( $\theta_e$ ) structure of the troposphere before and after the passage of several tropical wave disturbances, the authors concluded that prolonged downdraft activity must have occurred to produce the consistently observed reduction in  $\theta_e$  in the lower troposphere on the synoptic scale following passage of disturbances.

Another confirmation of the substantial contribution to total convective transport by cumulus downdrafts in equatorial regions was provided by Betts (1973a) in a study of Venezuelan thunderstorms. Mass fluxes in cumulus downdrafts determined from the compositing of rawinsonde observations taken in the region of deep convective cells during their growing and decaying stages were found to be about one-half the size of those in cumulus updrafts through the depth of the troposphere below 400 mb.

Johnson (1976) developed a diagnostic model to determine the contribution by convective-scale precipitation downdrafts to the total cumulus fluxes of mass, heat and moisture on the synoptic scale. The model was tested on the Reed and Recher (1971) western Pacific composite easterly wave data and on a heavy-rain-producing tropical depression that occurred over northern Florida in 1969. Results from both studies indicated that cumulus downdrafts contribute significantly to the total convective mass transport in the lower troposphere. It was shown that the neglect of cumulus downdrafts and their associated rainfall evaporation leads to the diagnosis of excessively large populations of shallow cumulus clouds in highly convective situations. Meanwhile,

analysis of the subcloud-layer moisture budget showed downdraft water vapor transport to be important in the water vapor balance for this layer.

It is commonly assumed that cumulus convection, having a length scale  $\sim 1-10$  km, somehow responds directly to forcing by the large-scale flow. The possibility exists that under some circumstances one or more intermediate scales may have a crucially important effect on the response of the cumulus convection or may even independently determine the nature and character of the convective activity. This possibility has been discussed by Zipser (1970), Betts (1974) and others. Measurements by Zipser (1969) and the numerical modeling results of Brown (1974) indicate that mesoscale downdrafts may contribute importantly to the total convective mass flux on the synoptic scale.

The mesoscale downdraft of a tropical squall-line system was envisaged by Zipser (1969) to be driven by widespread cooling due to the evaporation of precipitation below the base of the mesoscale trailing anvil cloud. Using a hydrostatic, unfiltered numerical model, in which both cumulus-scale convection and cloud microphysical processes are parameterized, Brown (1974) demonstrated that this mechanism is feasible. In his model, the mesoscale descent is sufficiently strong to transport midtropospheric air to lower levels and is associated with a weak, but realistic mesohigh. Observations of shallow layers of apparent warming between 700 mb and 800 mb below the anvils of convective storms over Venezuela, however, have led Miller and Betts (1977) to question whether the mesoscale downdraft is evaporatively driven or forced by some other mechanism.

Warner et al. (1979) described the two different kinds of downdrafts. They inferred that arc patterns were triggered by dense downdraft air accompanying rainfall. Apparently they were driven by constantly renewed convection, which refreshed the original density current at the surface. Downdrafts of convective scale were shown by vertical air motions measured by the aircraft, and suggested by short-lived variations of horizontal wind near and below cloud base, by vertical changes of wind and by the appearance of the clouds. Downdrafts on the mesoscale behind the arcs were suggested by clear skies, stable stratification and a reduction of wind speed at 537 and 1067 m behind the arc. The self-perpetuating arcs of the moist layer, with downdrafts on both the cloud and mesoscale, seem similar to the self-perpetuating squall lines of the troposphere, with downdrafts on both the cloud and mesoscale (Zipser, 1977).

The convective-scale downdrafts are presumed to be negatively buoyant features composed of air initially dragged downward by the weight of precipitation particles, then cooled by evaporation. This mechanism, first suggested by Brooks (1922) and later elaborated by Byers and Braham (1949), produces convective-scale downdrafts in one, two and three dimensional models of cumulonimbus clouds (e.g., Ogura and Takahashi, 1971; Takeda, 1971; Wilhelmson, 1974; Miller and Pearce, 1974).

The presence of unsaturated downdrafts in cumulonimbi has been known for a long time. Many authors have also studied the saturated downdraft on the cumulus scale. Downdrafts at the downshear edge of trade cumulus updrafts were examined by Malkus (1955) using a quasi steady-state model with aircraft observations. If saturation were

required in the downdraft, above 80% of its air would have to be entrained from the updraft. It was suggested that the downdraft originated at the top of the cloud from air which had recently been part of the updraft. Air shed from the updraft at cloud top might, because of slight dilution by the surroundings and evaporation of roughly 10 percent of its liquid-water content, acquire sufficient negative buoyancy to begin a rapid downward acceleration, once given a small initial downward velocity of the order of magnitude observed in the turbulent fluctuations at cloud boundaries. Later evidence (e.g., Ruskin 1967) that many in-cloud downdrafts are 10-20% undersaturated would permit a higher proportion of clear air entrainment. The downdrafts described above were driven by evaporation of cloud droplets detrained from nearby updrafts, and this mechanism might be involved in the upper and central parts of cloud. For downdrafts driven by the evaporation of precipitation, Hookings (1965), Kamburova and Ludlam (1966) and Das and Subba Rao (1972) developed a steady-state, one-dimensional, microphysical-kinematic trajectory model. These papers discussed the lapse rate and relative humidity within downdrafts driven by the evaporation of falling precipitation as a function of drop size, rain intensity and downdraft speed. They showed that the stronger the downdraft speed the closer the downdraft lapse rate approaches the dry adiabat and the more unsaturated it becomes. Thus, strong downdrafts can only occur if the environmental lapse rate is close to the dry adiabat. The saturated wet adiabat can only be approached by the downdraft if the downdraft is weak, the mean drop size small and the rainfall heavy.

There have been many discussions regarding the source height and the mechanism of downdrafts. Since Newton (1950), numerous studies have suggested the need for mid-level dry air in the explanation of the thermodynamical properties of downdrafts in squall lines. Kropfli and Miller (1976) analyzed a hailstorm over northeastern Colorado in its decaying stage by Multiple Doppler radar data. They found that the updraft was fed by potentially warm air from ahead of the storm, and that the source air for the downdraft is potentially cool air at midlevels. In storms described by Browing and Ludlam (1962) and by Brandes (1977) downdrafts were also found to originate in middle-levels. Emanuel (1981) attempted to explain downburst phenomena as penetrative downdrafts of the type discussed by Squires (1958), in which condensate is supplied to the unsaturated downdraft by turbulent mixing. This downdraft would originate in the middle-level dry air that has been entrained into the storm. Thus, downdrafts are found to originate at middle storm levels. This result was also obtained for tropical cumulonimbi and squall lines by Betts (1978), Zipser (1969) and others.

On the other hand, the possibility of downdrafts initiating at the top of cumulus clouds was proposed by Squires (1958). In explaining the fast-moving tongue of a spearhead echo which spawned downbursts at the JFK Airport, New York City, Fujita (1976) and Fujita and Caracena (1977) speculated on the possibility of a long-distance descent of the cloud-top air, triggered by the collapsing phase of an overshooting top. The descending currents are assumed to entrain the environmental in-cloud air, because there is no means of bringing the undiluted cloud-top air of high potential temperature down to the ground. In their recent paper, Lemon and Doswell (1979) proposed a mechanism of the rear-flank

downdraft originating at near the jet stream level. The downdraft is assumed to be cooled by the evaporation of hydrometeors falling from the sloping echo overhang while the downward acceleration is provided by the vertical gradient of the non-hydrostatic pressure, similar to that proposed by Newton and Newton (1959). Finally, through the triple-Doppler analysis of the project NIMOD data, Heymsfield and Srivastava (1980) depicted a downflow field extending from the cloud top at 8.4 km all the way to the ground. The downflow was located on the northwest side of a thunderstorm traveling northeast. At the cloud-top level there was a converging flow mainly from the northwest descending into the top of the downflow area, ~3 km across. At this point, it is appropriate to mention that the downdraft can originate at the top of the cloud from air which has been part of the updraft, but it is doubtful that this high potential temperature downflow can extend from the cloud top all the way to the ground. Likewise, the indicated mechanism can hardly be responsible for driving cold downdrafts down to the ground or even to the cloud base. As proposed by Brown (1979), common to virtually all features associated with cumulonimbus convection is the lower entropy (or  $\theta_e$ ) of the air near the surface in the rain area relative to air outside. Sounding data indicate that this air must be transported downward at least from above cloud-base and in most cases from midlevels. It is well known that downdrafts on convective time and space scales normally accompany rainfall from cumulonimbi. The coolness and dryness of these downdrafts attest to their source above the cloud base (Betts, 1976). Therefore, they are commonly cited as the explanation for the lower  $\theta_e$  values at low levels.

The preceding review shows a general description of the downdraft. It will be necessary to make further attempts to clarify the role of the downdraft which can lead to the formation of a sustained, long-lived system. Downdrafts are formed, or at least enhanced, by mid-level inflow of potentially cool air due to the vertical mass flux divergence beneath the invigorated tower (Knupp and Cotton, 1981b). These enhanced downdrafts could then lead to increased convergence at the surface at the interface between downdraft air and ambient flow, thus making downstream development possible. This situation was considered by Browning (1964), who developed a conceptual model of a severe, right moving storm in a sheared environment with veering winds. He proposed an interlocking system of up- and downdrafts, in which the potentially warm air destined to become the updraft is situated in the lower levels, and approaches the storm from the right forward quadrant. After rising within the updraft, it leaves within the anvil cloud, ahead of the storm at high levels, finally taking on the velocity of the winds at these levels. The potentially coldest air, best suited to become a downdraft, is generally located in the middle levels (Fawbush and Miller, 1954). This air is very dry, and the most efficient way to make it negatively buoyant is to chill it evaporatively. In this way a vigorous downdraft may be induced within middle level air which flows through the region of light precipitation. The most intense portion of the downdraft reaches the ground; at the surface where the downdraft air diverges strongly in all directions, but spreads predominately beneath the updraft, toward the storm's right flank. The edge of this cold outflow constitutes a gust front which is overrun by warm surface air approaching the updraft from the right forward flank. The enhanced convergence can force inflow

air up and into the updraft which causes the cloud to sustain itself longer. Miller's (1978) simulation of the quasi-stationary Hampstead storm with a three-dimensional model showed a draft structure similar to that proposed by Browning (1964) and it emphasized the dominant role of the downdraft outflow which establishes and sustains the storm through its interaction with the low level flow. Yau and Rejean (1982) used a three-dimensional anelastic model with periodic lateral boundary conditions to simulate a cumulus ensemble in Canada. They found cases where small clouds were dried by downdrafts of neighboring large clouds and cases in which under favorable conditions downdrafts of two neighboring clouds diverge on approaching the ground and generate a convergence flow in the region between them that can generate a new cloud.

Tripoli and Cotton (1980) demonstrated possible interactions between surface mesolows and downdrafts. They found in a series of numerical experiments with a three-dimensional cloud model that an initially stronger updraft and more pronounced mesolow acted to diverge a large fraction of the outflow towards the low pressure region immediately below the more sustained and intense initial updraft. The resultant convergence below the primary updraft further reinforced the updraft circulation.

An intense, quasi-steady thunderstorm which formed over South Park in Central Colorado was analyzed by using multiple Doppler radar data (Knupp and Cotton, 1981b). This storm developed within an environment having strong low-level wind shear. Analyzed storm downdrafts exhibited cellular patterns. Downdraft circulations were located both upshear and downshear of updrafts and appeared to be driven primarily by negative

buoyancy due to evaporational cooling and precipitation loading. Flow around the upshear updraft led to inflow into the storm which was apparently instrumental in driving a downshear wake downdraft similar to that observed by Heymsfield et al. (1978) and modeled by Cotton and Tripoli (1978) and Tripoli and Cotton (1980). The adjacent location of the downdraft cells produced single cold air mass at the surface. Such a structure sustained an active gust front which opposed low-level inflow and supplied the primary downshear updraft with continuous low-level forcing. It was concluded that the steadiness of the storm depended on the formation of persistent downdrafts of sufficient magnitude to sustain an active gust front.

A tornado observed on 15 June 1973 in the Florida Area Cumulus Experiment (FACE) mesonet network was studied by Holle and Maier (1980). The 15 June tornado study has illustrated several important factors in cloud growth and tornado formation in Florida. The situation is dissimilar to the midlatitude tornado associated with a moving system in a strongly sheared environment. Instead, the tornado owes its existence to the strength of vertical cumulus drafts in the subtropical or tropical environment. The interaction of these drafts with cloud-scale or mesoscale flow is sufficient to form intense new clouds which can spawn tornadoes during weak flow conditions in Florida. The 15 June funnel occurred in a region with extremely light synoptic scale winds and the weakest 850-200 mb shear measured over many FACE summers. Outflow emanated from the two largest clouds of the day, translated into the network, and met along an intersection line halfway between the two original major thunderstorms. A new cloud line formed along this gust front intersection line and grew rapidly in response to the strong,

sustained, and organized surface convergence. In one of the few studies directly relevant to the FACE tornado, it was suggested by radar observation (Gerrish, 1969) that interacting fine lines caused a tornado in South Florida, and that the fine lines represented edges of cold downdrafts from nearby thunderstorms.

Simpson et al. (1980) postulated that the joining together or merging is a major way in which convective clouds become larger, enhancing their transports and impacts upon their environment. This merger study showed first-order mergers produced an order of magnitude more rain than unmerged echoes, while second-order mergers produced another order of magnitude more, primarily owing to greater size and secondarily to longer duration. The primary mechanism of shower merger was proposed to be the downdraft or gust front interaction. This postulate has been developed in more detail by Simpson (1979) in relation to dynamic seeding effects; it is also believed to be the merger mechanism of natural showers. The approach or collision of gust front/downdrafts from adjacent clouds can force upward warm moist air which in tropical air masses is both conditionally and convectively unstable. A crucial clue to the role of downdrafts in the merging process is illustrated in Fig. 2.1. This figure shows the precursor bridge between cloud towers which virtually always precedes radar echo merger. New towers surge up from the bridge filling the gap, as the downdrafts approach and collide. Fig. 2.1 also depicts a situation with weak wind and weak shear. Ulanski and Garstand (1978), working in the same observational mesonet network, found that stronger gust fronts were associated with moving, in contrast to stationary, showers. With wind

shear, the merger process should be different and possibly more effective in joining and organizing cloud systems.

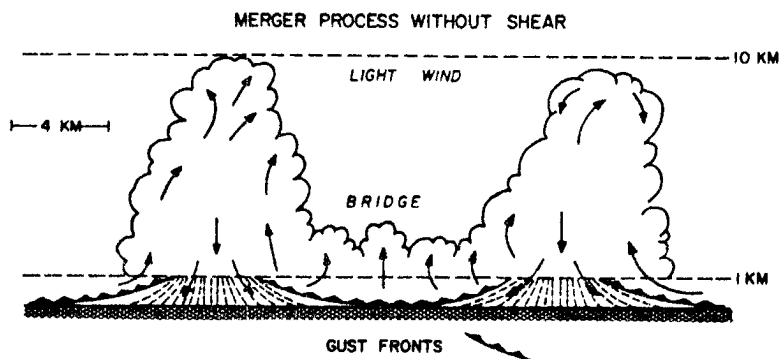


Figure 2.1. Schematic illustration relating downdraft interaction to bridging and merger in case of light wind and weak shear. From Simpson *et al.* (1980).

The ability of a gust front to enhance and/or propagate its mother cloud depends on the relative locations, motion vectors and vertical shear profiles (Moncrieff and Miller, 1976; Browning, 1977; Simpson and Van Helvoirt, 1980). The interactions between the cloud and subcloud layer in the GARP (Global Atmospheric Research Program) Atlantic Tropical Experiment were examined by Simpson and Van Helvoirt (1980). Cumulus downdrafts were postulated to be the main interaction mechanism on the scales of interest. In their case, the updraft experiences inflow only from its downshear side. Inflow into the downdraft, located on the upshear side of the cloud, as also found by Schlesinger (1978), is from the clear air upshear (north) of the cloud. At higher levels, where the updraft decreases with height, the outflow is pronounced, resembling a source embedded in a flow field. At these levels, the stronger downdraft is on the downshear side of the cloud, with the updraft air detraining into it; updraft air is also detraining into the upshear downdraft which dominates the lower portion of the cloud. Further insight into cloud propagation mechanisms was obtained by

examining the cold downdrafts directly beneath the active cloud towers, which rapidly spread downwind with a sharp gust front at the leading edge. Convergent conditions at the upwind edge of the cumulonimbus cloud, together with an unstable moist subcloud layer favored the growth of new towers at the edge of the cloud, leading to some propagation upwind. These clouds grew, eventually merging with the old ones, enlarging the complex. Weaker convergence was also found at the forward edge of the gust front, where new cumulus growth might also be sought.

Moncrieff and Miller (1976) used theory and numerical simulations to discuss the maintenance of tropical cumulonimbi that tend to propagate faster than the wind at any level in which they are embedded. They argue that under certain conditions a density current due to a diverging downdraft near the ground propagates at the same speed as the cloud and the net result is a convergent region beneath the updraft, forcing continuous uplifting of the moist low-level inflow along the right flank. In this manner the storm maintains its moisture supply and tends to propagate to the right.

Using a three-dimensional numerical cloud model, self-sustaining right-and left moving storms were simulated by Klemp and Wilhelmson (1978). The right-moving storm developed a structure which displayed strong resemblance to Browning's (1964) three-dimensional conceptual model for a single-cell right moving storm. For the right-moving storm moisture is supplied through low-level inflow from the east and is carried upward through a cyclonically rotating updraft. Meanwhile, the right-moving storm induces a flow at middle levels which passes around the east side of the updraft from the south and feeds into the downdraft located on the north side of the updraft. In addition, the downdraft is

supplied by flow from the west which develops anticyclonic rotation. The main downdraft is confined almost entirely beneath the level of maximum updraft velocity. The downdraft associated with this right-moving storm then spreads out just above the ground to the south underneath the updraft. The resulting gust front forming along the right flank of the storm produces strong low level convergence which forces uplifting of moist inflow from the east to sustain the updraft. This gust front induced convergence appears to govern the storm's propagation.

Ray et al. (1981) investigated the severe storms which occurred in western and central Oklahoma on 20 May 1977. The severe storms on this day were characterized by deep up- and downdrafts. After the storm reaches a mature stage, the downdrafts at 2 km height are closely associated with strong reflectivities. In time, the updraft becomes elongated in an east-west direction and as the cyclonic rotation develops in the vicinity of the updraft, rain and downdrafts begin to move around the western portion of the updraft. As the circulation intensifies and the gust front south of the updraft moves eastward from the center of circulation, a downdraft forms behind it and a new updraft develops at the leading edge of the outward propagating gust front. This new updraft is in the weak echo region and is associated with the hook in the rain water field.

There have been several hypotheses concerning the origin and intensification of rotation and downdrafts in severe thunderstorms. Based on Doppler radar observations of the Harrah tornadic storm, Heymsfield (1978) suggested that a vorticity couplet which centered on the updraft originated at mid-levels by the tilting of vorticity. In

In this case, as the updraft became more vigorous, the tilt of the updraft was increased due to increased low-level inflow (momentum). Precipitation particles having large terminal fallspeeds descended from the rear of the tilted updraft. A downdraft developed due to evaporation and melting of precipitation, and several processes were capable of producing an anticyclonic downdraft in the middle troposphere along the left flank. The increased anticyclonic vorticity along the left flank resulted in an air flow reversal, which shifted the mid-level vorticity couplet northward such that the cyclonic vorticity was centered on the updraft, and the anticyclonic vorticity was to the left of the updraft. At low levels, the low level mesocyclone intensified as air descended along the left flank of the storm and intensified the low-level mesocyclone at inflow-outflow boundary. A second downdraft along the right storm flank, was suggested to be less important in mesocyclone intensification. Lemon and Doswell (1979) have provided a revised severe storm conceptual model which proposes two downdrafts, one downdraft is located in the precipitation cascade region downwind (relative to the 3-5 km AGL flow) of the updraft. The other downdraft lies immediately upwind of the updraft (relative to the 7-10 km AGL flow). The latter downdraft was suggested of importance in mesocyclone intensification and storm evolution, and forms when air decelerates at the upwind stagnation point of the intense blocking updraft and is forced downward, mixing with air from below which reaches the surface through evaporative cooling of cloud and precipitation droplets and, perhaps, through precipitation drag as well. Barnes (1978) has also suggested the importance of a similar downdraft in tornadogenesis, produced by updraft blocking. Schlesinger's (1980) three-dimensional

cloud model results give two downdrafts: the main one on the upshear cloud edge and strongest at low-levels, and the second one on the downshear cloud edge between 3 and 6 km. Schlesinger's upshear downdraft was produced by pressure gradient forces and is similar to the downdraft Lemon and Doswell have asserted to intensify the mesocyclone and subsequently produce tornadoes. The models (Schlesinger, 1978, Klemp and Wilhelmson, 1978) also revealed that counterrotating horizontal vortices formed first in the middle troposphere and storms split under certain shear conditions. They concluded the tilting term to be important in initiating a vortex couplet in midlevels.

Finally, based on multiple-Doppler radar observations of a non-severe Illinois thunderstorm occurring on 29 May 1978, Heymsfield (1981) found an interesting coupling of the updraft, downdrafts and vorticity in this storm. Four downdrafts were identified in the storm: a downdraft upshear of the updraft, downdrafts on the left and right flanks, and a downshear downdrafts. The blocking of the environmental flow by the updraft was important in development of the downdrafts. The main downdraft was the upshear downdraft during the growth period of the cell, probably due to a combination of non-hydrostatic vertical pressure gradient forces and evaporative cooling by precipitation falling out of the upshear updraft edge. The location of upshear downdraft at mid-to upper levels resembles Lemon and Doswell's conceptual model (1979) and three-dimensional cloud model results of severe storms. Downdrafts on the left and right developed as upper level air was diverted around the sides of the updraft, as the precipitation core descended to the surface and a minor pulsation in the updraft occurred. The major downdrafts during the mature period were the left and right flank downdrafts, but

the right flank downdraft was weaker and its intense period was short-lived. The downshear downdraft resulted from the convergence region downwind of the cell resulting from environmental air flowing around the cell at upper levels. This downdrafts, though quite weak, is in a similar location to Lemon and Doswell's front flank downdraft. The vorticity in the cell developed first in mid-levels as a couplet centered on the updraft, and the tilting term appears to be important in initiating this vorticity. The mid-level vorticity intensification was found to result from the tilting term, in the region between a right flank downdraft and the main updraft. This is different from the Lemon and Doswell's (1979) model. They suggest that the updraft is initially cyclonically rotating, and that the rotation shifts between the updraft and rear flank downdraft. After the vorticity couplet intensified to its maximum value, it advected downshear of the updraft. This is not similar to the mesocyclones in severe storms which usually remain tied to the storm core, often in a favorable location relative the updrafts and downdrafts. In the Illinois case, low-level downdraft outflow moved upshear away from the updraft, and did not sustain the low-level lifting mechanism.

The South Park case study is an attempt to examine the evolution of downdrafts which cause enhanced inflow, leading to more extensive clouds that last longer and merge with a neighboring cloud. The coupling of downdrafts and vorticity intensification in this storm will be considered also.

### 3. INSTRUMENTATION, ANALYSIS TECHNIQUES, AND ERRORS

#### 3.1 INSTRUMENTATION

Data used in this thesis were obtained from the following sources: (1) rawinsonde unit; (2) NCAR's Portable Automated Mesonet (PAM); and (3) three Doppler radars. The location of each instrument within South Park is shown in Fig. 3.1.

The main base station was located about 10 km south of Fairplay, Colorado on dry, flat pasture land, about 5 km east of the wooded foothills of the Mosquito Range. Rawinsondes were launched from the base station on 20 July 1977 at 0600 Mountain Daylight Time (MDT), 1003 MDT and 1355 MDT. Temperature measurements were made by a thermister, humidity by a hygrometer, and wind speed by a tracking unit. Data quality were generally quite good, and there was no tracking problems. Wind data given in the present thesis have been smoothed in vertical to reduce possible wind errors. A calibrated aneroid barometer within the instrument package yields a temporal record of the balloon's height. The base station was the site of SPACE micrometeorological experiment; it was also the site of the National Oceanic and Atmospheric Administration (NOAA) Lidar system, which included a 1 cm radar and a large array of radiation sensors as well as the Lidar equipment.

The National Center for Atmospheric Research (NCAR) Portable Automated Mesonet (PAM) was deployed on the South Park scale. As shown in Fig. 3.1, twenty remote weather stations were spaced roughly on a 10 X 10 km grid, with two remote stations located on the ridge top of the

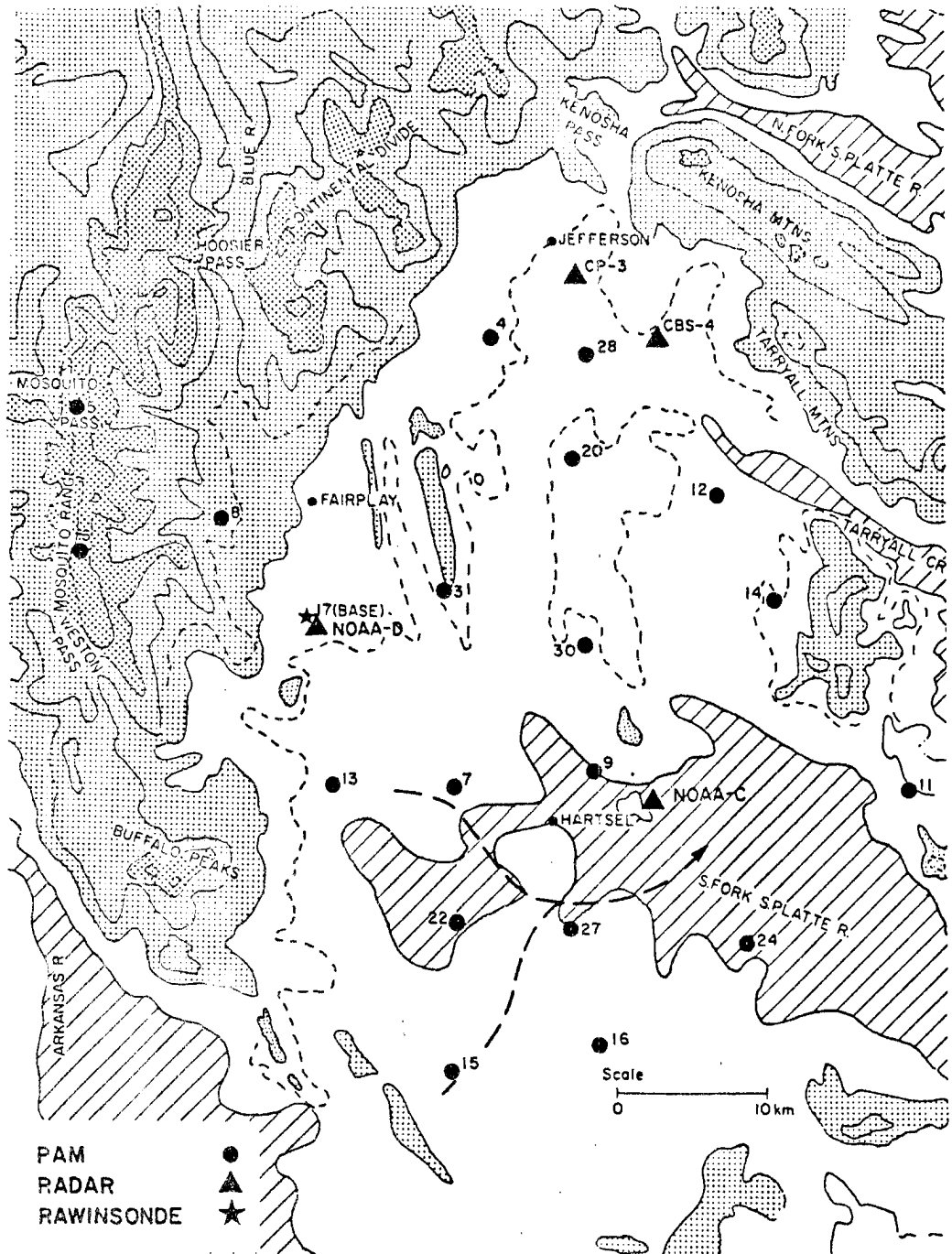


Fig. 3.1. Map of terrain in South Park, Colorado. Regions below 9000 ft. (2744 m) are hatched; regions above 10,000 ft. (3049m) are lightly shaded; and regions above 12,000 ft. (3657m) are heavily shaded; contours intervals are 1000 ft. (305 m). Dash line depicts trajectory of the storm.

Mosquito Range. Each remote station measured various meteorological variables including wind speed and direction 4 m above the ground, wet- and dry-bulb temperatures and pressure from 2 m above the ground, and rainfall in 0.254 mm increments with a tipping bucket raingauge. Data were telemetered from the remote stations once per minute to the PAM base van which was located at the base station. These data were instantly available for display on a computer graphics terminal located in the van. In most cases, PAM stations were located in relatively open areas away from significant obstacles such as trees and rough terrain.

Because the PAM system provides the capability of real-time display of surface data as well a recording of those data on a single computer-compatible tape recorder, it has a number of advantages for operational decision making and data analysis. In SPACE the PAM data were used to determine where active convection was about to begin or where vigorous convection was expected to continue. This type of information was critical in SPACE, which needed a significant lead time to get aircraft on site. A second utilization of PAM was that one could look not only at the surface moisture available for convection at a central site but also at the gradients of moisture over the experimental area. Another application for which the PAM system is also useful is defining the location and alignment of surface fronts which may exist within the network. The main advantage of PAM for the post analysis of mesonet data is that these data are recorded on a single, computer-compatible tape. Thus, the mesonet data can be easily computer processed and displayed.

As with any new system, there are problems with PAM. The instrumentation on the remote sites was in general quite reliable. The

sensor that gave the most failures was the pressure sensor. One consequence of the loss of the pressure sensor was that calculated variables which depended on pressure could no longer be obtained. A solution to this problem that would allow reasonable estimates of these variables in the field would be to assign each station a pressure which corresponded to its mean value. On 20 July 1977, pressure sensor at station #13 had a consistent problem. Thus, the mean value of pressure was used for field calculations. Another data anomaly was that the raingauges which were tested by tipping the buckets at the remote sites, introduced spurious precipitation amounts into the data. Since the base station was powered by commercial power, it went down whenever there were major power surges. Unfortunately this usually occurred at a time of peak interest when a thunderstorm gust front was passing through the network. Also cold temperatures in the base station seemed to affect the base performance. On 20 July, system reliability was generally quite good, except for the few times the system crashed due to thunderstorms. A severe lightning storm passed over the base at 1230 crashing the system and disabling the base station with a direct lightning stroke. A thorough discussion of the PAM system is given by Brock and Govind (1977), and its application to South Park by George and Cotton (1978).

Triple Doppler radar data were also taken on the South Park scale. NOAA provided two 3.2 cm wavelength (X-band) Doppler radars, and NCAR provided the 5.5 cm (C-band) CP-3 radar. NOAA-D was located at the base, NOAA-C was 27 km southeast of the base, and CP-3 was 30 km northeast. The CP-3 radar also provided full volume ( $360^{\circ}$ ) scans in addition to coordinate sector scans. CP-3 was chosen for this task

because it provides more reliable reflectivity data than the NOAA radars, and because its scan rate is faster than the NOAA radars, allowing it more free time during the triple-Doppler experiments to perform full volume scans. The specifications of each radar are given in Appendix A. Radar data was also available from the NWS 10 cm WSR-57 radar located in Limon, Colorado. Data from this unit was archived in the form of photographs of the PPI display, and manually drawn overlays of the PPI display was also made throughout the experiment. The NWS radar was used to determine the eastward extent of the mesoscale system described herein. It is well known that the Limon radar signal is deteriorated by the effects of ground clutter and beam blockage over the mountainous terrain, but can be used effectively for mapping positions of echoes over the mountainous regions. The NCAR CP-3 radar was used as the main source of quantitative PPI data. It should be noted, however, that sidelobing problems with the CP-3 radar could have contributed to overestimates of reflectivity in storms located near the mountain peaks, particularly in a 10-25 km annulus east, north and west of CP-3. GEOS geosynchronous satellite data applicable to the larger scale were available in visible and infrared imagery.

### 3.2 Background on Radar and Doppler Radar

Radar is a remote sensing instrument, and it relies upon scattering and propagation of electromagnetic (EM) waves through an inhomogeneous atmospheric medium. Thus, it is necessary to describe some of the characteristics of scattering and propagation of EM waves.

For most purposes, the speed of propagation of an EM wave may be considered to be constant and equal to the speed of light in free space. But, the atmosphere is significantly different from free space and that

the observed air-mass properties are sufficiently variable to produce small changes in the speed of propagation. These small changes are important because they may lead to refraction of the radar ray and produce marked changes in the direction of propagation. In the study of optics, it is common to define the index of refraction as the ratio of the speed of light in a vacuum to that in some medium. Spatial variations in the index of refraction, which are commonly observed in the atmosphere, can introduce significant bending of radio waves in the same manner as light rays passing from water to air. If sufficient bending occurs, the wave emitted from a ground station is said to be trapped, and the region in which the energy is trapped is called a duct. Within the duct the strength of the electromagnetic field is greater than it would be under standard conditions, and the duct acts as a guide and may direct the energy to long distances within a narrow layer near the earth's surface. The important source of ground ducts is the diverging, cool downdraft under a thunderstorm. When the relatively cool air spreads out from the base of a storm, the result is a temperature inversion in the lower layer. Because of the evaporation of raindrops, the air has a high specific humidity, and a strong duct can be formed over a relatively small area in the vicinity of the thunderstorm. From a careful surveillance of a radar screen, one can detect the establishment of anomalous propagation conditions by the sudden increase in the number and range of ground targets.

At this point, it is appropriate to note qualitatively the process by which a drop scatters an intercepted radio wave. When a plan-polarized wave passes over a spherical drop, it induces oscillating electric and magnetic dipoles within the drop. Energy is taken from the

incident field. Part of this energy is absorbed as heat by the drop, and part is reradiated as a scattered electromagnetic field having the same wavelength as the incident energy. The physics of scattering processes are dependent on the size and shape of the scattering particle, the incident wavelength, and the refractive index of the medium. For spherical particles small compared to the incident wavelength, the scattering follows Rayleigh's theory. In the case of larger particles or short wavelength radars, the scattering of energy follows the more complex Mie theory. When Rayleigh scattering holds, the average received power is proportional to the sixth power of the particle radius. In Mie theory, however, such an ideal size relation does not exist, and significantly more energy is scattered in the forward direction. Scattering processes within precipitation are generally complicated because precipitation particles may be composed of water, ice, or a mixture of both. Such variations then produce corresponding variations in the complex index of refraction. In addition, departures of precipitation shapes from sphericity introduce further complications. Thus, the derived reflectivity values should be interpreted cautiously.

Another factor which should be accounted in analysis of reflectivity data is attenuation, i.e., the reduction in intensity of the electromagnetic wave along the beam path between the radar and the target. The attenuation experienced by radar waves is a result of two effects: (1) absorption, and (2) scattering of power out of the beam. In general, gases act only as absorbers. The only atmospheric gases which need be considered as absorbers are water vapor and oxygen. Each gas absorbs energy because the individual molecules behave like dipoles.

Water vapor has a permanent electric dipole moment; oxygen has a permanent magnetic dipole moment. At wavelength greater than 3 cm, gaseous attenuation is small and can be neglected unless long ranges are involved. The attenuation of electromagnetic waves by hydrometeors in the atmosphere may result from both absorption and scattering, depending on the size, shape, and composition of the particles. Attenuation decreases with increasing wavelength; at wavelengths in the 5 and 10 cm bands, cloud attenuation can be safely neglected. Also, attenuation increases with decreasing temperature. These relations are a reflection of the dependence of the refractive index on both temperature and wavelength. The effects of the different dielectric properties of water and ice are illustrated by the differences in attenuation. Ice clouds give attenuations about two orders of magnitude smaller than water clouds of the same water content. Attenuation by hail is usually more significant, but not always consistent. Uncertainties about the effects of deviations from sphericity on the part of hailstones and about their compositions introduce substantial problems about the calculation of the attenuation. Radar transmission losses through the radomes of the NCAR portable C-band Doppler radar (CP-3) were examined by Wilson (1978b). Two losses have been considered: (1) that resulting from attenuation through the water film that builds up on the outside of radome during rain, and (2) that through the radome itself which houses the antenna dish and changes in structural characteristics from base to top. It was concluded that radome attenuation amounts to at most 1-2 db. For the storm examined in this thesis, values of the attenuation range from 2 db to 5 db.

Many weather-radar sets make use of an antenna consisting essentially of a point source at the focal point of a parabolic reflector. The power is reflected from the surface and directed along lines parallel to axis of the parabola, which is known as the major lobe. Smaller, secondary lobes are usually found their central axes directed at various angles with parabola's axis (Fig. 3.2). The actual shape of the lobes depends on the shape and size of the antenna, the wavelength involved, and the type of feed used as a source (radome).

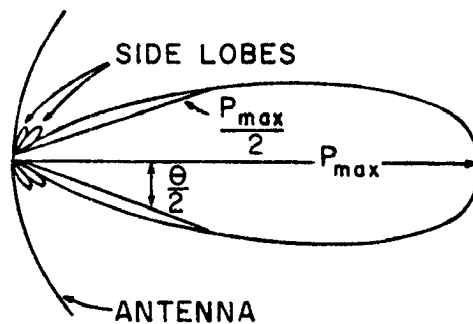


Fig. 3.2. Schematic cross section of radar beam from a parabolic antenna reflector.

The beam width  $\theta$  is usually defined as twice the angle between the direction of maximum power and the direction at which the power is half the maximum value. In some radar applications only the power in the major lobe is considered because the minor lobes represent relatively small amounts of power. The summation of the power within the solid angle defined by the half-power points is about 80 percent of the total power. However, when targets have high reflectivities or are located at small ranges, even the low-level power from the side lobes may lead to sufficient backscattered power to give an echo. In such cases, the side lobes may produce serious echo distortions.

The precise antenna power patterns of the Doppler radars used in South Park experiment 1977 were not determined in the field. However, the NOAA-X-band radars exhibit well behaved patterns, with relatively insignificant amount of power within secondary lobes. On the other hand, CP-3 had significant and nonuniform side lobes which were reinforced by interference effects with metal bolts and nonuniformity of the fiberglass construction of the radome housing the antenna. Both side lobes and the main lobe introduce errors in radial velocity and variance estimates, and distortions in reflectivity patterns. The magnitude of radial velocity errors is dependent upon the angular distribution of power within the secondary lobes. Such errors can be minimized by placing radars in shallow depressions such that side lobe energy is cut off by the nearby horizon.

The velocity of scatters in the free atmosphere can be obtained by means of coherent radars. The name Doppler radar has been given to the class of radar sets which measures the shift in microwave frequency caused by moving targets. The Doppler shift frequency is described in greater detail by Battan (1973) and Atlas (1964). Meanwhile, in this thesis, Doppler spectra were obtained from the Doppler radar time series data using pulse-pair covariance technique (Sirmans and Bumgarner, 1975).

The use of a single Doppler radar to determine kinematics properties of the wind field accompanying widespread precipitation has been treated in depth by Browning and Wexler (1968). In this case, features of the wind near the radar site are derived from the record of radial velocity along annuli completely surrounding the station when the air is filled with radar targets which are good tracers of the

horizontal component of the wind. Measurements from two or more locations are required, however, to estimate the wind field in a region remote from the radar.

As illustrated in a growing number of references (see Gray et al., 1975; Burgess et al., 1976; Baynton et al., 1977), it is possible to infer storm structure from only the radial component of wind from one radar, although not always unambiguously. However, certain patterns or signatures may be used in interpreting displays of single-Doppler radar data. One approach is that described by Burgess et al. (1976), where the velocity pattern is displayed in rectangular (range, azimuth) format with velocity at each location represented by a vector whose length is proportional to received power and whose orientation ( $\psi$ ) with respect to an arbitrary origin is given by

$$\psi = \frac{\bar{V}\pi}{V_{\max}}, \quad (3.1)$$

where  $\bar{V}$  is the mean velocity estimate and  $V_{\max}$  ( $=\lambda \text{ PRF}/4$ ) is the Nyquist interval (or the velocity range in which all radial velocity estimates are represented); PRF is the pulse repetition frequency and  $\lambda$  the radar wavelength. Another approach utilizes the resolution afforded by color displays such as the NCAR display system (Gray et al., 1975). In this system velocities between  $\pm V_{\max}$  are assigned one of 15 colors. Velocities extending beyond Nyquist interval enter the scale of colors at the opposite end. Here the transition of colors and the ambiguity of the velocity is readily visualized as the velocities are aliased. The display technique is perfectly general with the Nyquist interval determined by the radar wavelength and PRF. Baynton et al. (1977) have described how this display may be used to interpret data obtained from

large-scale precipitation systems. Ray et al. (1980) have extended these and other results to illustrate patterns obtained from observations of severe local storms that occurred in central Oklahoma on 20 May 1977. In their case, color displays of single-Doppler radial velocity patterns aid in the real-time interpretation of the associated reflectivity fields and can reveal important features not evident in the reflectivity structure alone. Such a capability is of particular interest in the identification and study of severe storms.

### 3.3 Multiple-Doppler Radar Analysis

In recent years, simultaneous observation of atmospheric phenomena using two Doppler radars has come into increasing use. Two types of scanning techniques, COPLAN and independent, have been used in the past. In COPLAN method, wind field determination is greatly simplified if synthesis is performed in cylindrical coordinates with an axis colinear with the line connecting the two radars. Lhermitte and Miller (1970) suggested that Doppler data acquisition be confined to planes in this frame so that winds in each plane could be deduced directly with minimal data interpolation. Since COPLAN technique was not used to acquire data for this thesis, a detailed description will not be given. Details can be found in Lhermitte and Miller (1970) and Miller and Strauch (1974). In the independent scanning technique, each radar independently scans a given azimuth sector at various elevation angles. In this method, as in the triple-Doppler radar method, it is assumed that storm motions remain steady during the time interval require to scan a common region. Thus, temporal coordination among or between radars is essential. The dual-Doppler radar can provide information about two dimensional wind field; then application of continuity equation, and an estimate of particle

terminal velocity (from reflectivity) are in principle sufficient to synthesis the three-dimensional wind field (Armijo, 1969). Even when improvements such as the anelastic form of mass continuity, as introduced by Ray et al. (1975), are used vertical wind estimates are still unacceptable for many applications, such as accurate computation of trajectories, vertical fluxes of momentum, heat, moisture, etc. This is largely due to accumulation of numerical integration error and the inability of properly sample precipitation-free areas and data close to the earth's surface where divergence may be expected to be a maximum. The addition of a third radar relaxes the requirement of either the continuity or terminal velocity relations. Armijo (1969) has shown that use of three Doppler radars allows for the immediate realization of the horizontal wind components ( $u, v$ ) and the net vertical Doppler precipitation velocity ( $w + V_T$ ), where  $w$  is the vertical wind component and  $V_T$  is the precipitation fall velocity, throughout the region of interest. The advantages of three or more radars are illustrated in terms of extended areal coverage, error variance reduction and mitigation of poor sampling effects of divergence fields near the ground (Ray et al., 1978). In this thesis, although three Doppler radars were functional during the time period of interest, data from only two Doppler radars were used to determine mean storm motions in most of the analyses presented later. The theory for determination of three-dimensional wind field was developed by Armijo (1969) and later expanded by Bohne and Srivastava (1975). The following section summarize their work.

A right-handed cartesian coordinate system (X, Y, Z) with the plane  $Z = 0$  coinciding with a flat earth surface is used. For simplicity, the origin of the coordinate system is taken to coincide with the location of one of three Doppler radars. Second radar is placed on the X axis a distance  $X_2 = 2D$  from the origin, that is at  $(2D, 0, 0)$ , and third one is located at  $(X_3, Y_3, 0)$ . The coordinate system and radar placements is shown in Fig. 3.3. For an arbitrary point  $P(X, Y, Z)$  in the region of precipitation, the three radars measure outward radial velocity components  $(V_1, V_2, V_3)$ , respectively given by the following equations

$$V_1 = \frac{1}{R_1} [Xu + Yv + Z (w+V_T)], \quad (3.2)$$

$$V_2 = \frac{1}{R_2} [(X-X_2)u + Yv + Z (w+V_T)], \quad (3.3)$$

$$V_3 = \frac{1}{R_3} [(X-X_3)u + (Y-Y_3)v + Z (w+V_T)], \quad (3.4)$$

where  $u$  is the horizontal wind in the positive X direction,  $v$  the horizontal wind component in the positive Y direction,  $w$  the vertical wind component and  $V_T$  the terminal fall velocity of the precipitation.

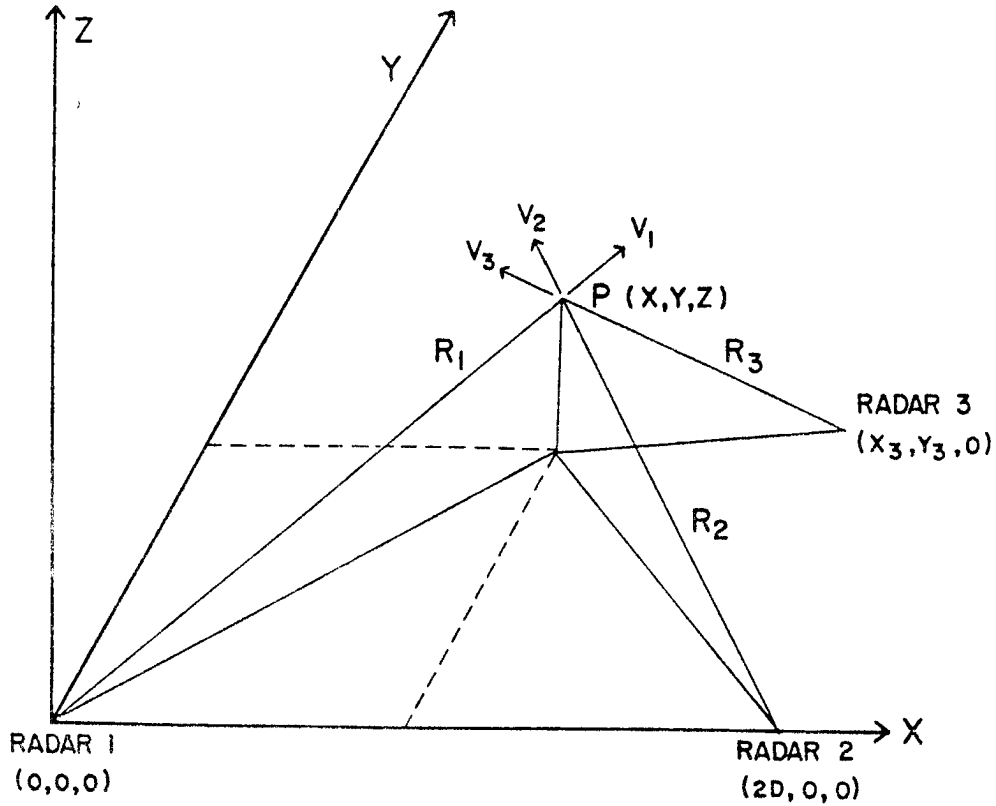


Fig. 3.3 Coordinate system geometry.

$R_1$ ,  $R_2$  and  $R_3$  are the radial distances from each radar to the point of observation and are given by

$$R_1^2 = X^2 + Y^2 + Z^2, \quad (3.5)$$

$$R_2^2 = (X-X_2)^2 + Y^2 + Z^2, \quad (3.6)$$

$$R_3^2 = (X-X_3)^2 + (Y-Y_3)^2 + Z^2. \quad (3.7)$$

this system of equations from (3.2) to (3.7) are supplemented by an equation of continuity

$$\frac{\partial u}{\partial X} + \frac{\partial v}{\partial Y} + \frac{\partial w}{\partial Z} = kw, \quad (3.8)$$

where  $k$  is a small positive constant which approximates the negative logarithmic vertical gradient of air density,  $-\partial(\ln\rho)/\partial Z$ . In this

equation, the local variation of air density and horizontal advection of air density are assumed to be negligible.

For the case of two Doppler radar the horizontal wind components can be obtained from equations (3.2) and (3.3),

$$u = \frac{1}{X_2} (R_1 V_1 - R_2 V_2), \quad (3.9)$$

$$v = \frac{1}{YX_2} [(X_2 - X) R_1 V_1 + X R_2 V_2] - \frac{Z}{Y} (w + V_T). \quad (3.10)$$

The  $v$  component is dependent on the net vertical Doppler precipitation velocity and is resolved after an independent estimate of particle fall velocity ( $V_T$ ) is made and the equation of continuity is used to determine the vertical wind component ( $w$ ). Often the elevation angles used are small enough to justify neglecting the vertical component term in the  $v$  equation. In such instances the horizontal wind field is obtained directly and the vertical component can be realized by using the continuity equation.

In the case of three Doppler radars the system of equations (3.2), (3.3) and (3.4) can be solved for the components  $u$ ,  $v$ , and  $W = w + V_T$  to yield

$$u = \frac{1}{X_2} (R_1 V_1 - R_2 V_2), \quad (3.11)$$

$$v = \frac{1}{X_2 Y_3} [(X_2 - X_3) R_1 V_1 + X_3 R_2 V_2 - X_2 R_3 V_3], \quad (3.12)$$

$$W = (w + V_T) = \frac{1}{X_2 Y_3 Z} \left\{ [(X_3 - X_2) Y - (X - X_2) Y_3] R_1 V_1 \right. \\ \left. + (X Y_3 - X_3 Y) R_2 V_2 + X_2 Y R_3 V_3 \right\}. \quad (3.13)$$

As mentioned earlier, the use of triple Doppler radars allows for the immediate realization of the horizontal wind components ( $u, v$ ) throughout the precipitation volume from combination of the radar velocity estimates alone. The vertical component may be obtained from Eq.(3.13) by independent estimation of  $V_T$  or through use of the equation of continuity.

Bohne and Srivastava (1975) have discussed that  $V_T$  can be reliably estimated from the radar reflectivity factor then  $w = W - V_T$  yields  $w$  directly. This method may be sufficiently accurate to enable detection of convective elements embedded in generally stratiform snow except in the very lowest levels. In the case of deep convective storms, a preferred procedure is to estimate  $V_T$  near the top from radar reflectivity factor, then compute  $w = W - V_T$  at this level and then derive  $w$  by integrating the continuity equation from the top. Then  $V_T$  may be simply obtained by subtracting  $w$  from  $W$ .

#### 3.4 Nonrandom, Systematic Errors

There are many sources of error for winds derived from a network of Doppler radars, and the importance of each has not been fully explored. In fact, the effect of random errors, the easiest to evaluate, is the only one explored to date, e.g., Bohne and Srivastava (1976), Lhermitte and Gilet (1976), Ray *et al.* (1978), and Clark *et al.* (1980). For random errors which are independent of height, Bohne and Srivastava (1975) showed theoretically the horizontal wind components are reasonably accurate to  $<1 \text{ ms}^{-1}$ , and vertical velocity derived by downward integration is accurate to less than a few meters per second. In addition to random errors which are produced by uncertainties in Doppler radar velocity estimates, nonrandom, or systematic errors are

commonly present. Nonrandom errors can be due to radar characteristics and scanning procedures, instrument errors and limitations, and errors and biases created in the analysis. Some of the characteristics of each category are discussed below.

Errors from radar characteristics and scanning procedures originate from the following sources: (1) storm transience; (2) storm advection during the time interval taken to scan the target volume; (3) volume sampling differences among radars; (4) use of radars with different wavelengths. Small-scale flow features within thunderstorms are essentially transient, thus, errors are introduced when common storm points are not scanned simultaneously, as in the case of independent radar scanning. Clark et al. (1979) have investigated the effects of temporal errors, which were primarily due to cell evolution, by using the results of three-dimensional cloud model. For the cases of using three Doppler radars it was found that the temporal errors were of the same magnitude as the more usual random sampling error estimates ( $0.5 - 1.0 \text{ ms}^{-1}$ ). Analysis cases with a reduced scan period or equivalently with an increased radar separation resulted in a reduction of the temporal errors. On 20 July, total radar scan times were relatively long (~5 min), thus, these data are subject to temporal errors. Another type of errors which are due to differences in radar sampling volume (pulse volumes) arise from the use of radars whose pulse volumes exhibit large differences. Their magnitude is probably a function of wind and reflectivity gradients present within the large storm. The characteristics of errors introduced when radars with different wavelengths are combined have not been investigated thoroughly. Such errors result from differences in reflectivity estimates (scattering

properties and attenuation) which introduce nonuniform weighting in the computation of mean radial velocity. Finally, errors due to the storm advection during the finite scan time can be minimized by implementing spatial corrections based on storm speed of movement.

CP-3 radar had several software problems, including range gate errors and production of bad velocity flags in region of high turbulence and wind shear. These errors can be detected and removed by objective data processing schemes. The presence of side lobes, ground clutter and appreciable variations in wind and reflectivity fields can lead to significant radial velocity errors. Since radial velocities are combined from two or more radars, errors in measurement of radar azimuth and elevation angles, or in relative radar positions, will lead to errors in synthesized wind components. These errors are proportional to the magnitude of wind shear and to the radar-storm distance. These errors are probably negligible because each radar made a daily calibration of azimuth and elevation angles.

Errors and biases created in analysis result from certain assumptions made and procedures used in the data analysis. Transformation from radar coordinates to cartesian coordinates requires interpolative schemes which smooth the data fields both horizontally and vertically. Such a process significantly reduces error magnitudes present in the raw-data. The horizontal wind components are determined generally more accurately than the vertical wind component. This is because the errors in the horizontal wind components used to compute the vertical wind component accumulate during integration. Other error sources particularly important in the vertical wind computation include the effects of combining inappropriate divergences resulting from an

uncertain estimate of storm motion and a finite data collection time. The effects of storm evolution over the data collection interval are greater for the vertical wind component. Additional vertical velocity errors may result from assignment of the boundary condition used in vertical integration of the continuity equation. For upward integration from the surface, a boundary condition of  $w = 0$  at  $Z = 0$  is accurate, but a combination of factors, including ground clutter contamination and inaccurate observation of low-level divergence, often prohibit accurate  $w$  estimates, especially in rough terrain. A second option assumes a boundary condition of  $w = 0$  at storm top, with the additional assumptions that the storm top remains at a steady state and that the hydrometeor terminal velocities at storm top are small. A discussion showing the increased accuracy of wind estimates obtained from downward integration over those obtained by upward integration appears in the Appendix B.

### 3.5 Method of Analysis

During the period of interest, independent, coordinated azimuthal scans of a common volume were made by each radar. Temporal and spatial resolution was only fair. Data tapes from all radars were reformatted to a common format and then edited to eliminate bad data. Data editing consisted of de-aliasing mean radial velocities (Ray and Ziegler, 1977), thresholding data fields to eliminate data with low signal-to-noise ratios (S/N), deleting points which contained bad data values, and implementing a two-dimensional pattern recognition on radial velocity data having low S/N. De-aliasing was largely subjective, however, the location of aliased radial velocity values was usually unambiguous. Radial velocities with magnitudes larger than the Nyquist velocity were

unfolded along radials by checking for large gradients of radial velocity between the range bin value and values from neighboring unfolded range bins. Radial velocity estimates were also thresholded at 7 dB S/N. Data editing stages were followed by interpolation to cartesian grid and subsequent synthesis to produce cartesian velocity fields.

Radial velocity and reflectivity data were interpolated from radar (spherical) coordinates to common cartesian grid points spaced 1.0 km in the horizontal and 0.5 in the vertical, using a spherical volume with a 1.2 km radius of influence, centered at a grid point. Points within the volume were linealy weighted according to the distance from the center grid point. Approximately 15 raw points contributed to an individual grid point radial velocity estimate. CP-3 reflectivity and radial velocity data were interpolated similary except with a 1.0 km radius of influence.

Estimates of radial velocity from the Doppler radars were combined at common grid-points to obtain the horizontal wind components. Divergence and velocity calculations at grid-points were made using a centered finite difference approximation. The vertical velocity can be calculated by several methods (Bohne and Srivastava, 1975): upward (from the surface) or downward (from the cloud top) integrations of the anelastic continuity equation using only the calculated  $u$  and  $v$  components or from  $W = w + V_T$ , where  $V_T$  is the mean particle fallspeed estimated from an empirical relation relating the fallspeed of the precipitation particles to the radar reflectivity factor. Downward integration of the anelastic continuity equation was chosen because upward integration and the  $W$  method gave physically unrealistic results.

Bohne and Srivastava (1975) have also shown theoretically the downward integration tends to suppress errors and results in the highest accuracy. The upward integration was unreliable in part due to errors in divergence estimation near the surface. The W method which does not use the continuity equation, gave inconsistent results from level-to-level probably because this approach is highly sensitive to errors in interpolated radial velocities. In the downward integration used for the final analysis, density was computed from the 1000 MDT South Park sounding, and then fitted with an exponential profile. The boundary condition  $w = 0$  was used at echo top. The accuracy of using  $w = 0$  at echo top is dependent upon the steadiness of the storm circulation and upon the distance between echo top and actual cloud top. The observed steady echo top of the analyzed mature storm indicates that errors due to rising and falling echo tops are minimal. If cloud top averages 500 m higher than echo top, then a maximum upper boundary vertical motion error of  $< 5 \text{ ms}^{-1}$  may be expected.

Additional errors in vertical velocity estimates are introduced from errors in estimates of Doppler-derived divergence which result from nonzero vertical motions of scattering particles. An analysis of this effect showed that downward integration of dual Doppler divergence estimates from storm top accumulates errors in estimated vertical velocities with decreasing height. Such an accumulative effect produces unreliable vertical velocity estimates at low levels. Thus, the vertical speeds given in section 5 should be regarded as semi-quantitative.

#### 4. CASE STUDY DESCRIPTION

##### 4.1 Synoptic Situation on 20 July 1977

On the morning of 20 July 1977 the synoptic pattern over North America was very weak. On the surface (Fig. 4.1), the major features consisted of a weak cold front, extending from Minnesota into northeastern Colorado and northwestward across Wyoming, and a trough to the lee of the Rocky Mountains from northern Kansas into northern Mexico. The trough was an extension of the surface low pressure center. There was little temperature and moisture contrast across the front in eastern Colorado. At 85 kPa (Fig. 4.2) a low level jet was located in western Kansas and the Texas Panhandle along the east side of the surface trough. By 1800 GMT, the cold front had been pushed south to the lee of the Rockies to the New Mexico border with well-developed northeasterly flow behind the front due to high pressure over eastern Montana, and breakdown of the lee surface trough. The onset of the northeasterly flow brought dew points as high as  $16^{\circ}\text{C}$  across most of the state. Northerlies persisted all day to the east of the foothills, but as will be discussed later, this synoptic flow was confined to the lower elevations over the plains and did not affect the local circulations that evolved over South Park. The 70 kPa analysis (Fig. 4.3) showed a very weak trough with weak flow extended from eastern Wyoming to west of Texas. The weak circulation around the 70 kPa low and cool tongue in southeastern Wyoming also induced a southward surge of the surface front. A region of high humidity at 70 kPa ( $T-T_d < 6^{\circ}\text{C}$ ) extended from

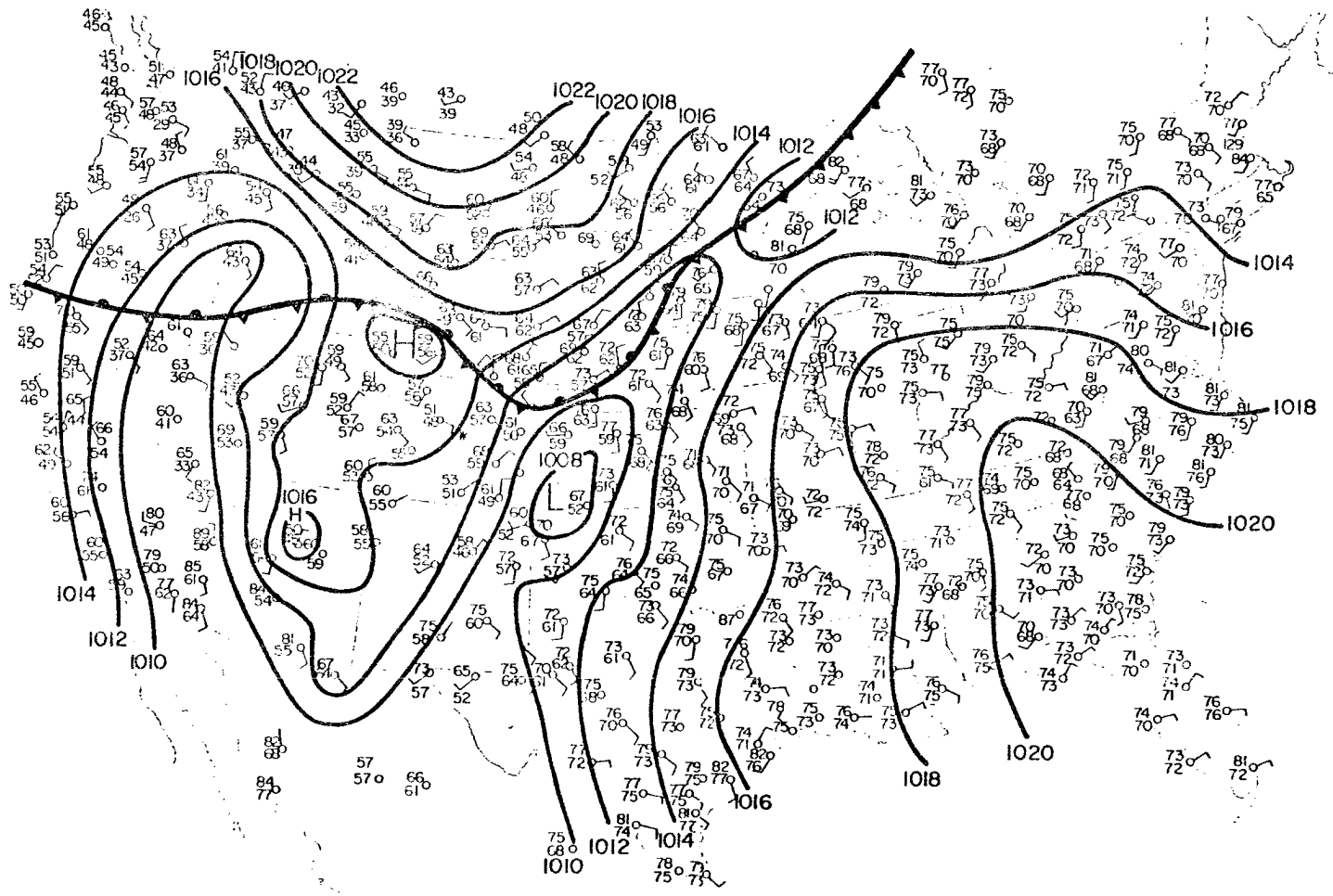


Fig. 4.1. Surface synoptic patterns for 0600 MDT 20 July 1977. The star denotes the location of South Park.

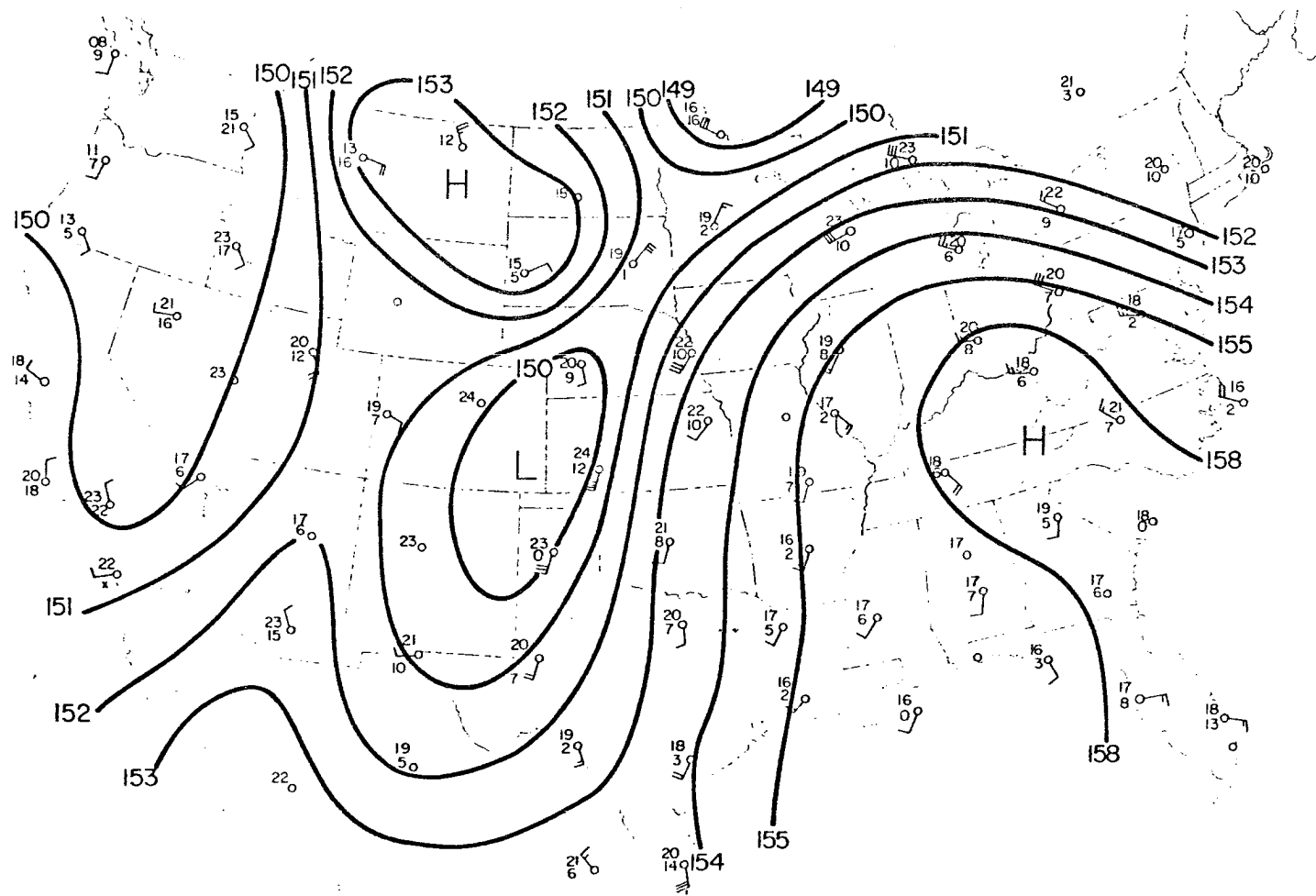


Fig. 4.2. 85 kpa analysis for 0600 MDT (12 GMT) 20 July 1977.  
Height contours are labelled in decameters.

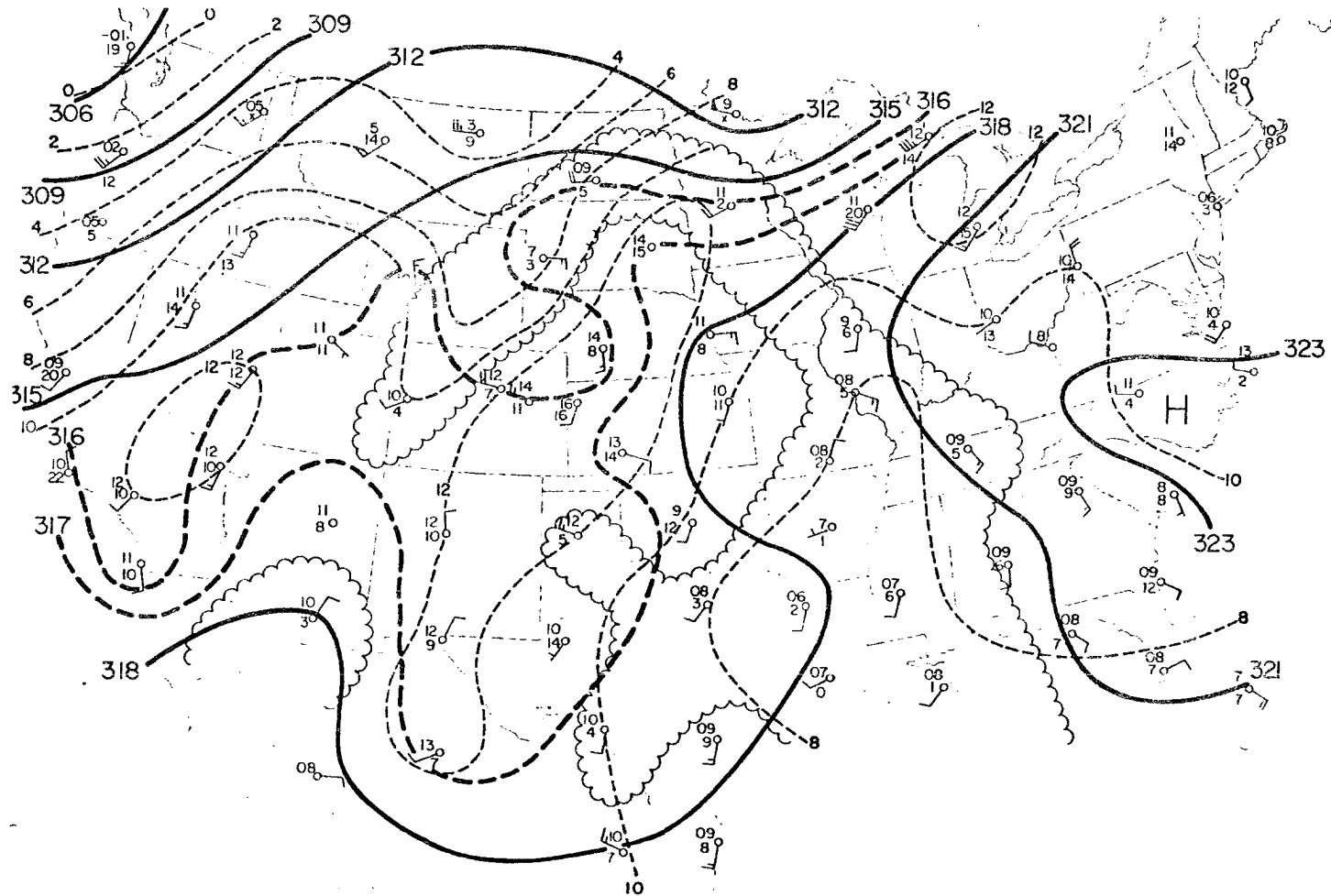


Fig. 4.3. 70 kpa analysis for 0600 MDT 20 July 1977. Areas with a dew-point depression ( $T - T_d$ ) less than  $6\text{ C}^\circ$  are marked. The primary contours (solid lines) are drawn at 30 m intervals, and secondary contours (heavy dashed lines) are drawn at 10 m intervals. Thin dashed lines depict isotherms.

southwestern Colorado northeastward in a band to North Dakota then inclined to the southeast. This eastward movement of the moisture advection pattern served to import substantial Gulf of Mexico moisture onto the eastern slopes of the Colorado Rockies during the day on July 20. The subtropical 50 kPa high pressure center (Fig. 4.4) elongated in a great arc across the U.S. with centers over the Oklahoma, west central Iowa, Michigan, and North Carolina. Baroclinic 50 kPa flow was confined to the Pacific northwest over the United States. In general, upper level flow (Fig. 4.5) over Colorado was weak ( $\sim 10 \text{ ms}^{-1}$ ) from the south and southwest, on the west side of a broad ridge over the eastern U.S. Little thermal and moisture advection was occurring, and the polar jet was located well to the north in southern Canada.

Satellite pictures taken at 1900 and 2000 GMT showed the north-south band of mountain convection formed over the Colorado Rockies, about 400 km long. This convective band appeared to be independent of the surface front, and more in line with 70 kPa trough (Fig. 4.6). Late in the afternoon the entire Colorado mountain region was under deep convection. The deepest area of convection appeared to be centered over South Park and to the north.

#### 4.2 Mesoscale Soundings

Three rawinsondes were released from the base station on 20 July 1977 at 0600 Mountain Daylight Time (MDT), 1003 MDT and 1355 MDT. Data quality were generally quite good, and there were no tracking problems. At 0600 MDT the South Park sounding (Fig. 4.7) showed a thin, nocturnal radiation inversion topped by a near-neutral layer to 68 kPa. Moisture values in the lowest level of the sounding ( $7.5 \text{ gm Kg}^{-1}$ ) were relatively high for South Park elevations in northern Colorado. Assuming a 10 kPa

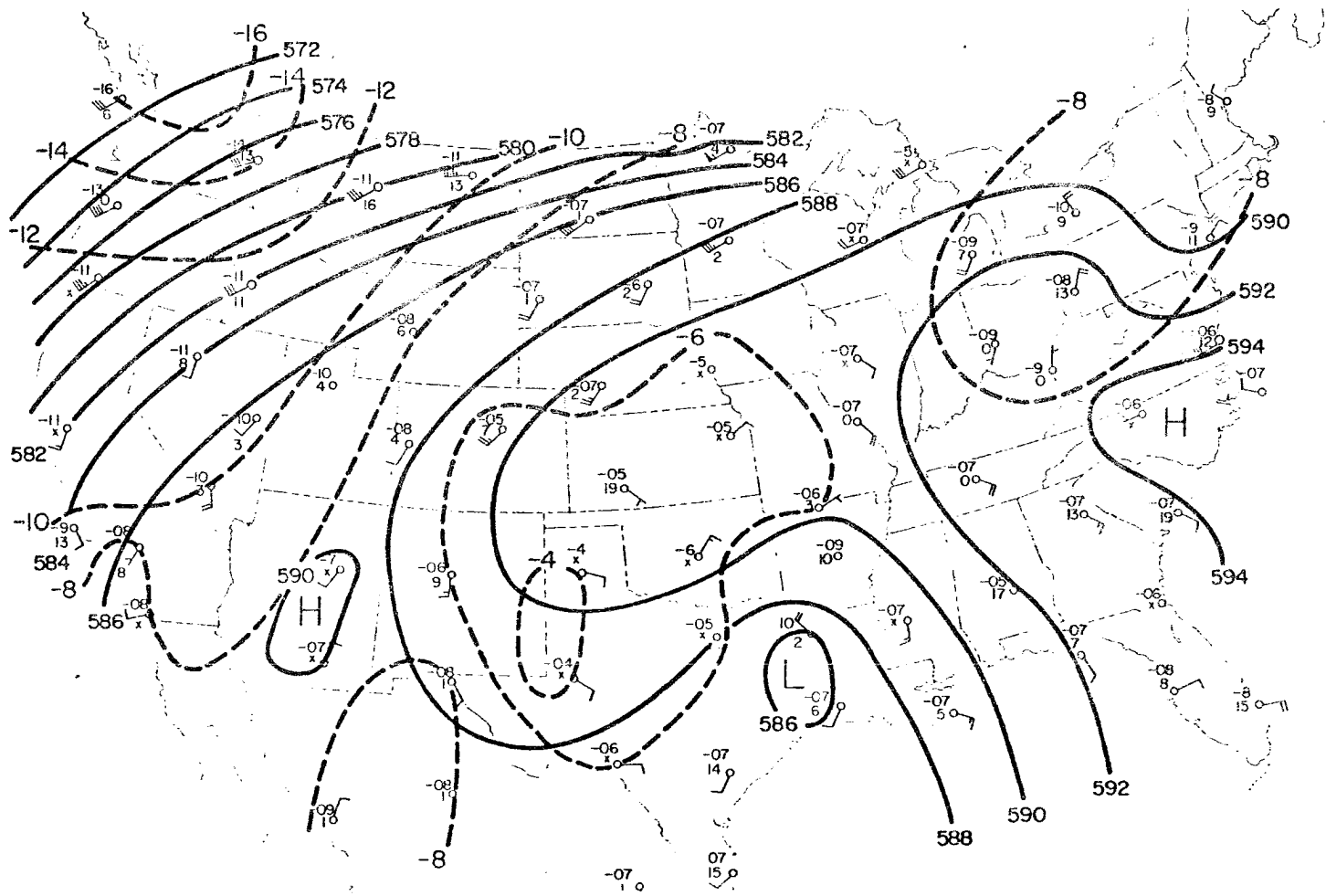


Fig. 4.4. 50 kpa analysis for 0600 MDT 20 July 1977. Height contours are labelled in decameters. Dashed lines depict isotherms.

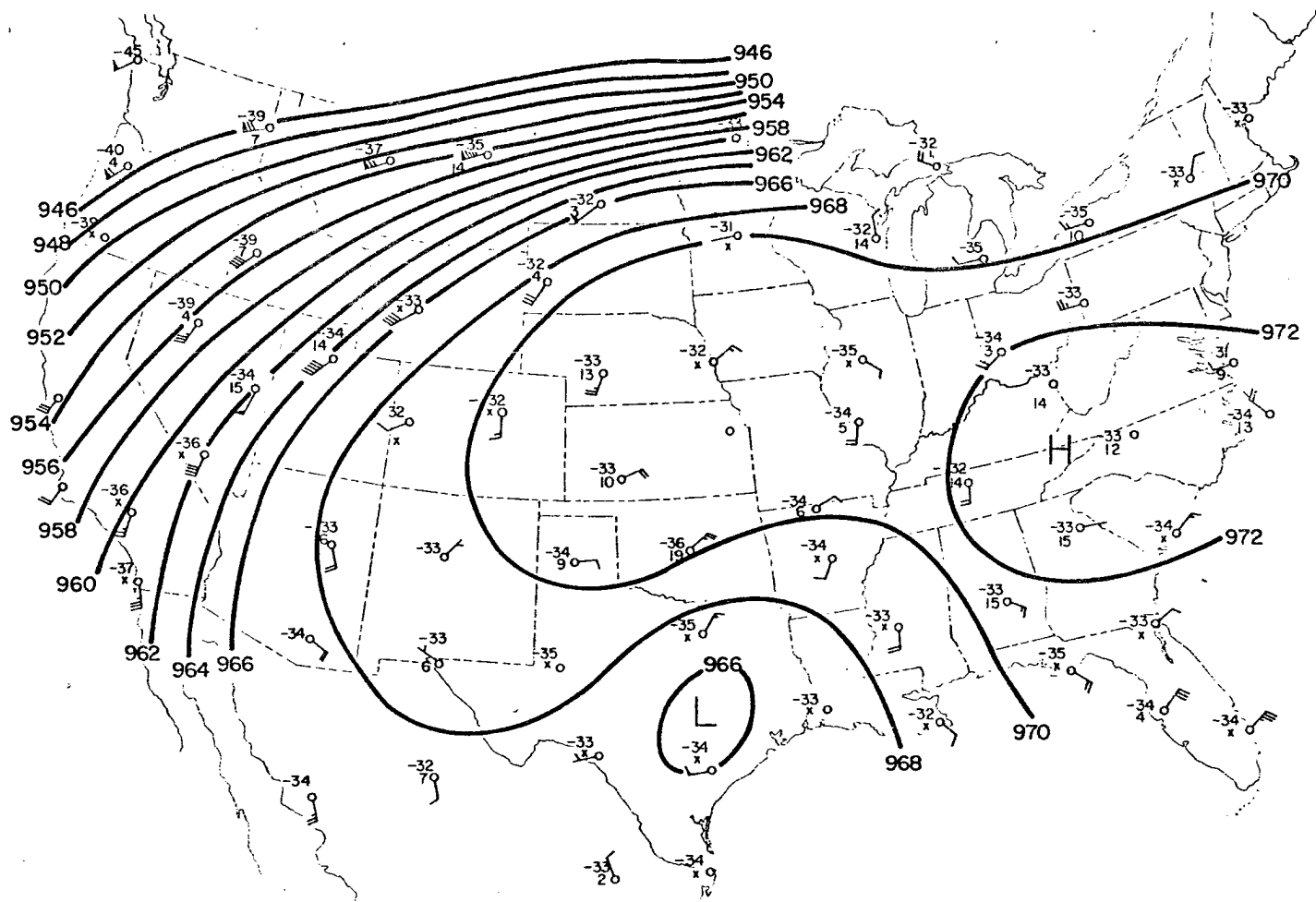


Fig. 4.5. 30 kpa analysis for 0600 MDT 20 July 1977. Height contours are labelled in decameters.

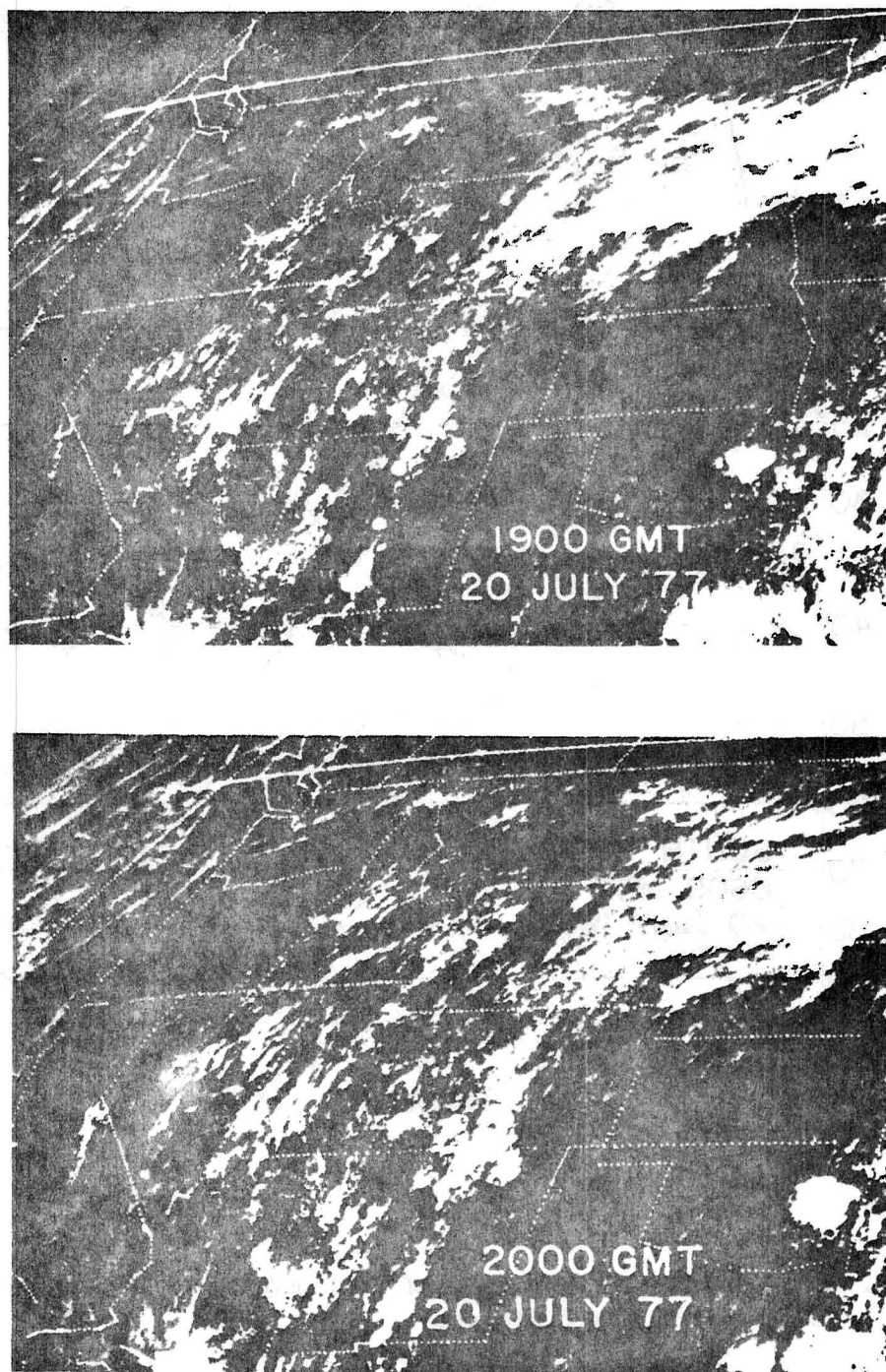


Fig. 4.6. Visible satellite images of the western United States, for 1900 and 2000 GMT, 20 July 1977. Dotted lines are state boundaries.

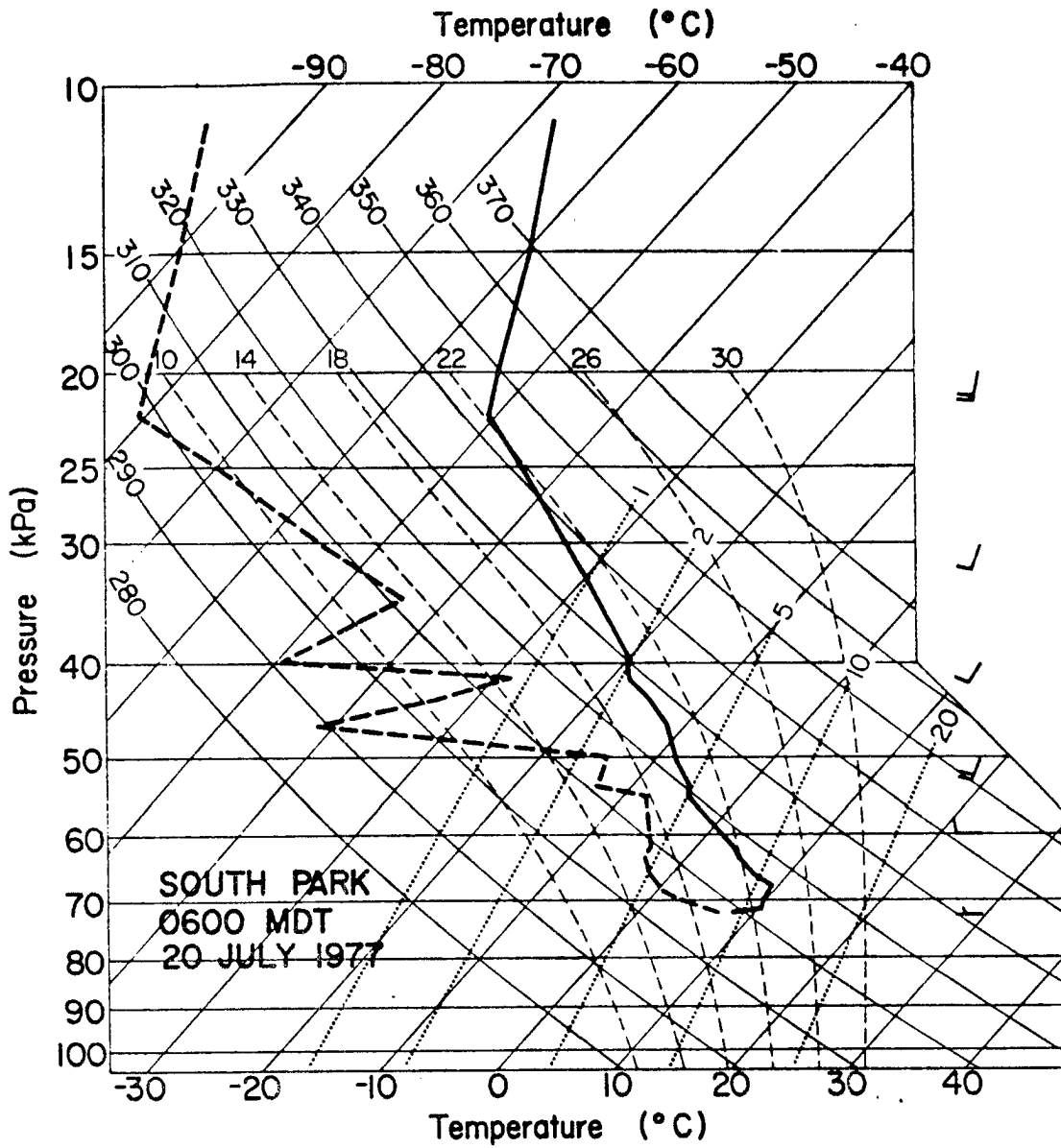


Fig. 4.7. South Park sounding of 0600 MDT 20 July 1977, plotted on skew-T log-P diagram.

mixed surface layer with mixing ratio of about  $7.5 \text{ g kg}^{-1}$ , a low-level parcel heated to  $17 \text{ C}^{\circ}$  could reach its convective condensation level (CCL) of 63 kPa. A cloud with its base at the CCL would be capped by the stable layer at 42 kPa, but if this stability were eliminated, the cloud parcel then could rise undiluted to at least 30 kPa before losing buoyancy. Winds were generally westerly in the lower and southwesterly aloft.

The 1003 MDT South Park sounding (Fig. 4.8) is considered to be representative of the storm environment. The initial nocturnal inversion at 0600 MDT was destroyed as a mixed layer had formed within the inversion. Winds from the earlier sounding were basically westerly near the surface. By 1003 MDT, winds had begun to turn easterly, indicated the initiation of the upslope/up-valley circulation. This sounding also indicated substantial moistening at all levels since the early-morning sounding. Above the CCL, the higher dew points resulted from eastward moisture advection. The moistening of the layer below the CCL was probably due to convective transport of moisture over a surface-based convergence line (southeasterly upslope over central South Park, westerly at ridge-top level). Abundant moisture was present in the lowest 100 mb, with a maximum mixing ratio of  $10 \text{ g Kg}^{-1}$  at the surface. A layer of conditionally unstable air extended from 67.5 kPa to 46.9 kPa, and a  $0.8 \text{ C}^{\circ}$  inversion to 45.8 kPa. A relatively large (for South Park) parcel method temperature excess of 3 to 4 K was estimated over a fairly deep layer. Assuming a 10 kPa mixed surface layer with mixing ratio of about  $7.5 \text{ g kg}^{-1}$ , a low-level parcel heated to  $19 \text{ C}^{\circ}$  could reach its convective condensation level (CCL) of 60 kPa. A cloud with its base at the CCL would reach saturation at about 50 kPa,

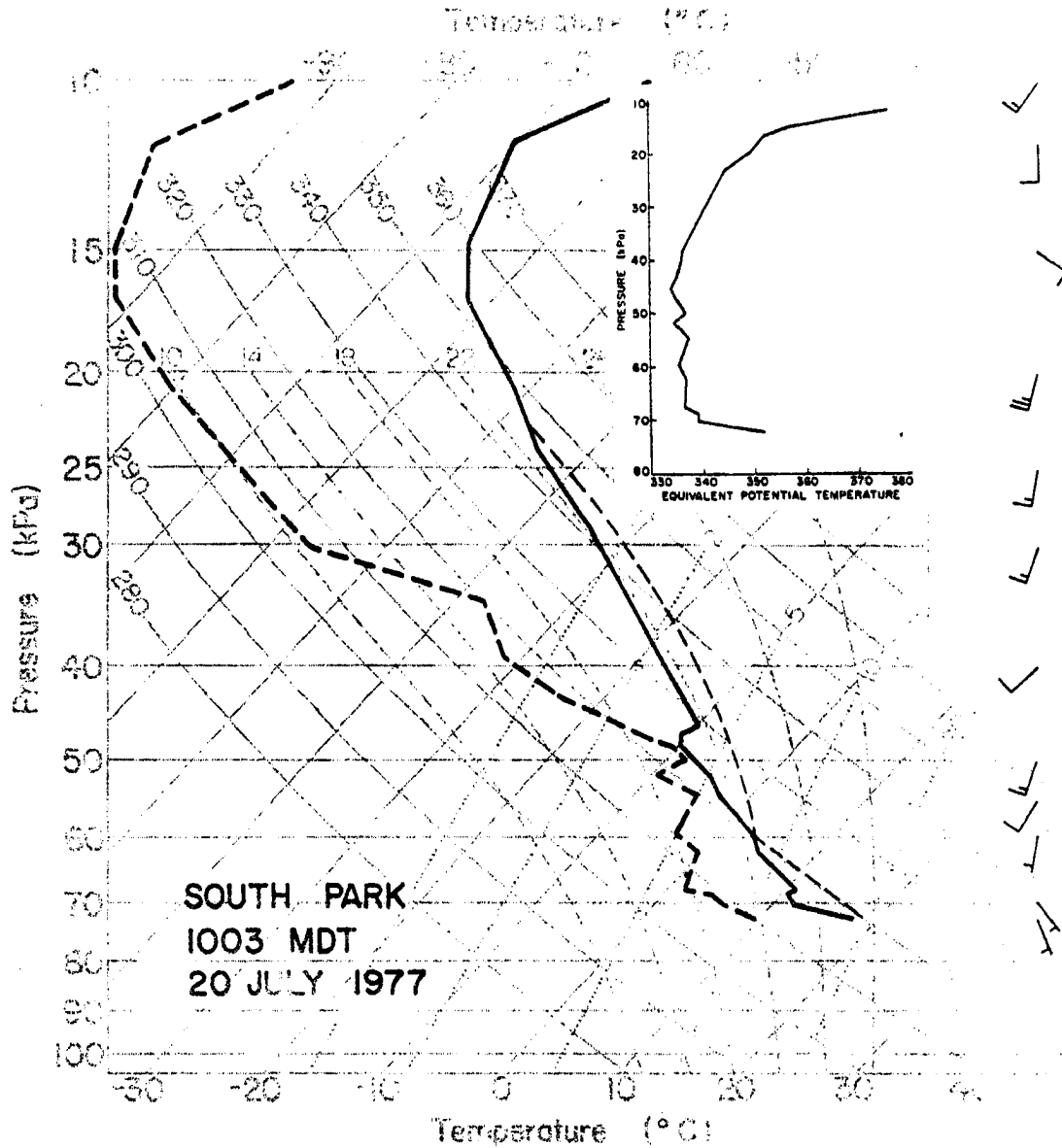


Fig. 4.8. South Park sounding of 1003 MDT, 20 July 1977, plotted on skew-T log-P diagram. Inset shows the corresponding equivalent potential temperature profile. The approximate trajectory of a parcel lifted from the surface is depicted by the thin-dash line.

and could rise to a potential cloud top of 26 kPa before losing buoyancy. Winds were easterly below mountain top and southwesterly above, and never exceeded  $10.5 \text{ m sec}^{-1}$ . The corresponding profile of the equivalent potential temperature ( $\theta_e$ ) is shown in the inset of Fig. 4.8. As seen from this profile, environmental equivalent potential temperature decreased from a maximum value of 352 K at the surface to a minimum of 334 K at a height of 4.6 km (45 kPa). Above this minimum,  $\theta_e$  again increased, but more slowly, reaching a value of 350 at 10 Km near the top of the radar echo. Note,  $\theta_e$  was nearly constant from 68 kPa to 43 kPa. The potentially cold dry air at middle level could contribute significantly to a deep downdraft circulation, provided it can be kept near saturation during its descent. The schematic models (Browning, 1964; Frankhauser, 1971; Knupp and Cotton, 1982) have also emphasized the role of middle level potentially cold air for invigoration of the downdraft. The observed internal kinematic structure will be shown to be consistent with these environmental conditions.

Conditions favorable for cumulus cloud formation or propagation over the South Park did not occur until after 1200 MDT, when a potential temperature of 320 K was present at most of the surface stations. The 1355 MDT South Park sounding showed the influence of this deep thunderstorm activity on the South Park environment. Downdrafts from the precipitating cumulus clouds which passed near the base station served to stabilize the lowest 4 kPa. Above this, a well-mixed neutral layer extended to 58 kPa. A deep mid-to upper level tropospheric layer (55-25 kPa) continued the substantial moistening and slight warming trends.

The hodograph in Fig. 4.9 was derived primarily from the 1003 rawinsonde data. These data have been smoothed in the vertical to reduce possible wind errors. In general, there was insignificant wind shear in the lower level. Wind near the surface (PBL) was light and southeasterly, then became SW in mid-to upper troposphere with maximum wind speed at about  $10 \text{ m sec}^{-1}$  in upper troposphere. At 1355 MDT, wind at the surface was light and northerly, then turned to WSW at about  $4 \text{ m sec}^{-1}$  in the lower troposphere up to the mid troposphere. In the upper troposphere wind was southerly at about  $10 \text{ m sec}^{-1}$ . A comparison of this wind profile with the wind hodograph at 1003 MDT indicated that the boundary layer wind became westerly after the storm moved eastward of South Park. Also, mid tropospheric winds were southwesterly, but 2 or 3  $\text{m sec}^{-1}$  lighter than they were at 1003 MDT. As a consequence, the absence of the significant steering level flow ( $\sim 50 \text{ kPa}$ ) allowed the storm to be quasi stationary which moved eastward at about  $5 \text{ m sec}^{-1}$ . Thus, synoptically weak environmental wind shear differentiates this storm from the severe storms of the Great Plains where low-to mid level shear is usually much greater.

Fig. 4.10 shows the magnitude of the difference between the storms inflow horizontal momentum ( $\rho_0 V_0$ ) and environmental horizontal momentum ( $\rho_z V_z$ ),  $|\rho_0 V_0 - \rho_z V_z|$ , where zero subscripts denote inflow quantities and z subscripts represent environmental quantities as a function of height. Fig. 4.10 indicates that the primary maximum occurs at a height of 4 km MSL, with a secondary maximum occurring at a height of 7.5 km MSL. Comparison of the Fig. 4.10 profile with the Knupp and Cotton (1982)'s profile for 19 July South Park storm indicates that in their case the profile was much stronger than this case (about factor of 2).

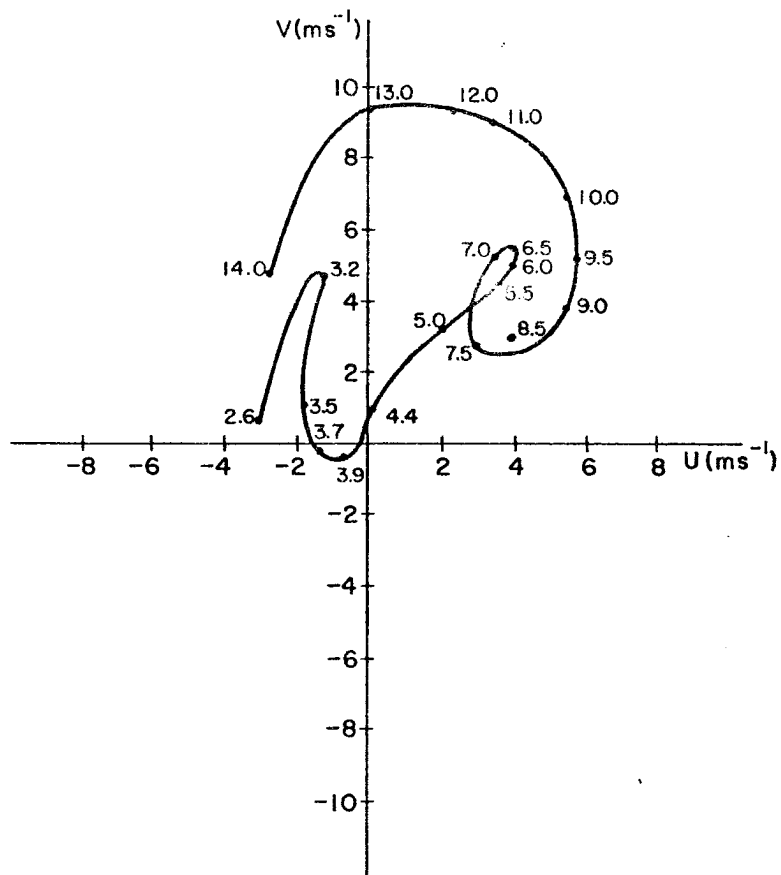


Fig. 4.9. Environmental wind hodograph derived from the 1003 EDT South Park sounding. Numbers adjacent to hodograph curve denote height in km MSL.

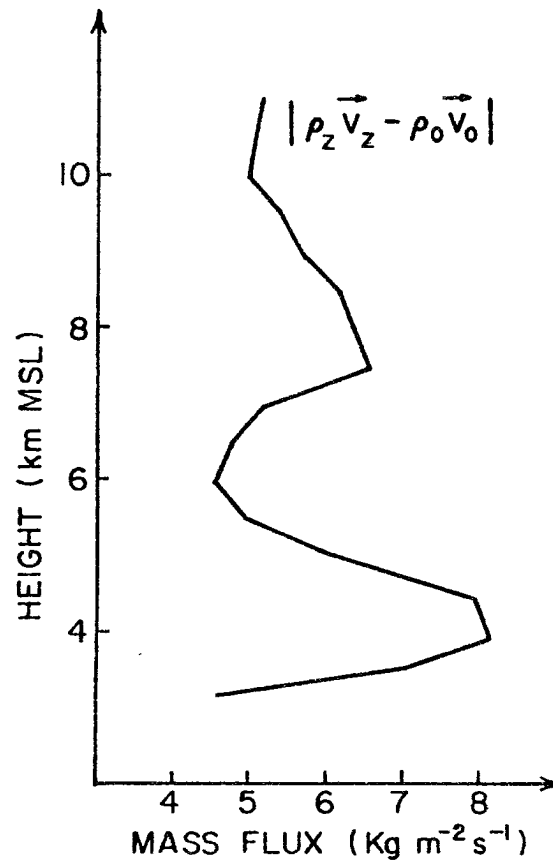


Fig. 4.10. Vertical profile of the magnitude of the difference between low-level momentum ( $\rho_0 \vec{V}_0$ ) and environmental momentum ( $\rho_z \vec{V}_z$ ).

This may help to explain less diversion of the ambient flow about updrafts and creation of inflow entrainment into the wake low pressure zone, and probably weaker dynamic forcing for the intrusion of low-valued  $\theta_e$  air into the storm.

#### 4.3 General Echo Characteristics

As mentioned earlier, conditions favorable for cumulus cloud formation over the South Park basin did not occur until after 1200 MDT. Shortly after 1200 MDT, the CP-3 radar began recording data. The evolution of the 5.5° elevation reflectivity patterns of convective cells is depicted in Fig. 4.11. Echoes assumed a variety of sizes, shapes, and intensities on 20 July 1977. These data, when compared with 1973 South Park echo data compiled by Huggins (1975), indicate that cell characteristics, including maximum echo top and echo intensity are well above normal for South Park thunderstorms. The first precipitating radar echoes formed over the eastern slope of the Mosquito Range around 1217 MDT. This location was found by Huggins (1975) to be the most likely place for first echoes to form in the South Park area. In this area easterly slopes winds would create low level convergence on the eastern slope of the Mosquito Mountains, producing the so called 'hot spot' thunderstorm. Hot spots are the zones of preferred echo frequency (Henz, 1974). Reflectivity fields showed that the radar echoes moved off mountains from the west into the northern edge of South Park. The radar field of view toward the northern sector was extremely poor because of ground clutter. Little information was available on the mountain convection over the northern part of South Park, but satellite and Limon radar data confirmed that it was relatively weak convective activity compared to the intense convection to be described. As time

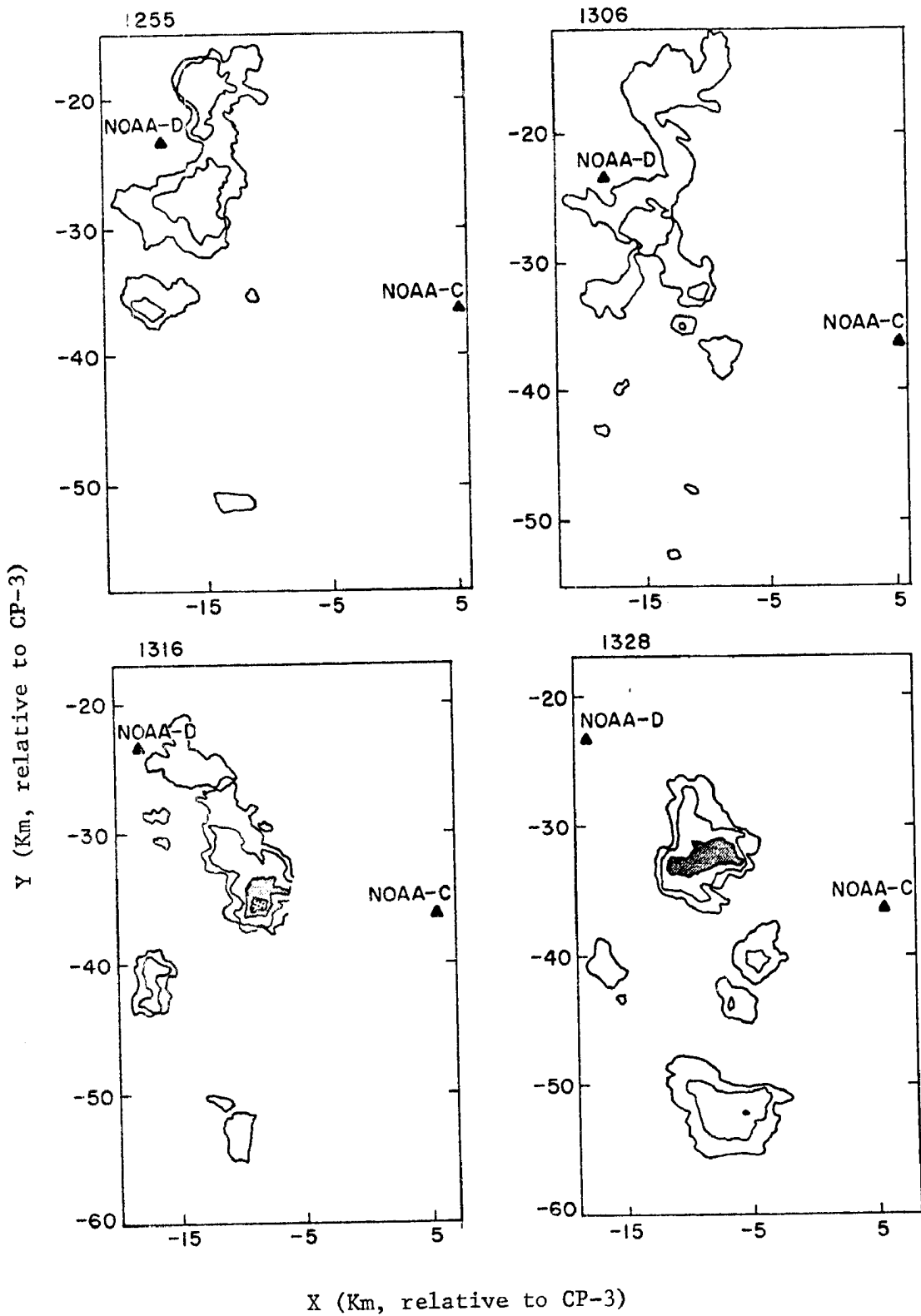


Fig. 4.11. Echo evolution of individual cells at various times (MDT). Echo contours (from CP-3  $5.5^\circ$  PPI) are drawn at 20, 30, 40 and 50 dBZ, with echo intensities greater than 40 dBZ shaded. Radar locations are denoted by triangles.

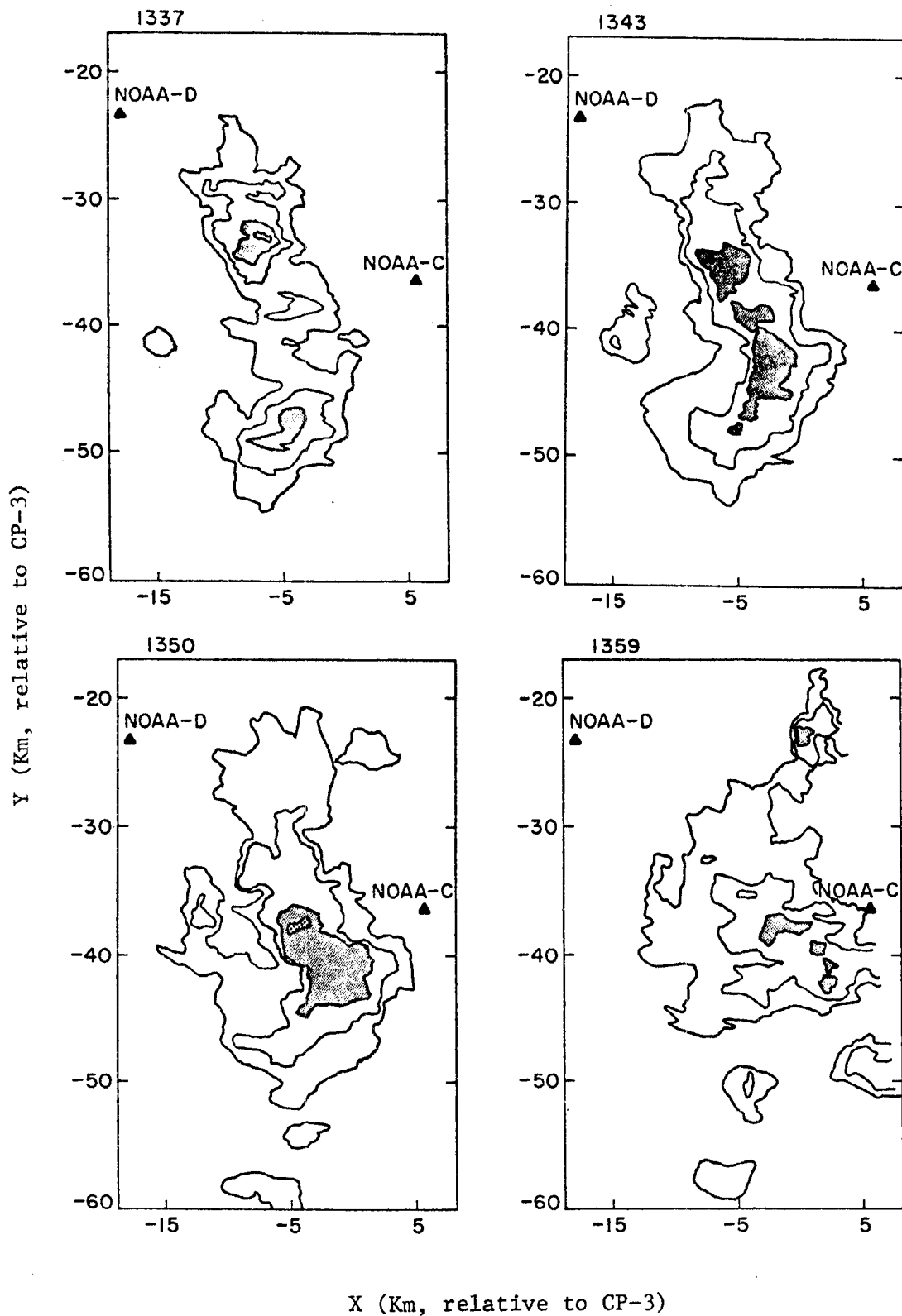


Fig. 4.11. (Continued)

proceeded, the radar echoes continued a slow eastward movement into South Park, apparently due to the weak steering flow aloft. By 1236, one of the cells near NOAA-D radar rapidly intensified to 40 dBZ reflectivity as a consequence of merging of several weaker cells. Following the initiation of this cell, new cells began to form about 10 Km south of NOAA-D radar. At 1255, the intensity of the strongest cell decreased considerably. At this time and shortly after (1306 MDT), several cells merged into a single reflectivity line. Some of the noteworthy features of this storm were its north-south orientation, and its multicellular nature with discrete propagation of cells at the SE flank of the storm due to its translational component. This organization resembles the July 19 storm analyzed by Cotton et al. (1982). By 1316, an intense storm had formed on the southeastern side of NOAA-D radar. This cell, which was partially merged with another cell to the south, had attained its greatest reflectivity (50 dBZ) and highest 20 dBZ echo top (14 Km MSL). This storm also showed an echo top rising about  $9 \text{ m sec}^{-1}$ . The radar echo top at 14 Km MSL indicates that the increased boundary layer moisture ( $q_v = 10.5 \text{ g Kg}^{-1}$ ) helped to support very deep convection. Following the intensification of this storm, new cells began to form over the relatively flat Park area along a low-level convergence zone. At 1328, this echo line became more contiguous and expanded towards the southern end of South Park. The evolution of the reflectivity structure of this storm showed a unicellular stage at this time. Subsequent  $5.5^\circ$  elevation PPI scans at 1337, 1343, 1350 and 1359 portrayed a more multicellular stage of this cell group.

By 1337, the dominant features were two intense cells to the southeast of NOAA-D radar. The two cells merged into a single cell by 1350, and was the strongest cell over South Park. Merging occurred as a consequence of the intersection of the gust fronts from two intense cells. Various characteristics of this storm will be discussed in greater detail in the following section. By 1359, reflectivities began to decrease considerably, but, some small new cells started to form in South Park with short echo lifetime.

#### 4.4 Overview of Storm and Mesoscale Surface Features

This section provides a framework for detailed Doppler analyses presented later and the interpretation of the interaction of Doppler radar inferred flow fields with surface data. As previously noted, the northeasterly flow behind the surface front was too shallow to advect moisture into South Park. Therefore, the observed increases in surface moisture before the onset of deep mixing must have come primarily from local evaporation or advection from neighboring river valley floors. Preliminary analyses of several other cases indicate that larger scale advection of moisture from the Plains westward into South Park by slope winds is most likely to occur in the late afternoon. Thus, moisture that has its origins in the Gulf of Mexico and that helps fuel early afternoon thunderstorms over South Park is likely to have arrived the day before (Cotton et al., 1982). On 20 July 1977, sufficient low level moisture was already present in South Park, which, when coupled with advection of moisture by upvalley and upslope flow provided favorable conditions for development of deep moist convection. Surface mixing ratios of 8-10 gm Kg<sup>-1</sup> were already high compared to other days in South Park.

The PAM network provided surface data from 20 different locations at any one time. A subjective streamline analysis has been drawn to represent general flow directions. Due to the limited number of PAM stations and the irregularity of terrain on the boundaries of the network, an objective streamline analysis was not attempted. Meanwhile, plotted winds and thermodynamic variables were based on three-minute averages centered on the analysis time.

The surface flow in South Park on the early morning of 20 July evolved in a manner quite typical for weak summertime synoptic situations. A well-established drainage flow (westerly to northwesterly) of cool air was indicated in central South Park at 0600 MDT. This drainage flow regime served to pool stable air in the lower areas of the Park overnight. After sunrise, surface heating below of the cold pool caused a gradual erosion of the nocturnal inversion layer from below and also produced valley/upslope flow within the heated layer next to the ground. When the valley/upslope regime became well established during the later morning hours (Fig. 4.12), the east-facing slopes of South Park were a region where upslope winds with an easterly component blowing up from the lower areas of the valley, met with convectively-mixed winds with a westerly component, blowing downward from the direction of the ridges. The region of confrontation between the two wind regimes generated a line of convergence. The convergence line subsequently propagated down the slope. A similar temporal development was also described by Banta and Cotton (1982) in several case studies. For the case of July 20, the convective clouds first formed along the eastern slopes of the Mosquito Range west and northwest of South Park at 1217 MDT. As these clouds intensified and convergence increased, the

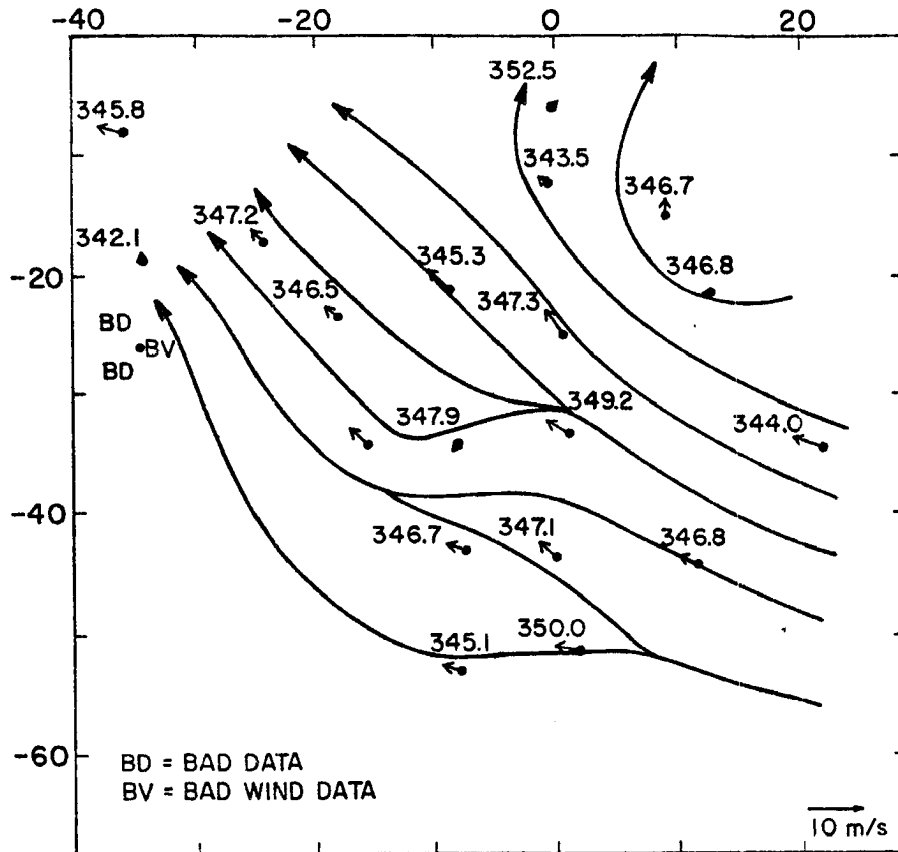


Fig. 4.12. PAM mesonet surface streamline analysis at 1100 MDT. Plotted values are wind vectors (maximum vector  $10 \text{ m s}^{-1}$ ) and equivalent potential temperature. The coordinate origin is located at CP-3 radar.

intense downdraft laterally spread out beneath the convective cloud and a strong gust front marked its leading edge. The passage of the gust front was verified by a strong gust of relatively cool air and a jump in pressure. The gust front provided low-level convergence which corresponded to the eastward propagation of the system from the mountain slopes over the flat regions of South Park.

The CP-3 radar began recording data at 1217 MDT. The PAM network, however, was completely out of service from 1230 to 1313, and 1335 to 1345 MDT. Thus, the earliest available period for the combined PAM-radar analysis was at 1316 MDT (Fig. 4.13). In this figure, PAM surface winds and equivalent potential temperature were superimposed with  $1.5^{\circ}$  elevation, Plan Position Indicator (PPI) scans from the CP-3 radar. Several convective echoes were present on the south edge of the Park, with a strong cell just southeast of NOAA-D. Three gust fronts depicted in Fig. 4.13 resulted from the coalescence of several storm outflows. The locations of the gust fronts on all the PAM-radar maps was estimated from PAM surface data by determining the time of the windshift, accompanied by a rapid temperature drop, and pressure jump. The gust front A north of the echoes in Fig. 4.13 was generated by another complex extending northward into the mountains from the northern portion of South Park. Limon radar and satellite data confirmed this activity. As seen in Fig. 4.13, the north end of South Park was covered by cool, moist northerly air, originating from downdrafts of convective clouds in the mountains to the north. It is hypothesized that the cool, more dense downdraft air flowed down the generally southward sloping terrain providing a northerly surface wind component. A similar southward moving meso-cold front was observed by Cotton et al. (1982) on July 19,

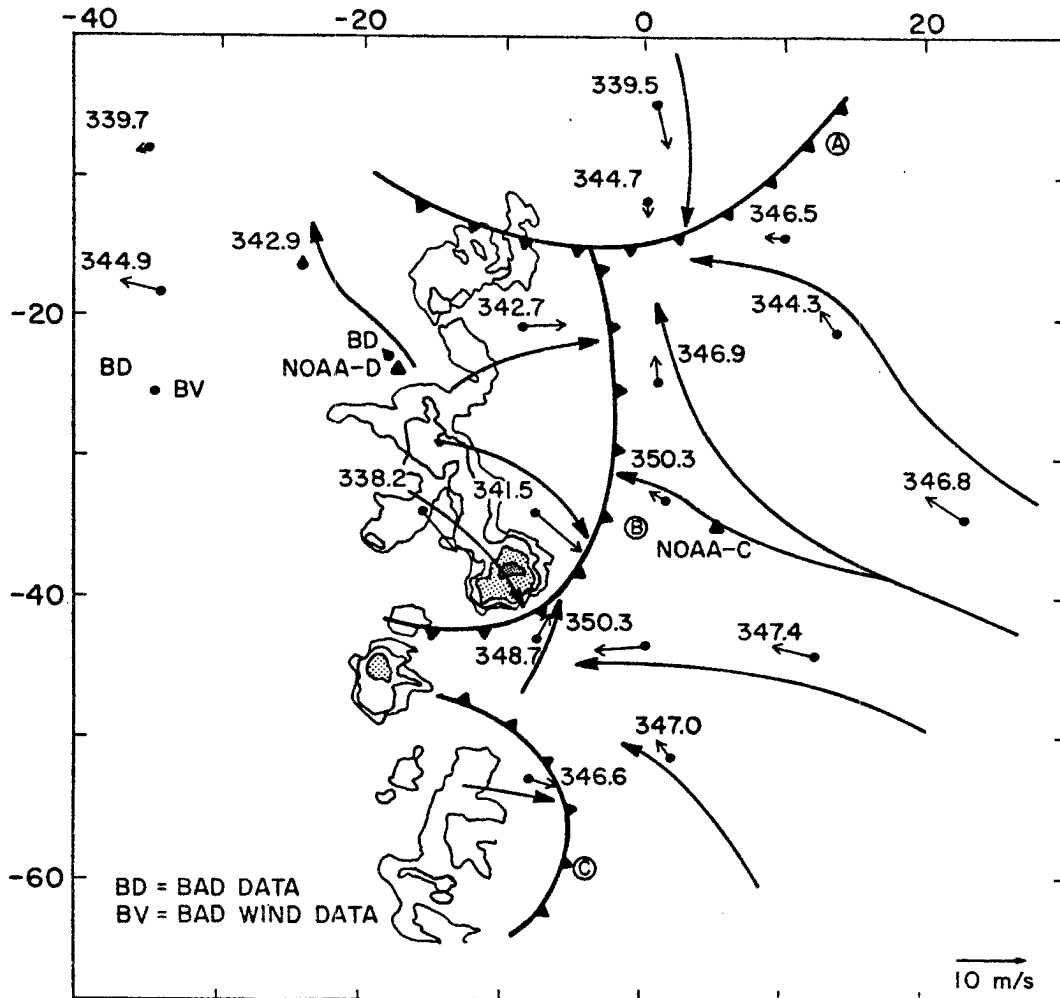


Fig. 4.13. Composite PAM-CP-3 radar plot for 1316 MDT, 20 July 1977. Three-minute averaged equivalent potential temperature ( $^{\circ}\text{K}$ ) and winds are plotted at each station. Radar contours are  $1.5^{\circ}$  constant elevation scans, projected onto a horizontal surface. Echo contours are drawn at 20, 30, 40 and 50 dBZ, with echo intensities greater than 40 dBZ shaded.

1977. Gust front B was the strongest gust front at this time, and emanated from a cluster near the NOAA-D radar. Winds behind gust front B were northwesterly. Since  $\theta_e$  is approximately conserved following air-parcel motion in the absence of mixing, therefore, reduced  $\theta_e$  values (as low as  $338^{\circ}\text{K}$ ) in the divergent flow behind the gust front B, as well as in the chilled air at 45 kPa of the 1003 MDT South Park sounding (Fig. 4.8), indicate that this air must be transported downward at least from above cloud-base level or from the mid-troposphere. At the eastern edge of the Park, easterly upslope/upvalley flow transported warm, moist air to the Park. The intersection of gust front B and the easterly upslope flow generated a strong convergence. The enhanced convergence forced inflow air up and into the updraft which caused the cloud to sustain itself longer. Gust front C was barely evident at the extreme southern portion of PAM. The location and extent of the convective activity can be seen on a satellite infrared (IR) image (Fig. 4.14) taken at 1915 GMT (1315 MDT). The enhancement scheme used was the MB curve (Corbell et al., 1975), at this very small scale of analysis, interpretation of individual pixel values was very difficult. The cold cloud top ( $-56^{\circ}\text{C}$ ) was associated with the thunderstorm in South Park over CP-3 radar (convective complex B in Fig. 4.14 at 1915 GMT). This convective complex was above the maximum scanning angle of CP-3. Further to the south a large, more mature convective complex (complex A at 1915 GMT) existed with apparent blackbody temperatures colder than  $-53^{\circ}\text{C}$ . As time proceeded, little changes in surface quantities and flow patterns were observed in South Park, but as mentioned earlier, new cells began to form and intensify along a low-level convergence zone.

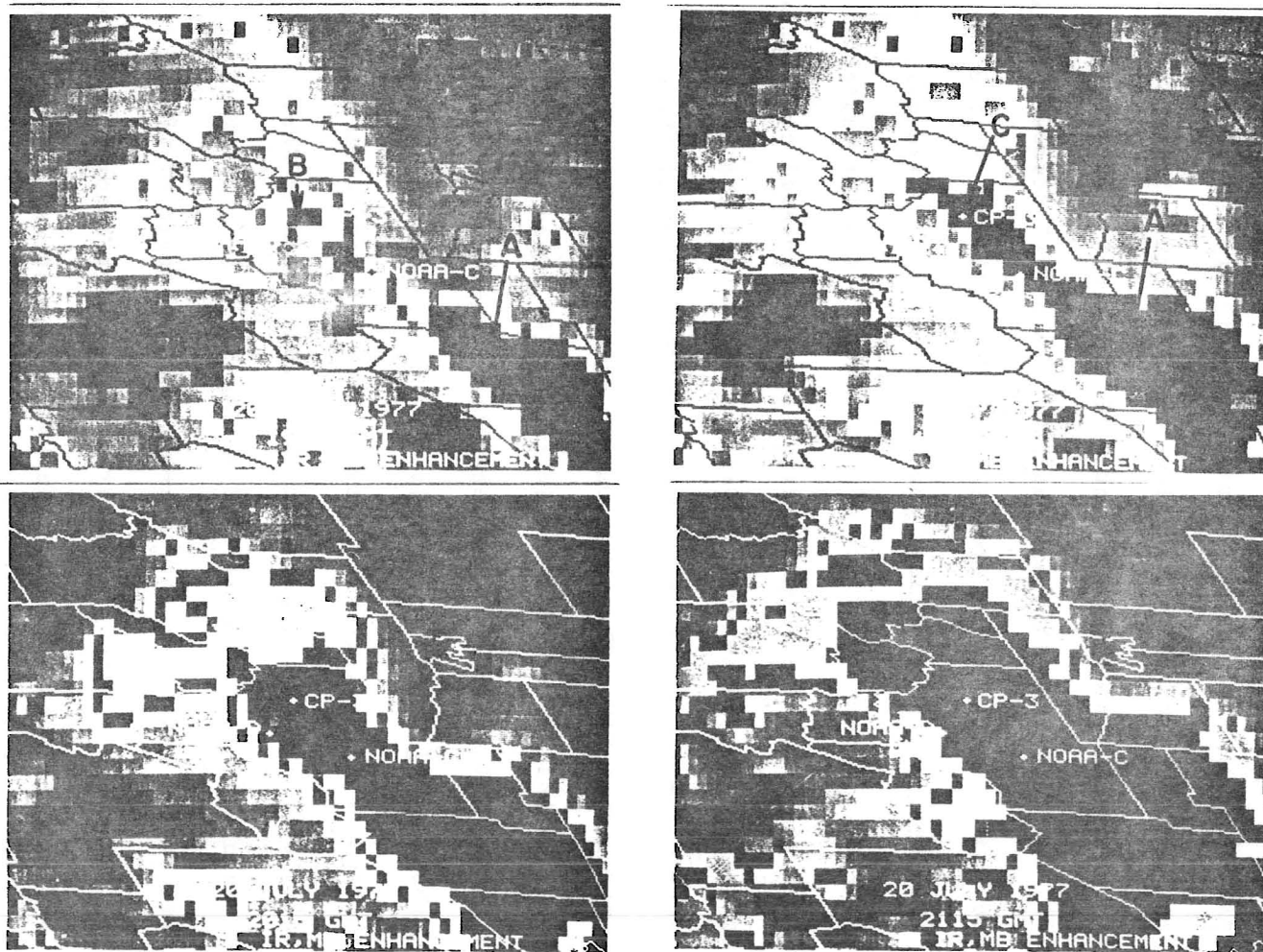


Fig. 4.14. Infrared (IR) satellite images of central Colorado for 1915, 1945, 2015, and 2115 GMT. The stepped gray shades of medium-gray, light-gray, dark-gray, and black are thresholds for areas with apparent blackbody temperatures colder than  $-32$ ,  $-42$ ,  $-53$  and  $-59^{\circ}\text{C}$ , respectively.

At 1328, this echo line became more continuous and expanded toward the south.

By 1350 MDT, two intense (50 dBZ) cells in the line merged into a single cell to the southwest of the NOAA-C radar. This cell had intensified and was the strongest storm in South Park (Fig. 4.15). The interaction of downdrafts or gust fronts from two intense cells appeared to be the primary mechanism of this merging process as suggested by Simpson et al., (1980). The approach or collision of downdrafts from adjacent cells forced more upward warm moist air into the cloud. This will be discussed in greater detail in chapter 5. Merging appeared to be a major way in which convective clouds became larger. Shortly after this merger had occurred, heavy rains began at station #27, producing a one-minute rainfall rate of  $230 \text{ mm hr}^{-1}$  (Fig. 4.16). This compares to the previous rainfall rate maximum, associated with non-merging storms, of  $130 \text{ mm hr}^{-1}$ . Therefore, consistent with the findings of Simpson et al., (1980) over south Florida, the merging process coincided with more rain than occurred in unmerged echoes.

At this point, it is necessary to mention that multiple Doppler radar observation of low-level outflow was not possible because downdraft outflow was below the level of multiple Doppler radar coverage. The radial velocity detected with the CP-3 radar at a 0.4 deg. elevation was about  $14 \text{ ms}^{-1}$  within the storm low-level outflow air. The area of these strong winds were confined to the lowest 350 m. Fujita (1981) inferred that the maximum wind of the horizontal downburst flow was located 50 m above the ground. At 1349, gust front A slowly moved southward, while gust front B moved eastward, but convection supporting it began to weaken. Gust front C moved northeastward, and

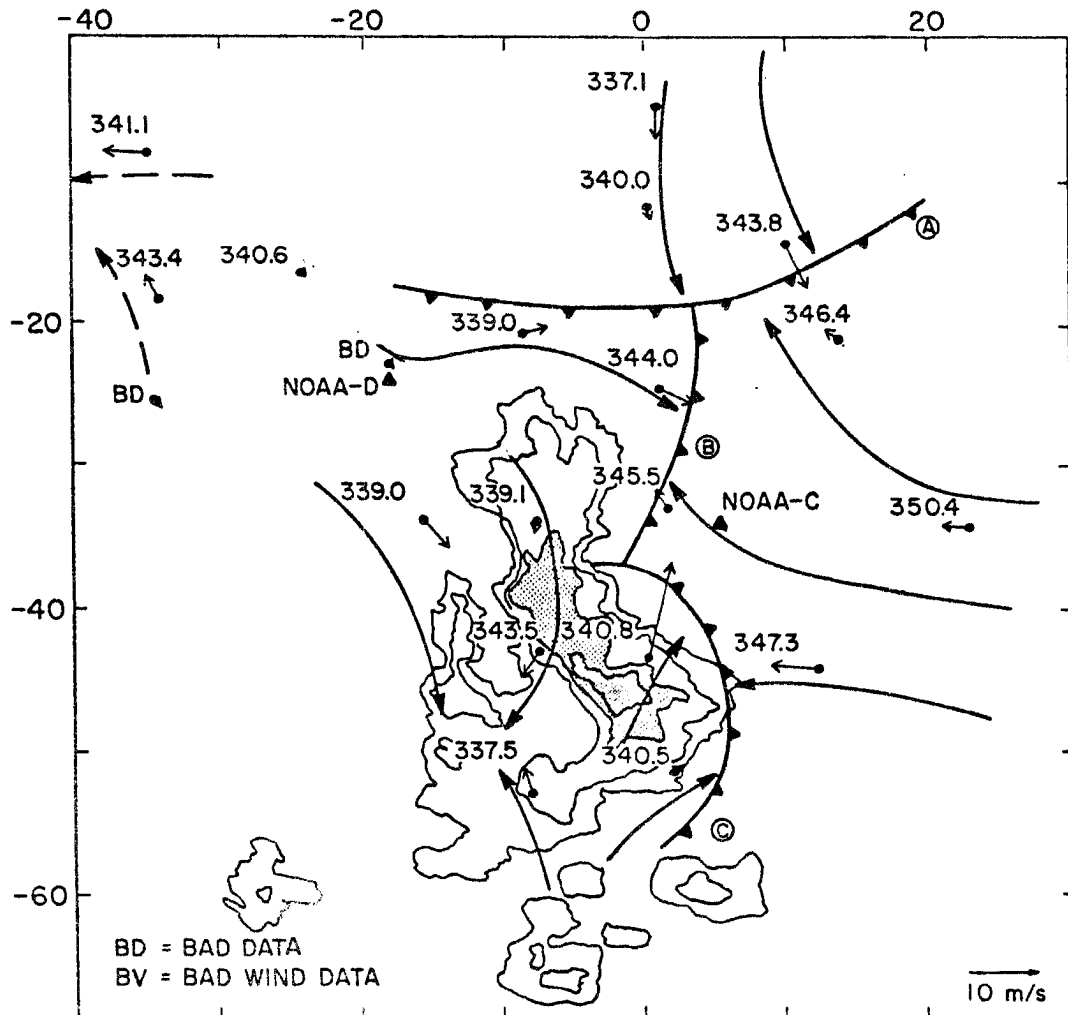


Fig. 4.15. Same as Fig. 4.13, for 1349 MDT.

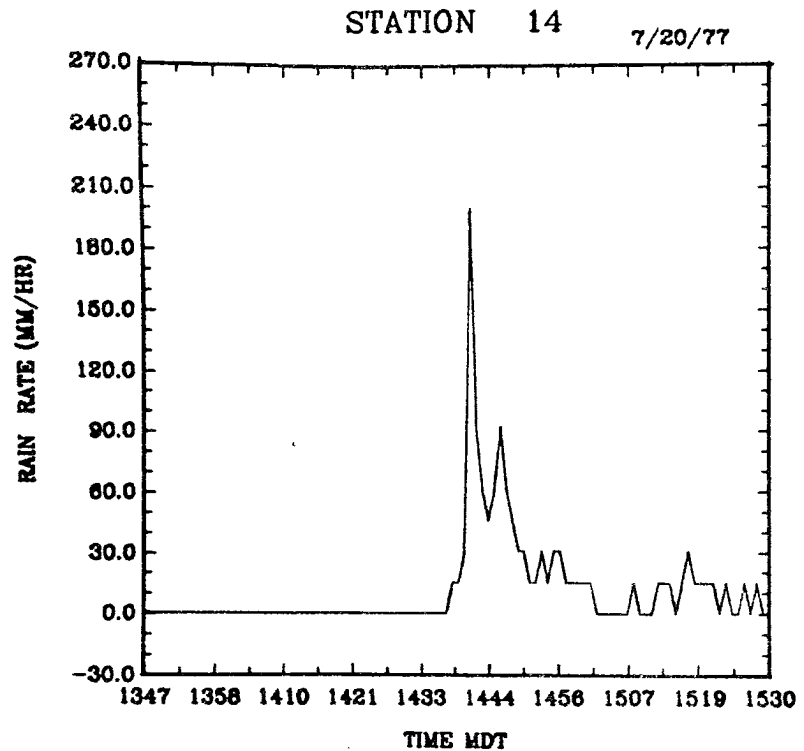
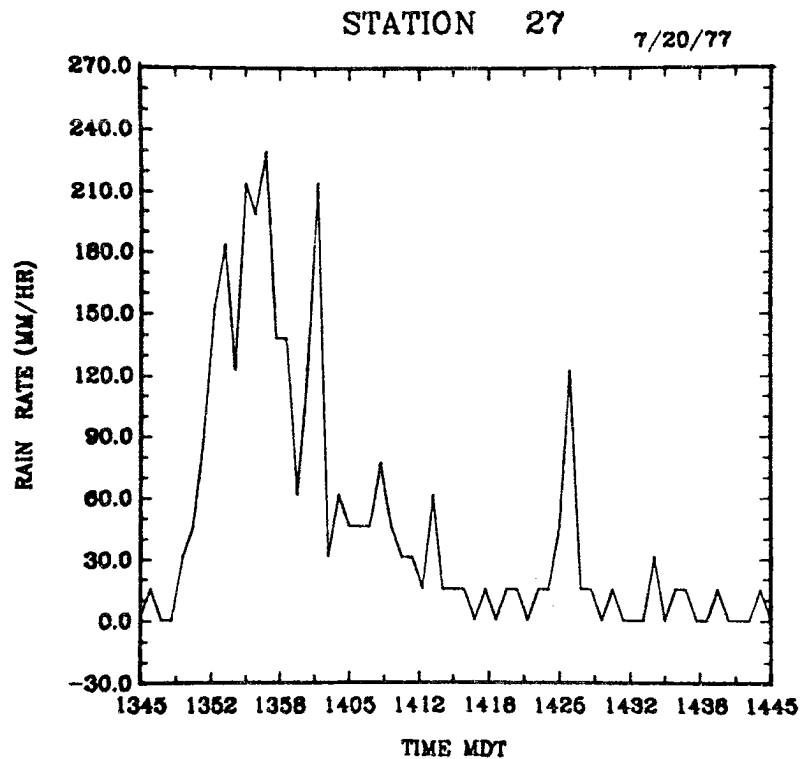


Fig. 4.16. One-minute rainfall rates for selected stations and time intervals. The rates are derived from PAM tipping-bucket raingauges.

appeared to be reinforced by the intense cell behind it. The entire system continued to propagate slowly eastward. Therefore, the outflow leading edge was maintained as a preferred zone for new convective development and thus was important for storm propagation. The IR satellite image for 1945 GMT (Fig. 4.14) indicated that over the previous 30 minutes a cloud top colder than  $-59^{\circ}\text{C}$  developed, and extended northward from the more mature convective complex (A) that existed to the south. The resolution of the IR imagery was too poor to identify individual convective elements.

By 1430 MDT, gust front A continued its southward movement, and intersected the continued northeastward movement of the gust front C. Gust front B at this time could no longer be discerned as a distinct entity (Fig. 4.17). CP-3 radar detected the northern part of gust front C at 0.4 deg. elevation. The striking divergence pattern over southern South Park (Fig. 4.17) within an area of weaker echo was apparently associated with a downdraft organized on the mesoscale, associated with the decay of a number of convective cells. By 1439, one of the cells in northeast South Park produced an isolated one-minute rainfall rate of  $200\text{ mm hr}^{-1}$  at station #14, shown in Fig. 4.16. This corresponded to the small 55 dBZ echo contour visible in Fig. 4.17 just southwest of station #14. Assuming a translational speed of  $5\text{ ms}^{-1}$  and steady conditions, a spacial scale of  $\sim 500\text{ m}$  was implied for the intense portion of this shower. The IR image for 2015 GMT (Fig. 4.14) showed continued rapid development of cold anvils ( $< -53^{\circ}\text{C}$ ) over South Park.

By 1502, the large cell near NOAA-C (Fig. 4.18) produced a well-defined divergent downdraft outflow. Another new outflow center developed near the northern edge of gust front C, which reinforced gust

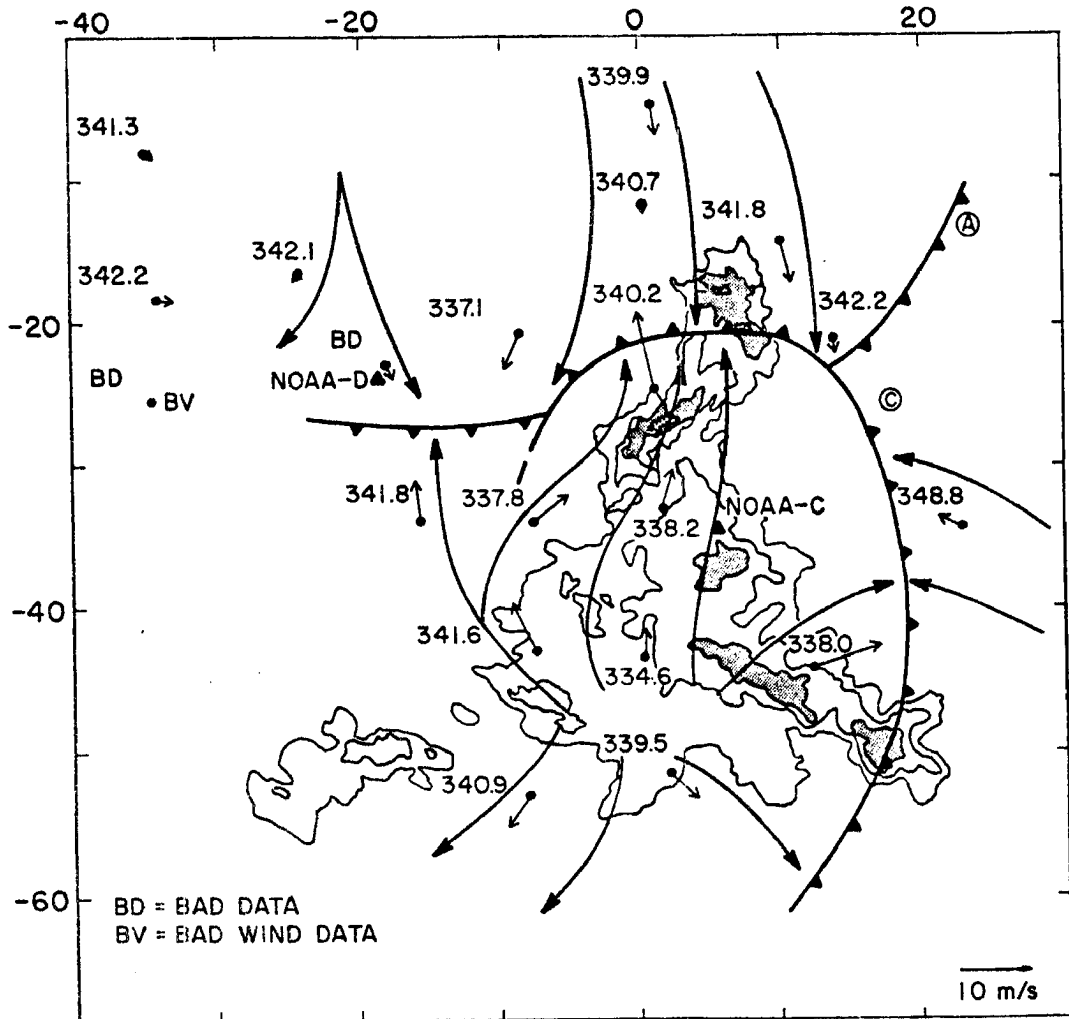


Fig. 4.17. Same as Fig. 4.13, for 1430 MDT.

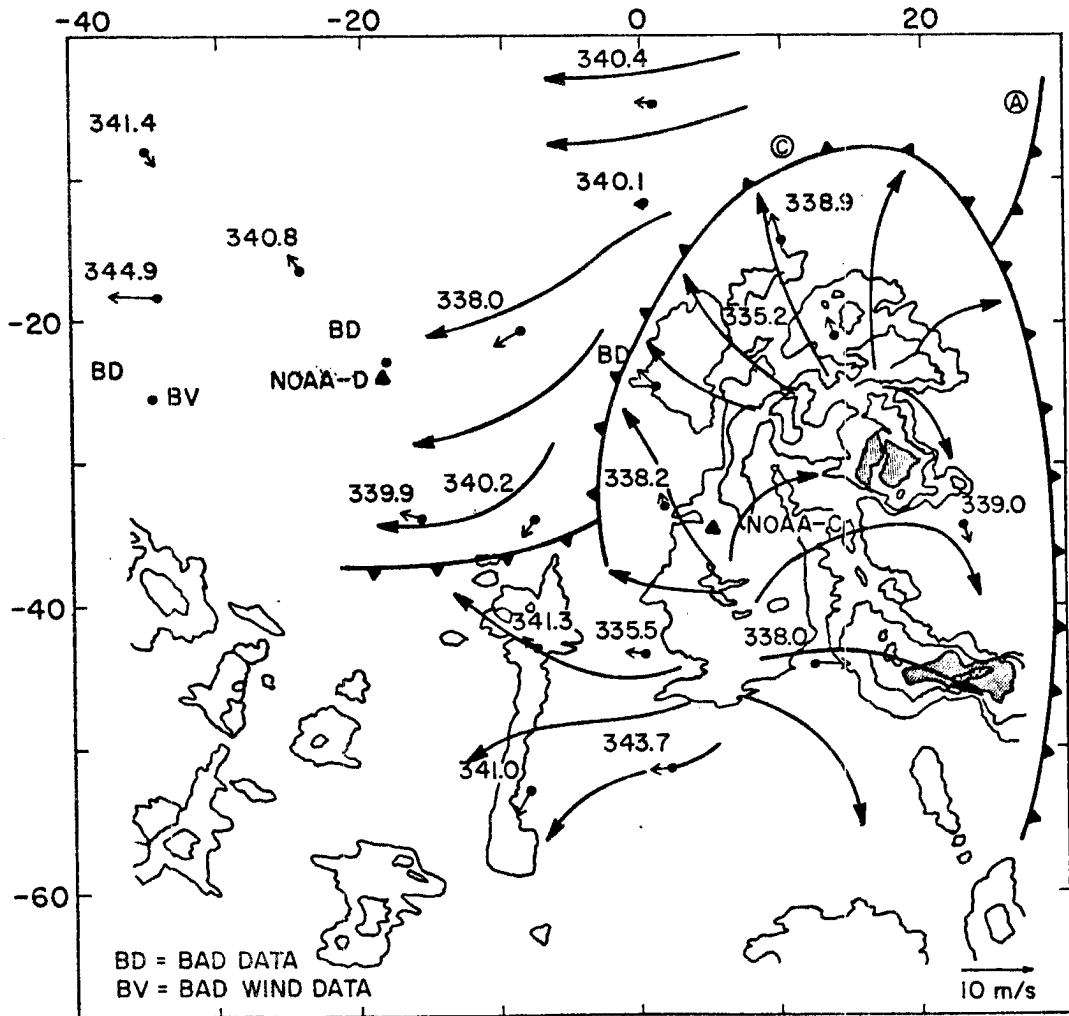


Fig. 4.18. Same as Fig. 4.13, for 1502 MDT.

front C near its northern end. Gust front A continued to move southward, with the reinforced gust front C penetrating it. At this time, reflectivities began to decrease, but infrared satellite data still showed well developed mesoscale anvil extending from the north of South Park to the south (Fig. 4.14). This mesoscale convective system continued to expand as it moved eastward over the foothills and onto the High Plains where it persisted through the night. Several echoes became intense on the Plains, east of South Park, and the linear shape evolved to a more irregular shape.

## 5. STORM-SCALE ANALYSIS AND RESULTS

### 5.1 Evolution of Reflectivity and Flow Fields

Results of various analyses are presented in this section. The observations indicate that the major circulation features were not steady within the limits of the data resolution (~10 min in time and 2-3 Km in space). The following discussion is based primarily on the sampling periods 1327, 1343, and 1349 because data quality was optimal and major merging occurred. Horizontal winds were derived from the NOAA-D and CP-3 dual Doppler combination. They are subject to both random errors and systematic errors. Such errors yield overestimated wind magnitudes. Thus, wind magnitudes are semiquantitative in this thesis. Generally the motion and origin of air parcels is more properly determined from flow patterns relative to the moving storm. However, differential motion may cause smaller features, such as weak circulations, to be obscured or misplaced in the analysis. Likewise, uncertainties abound in estimating storm motion which has no unique definition since different observable features may propagate at differing speeds as the storm evolves. Therefore, the interpretation of circulation centers should be viewed with caution. In the present case, the mean wind vectors derived from each analysis level generally show good agreement with rawinsonde observations.

The echo morphology of the storm during its developmental stages was described in section 4. For the first ~30 min, the storm consisted of a relatively weak multicellular complex. Intensification of echo

within the southern cell group occurred at 1316. This intensification was accompanied by an increasing separation between the more intense echo and the weaker echo. The 1327 time period represents the stage in which the storm transformed from a weak multicellular stage to a more organized unicellular storm. Fig. 5.1 depicts panels of the reflectivity factor and the storm relative horizontal velocity vectors on the selected horizontal cross section at 1327, 1343, and 1349 MDT. At 1327, the storm was characterized by a single dominant reflectivity core ( $C_1$ ) with a major reflectivity core on the southeast flank of the N-S line. A vertical cross section through the reflectivity core of  $C_1$  revealed an overhanging echo structure above a weak echo region, and a sharp reflectivity gradient on the southeast quadrant. A less intense reflectivity core ( $C_2$ ) south of the main reflectivity core was also evident at 1327. At this time, a low level flow with storm relative speed of  $12 \text{ m s}^{-1}$  and thermodynamic properties  $\theta = 319^\circ\text{K}$  and  $q = 10 \text{ g Kg}^{-1}$  continued to approach  $C_1$  from the east. At midlevels ( $Z = 4 \text{ Km}$ ), potentially cool easterly relative flow entered the eastern and southeastern portions of  $C_1$  and apparently maintained the downdraft analyzed in Fig. 5.2. The evidence that mid-level environmental air participated in  $C_1$ 's downdraft circulation is provided by the fact that mesonet station 13 recorded a minimum  $\theta_e$  of 339 at 1328 MDT. This corresponds to a minimum environmental  $\theta_e$  of 338 K which was observed at 45 kPa. Strong upper-level horizontal outflow occurred primarily northwest of  $C_1$ 's reflectivity core.

The quasi-continuous propagation on the SE flank of cell  $C_1$  at 1327 caused  $C_1$  to propagate southeastward and to merge with  $C_2$ , which was weaker and not thoroughly observed at 1327. Presumably, cell  $C_2$  formed

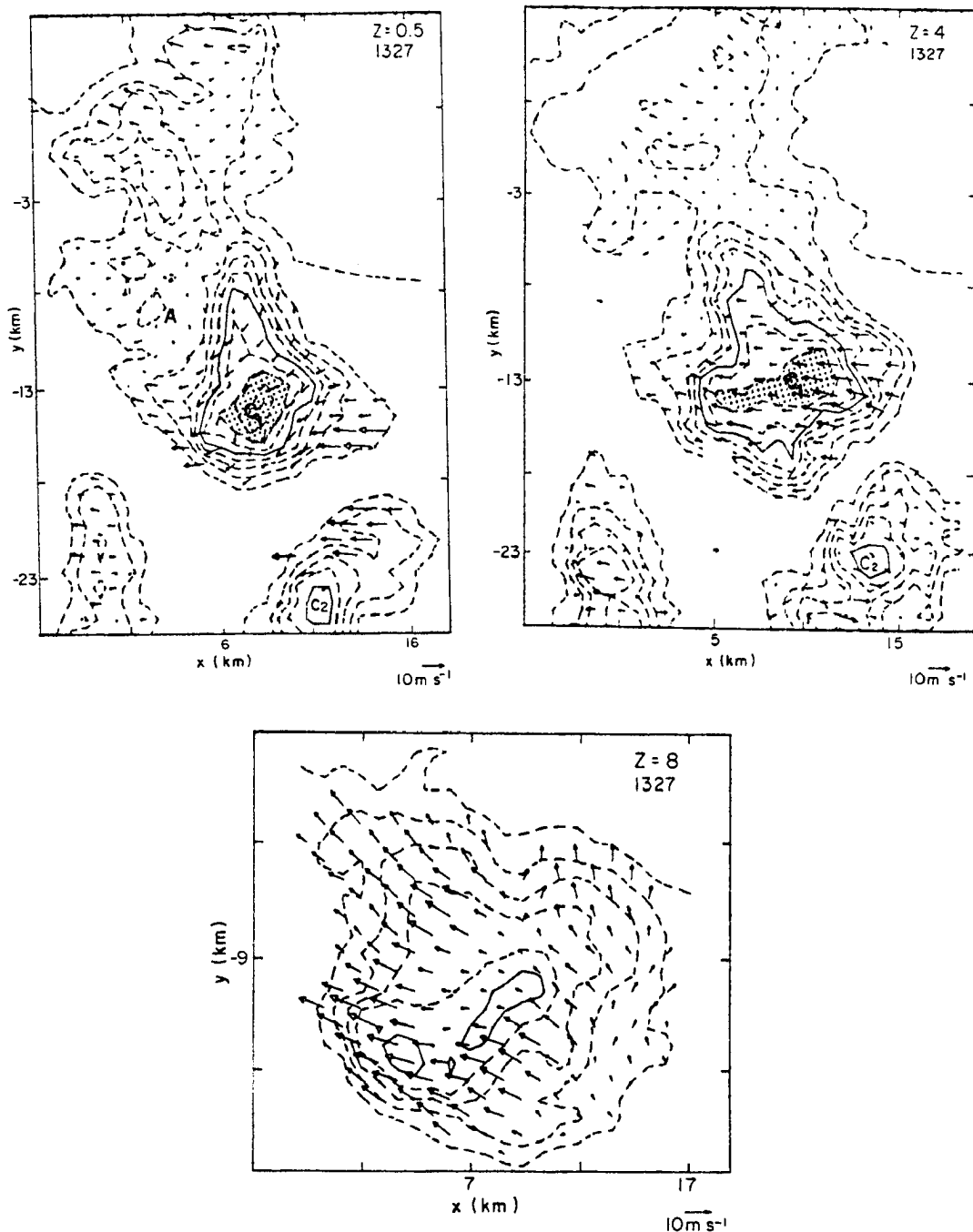


Fig. 5.1. Horizontal cross section of reflectivity and storm relative vectors. Echo contours are given in 5 dBZ intervals beginning at 10 dBZ, with 30 dBZ solid. Echo intensities greater than 40 dBZ are shaded. A  $10 \text{ m s}^{-1}$  vector scale is shown in the lower right-hand corner of each panel.

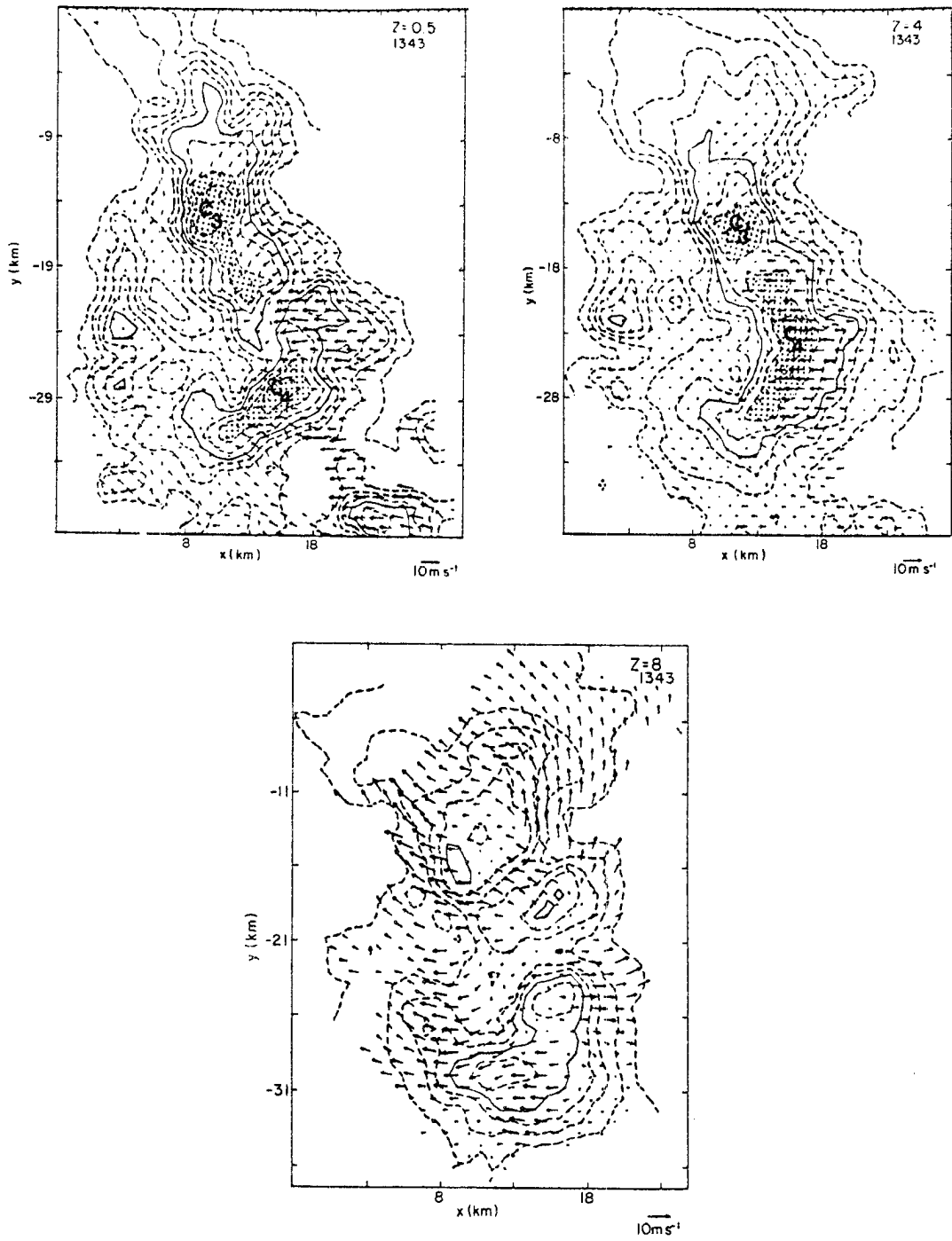


Fig. 5.1. (Continued)

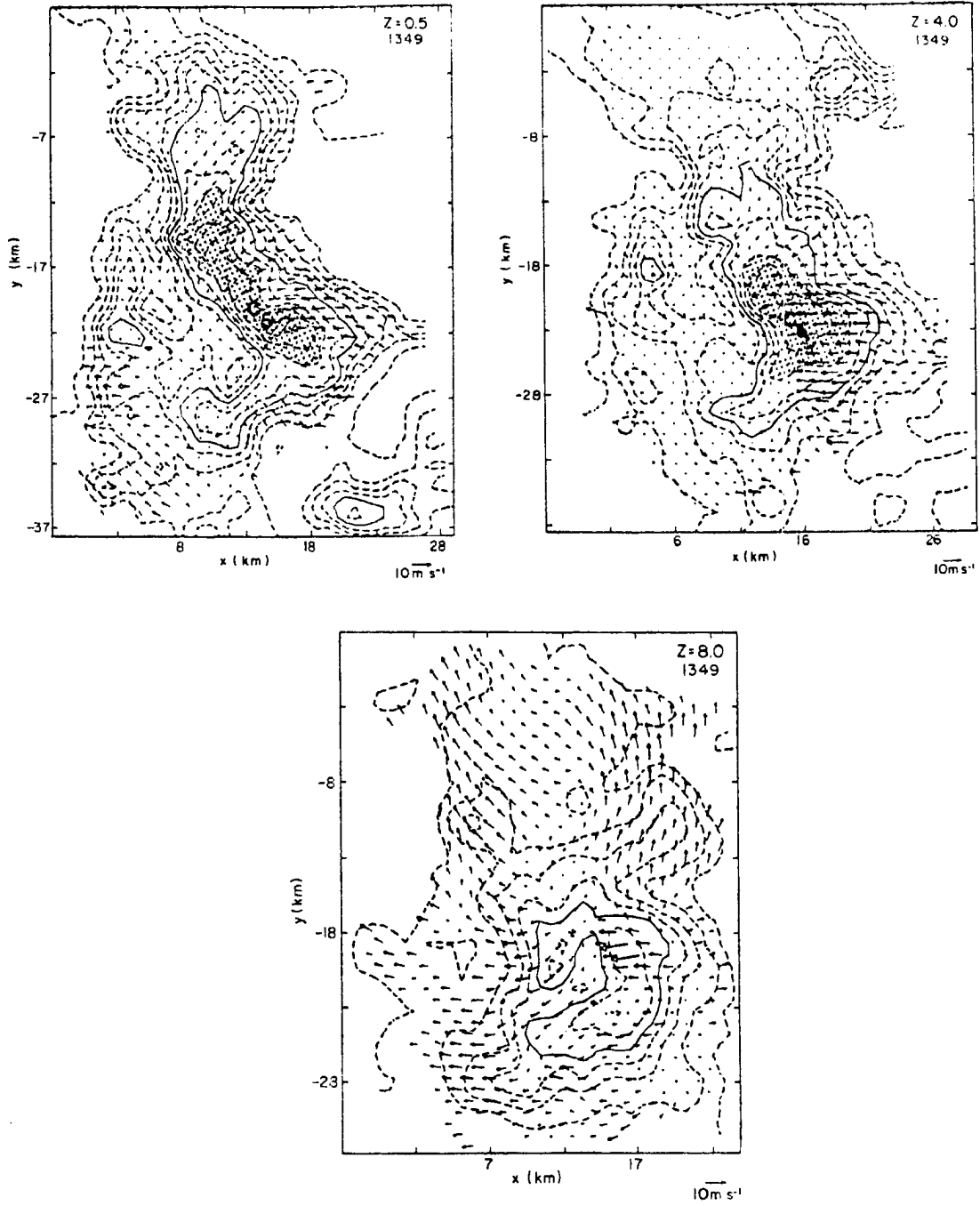


Fig. 5.1. (Continued)

at the gust front intersection. The merged cell, designated as  $C_3$  at 1343, was characterized by a N-S orientation, with signs of separate cells  $C_1$  and  $C_2$  were evident, especially at upper levels ( $Z = 8$  Km). At this time, cell  $C_1$  still had the higher reflectivity and upper level divergent outflow. Cell  $C_4$ , with its own separate gust front, translated to the NNE and out of Doppler coverage. At 1343, this cell was about the same size and intensity as  $C_3$ , and situated to the SSE of the southeastward moving  $C_3$ . The superposition of PAM surface data and 0.5 Km AGL reflectivity and flow patterns indicate that the gust fronts associated with  $C_3$  and  $C_4$  intersected on the leading edge of the combined  $C_3$ - $C_4$  line, near the point of weakest reflectivity between  $C_3$  and  $C_4$ . Subsequent growth occurred near this intersection, as  $C_3$  and  $C_4$  continued their confluent motion and merged by 1349. This rapid growth, resulting in the merger, may have been forced by the intersection of the gust fronts. At 1343,  $C_3$  acquired northeasterly momentum by feeding upon the relatively moist northeasterly flow east of the line.  $C_4$  appeared to be receiving inflow from regions east and southeast of the echo line. The onset and early evolution of  $C_4$  remain somewhat ambiguous because it was out of the range of Doppler radar coverage.  $C_4$ 's initial echo was first apparent at 1328 south of the echo line portrayed in Fig. 4.11. Some of the noteworthy features of this storm (at 1343) were its multicellular nature and discrete propagation, and relatively large storm size and high reflectivity factor. An increase of high-level echo areas and reflectivity at 1343 suggests greater upward mass flux than at 1327, which was mainly due to the merging.

By 1349 the two intense cells ( $C_3$ ,  $C_4$ ) merged into a single cell ( $C_5$ ), which was the strongest cell over South Park. The cyclonic inflow/anticyclonic outflow couplet can be partly responsible for the N-S echo orientation shifting more NNW-SSE by this time. At lower levels, easterly inflow east of  $C_5$ 's updraft region continued to exhibit relatively strong magnitudes. The reflectivity structure changed dramatically in 6 min in upper levels, from a definite 2-cell ( $C_3$  and  $C_4$ ) upper level reflectivity structure to a single cellular structure, with an increased high-level reflectivity factor. The merged cell  $C_5$  resulted in highest rainfall rates at PAM station #27 shortly after 1349 (see Fig. 4.6).

## 5.2 Structure of the Updrafts, Downdrafts and Divergence

Patterns of analyzed vertical motion within  $C_1$  at 1327 MDT, displayed in Fig. 5.2, exhibit a more variable pattern than indicated by reflectivity structure alone. It should be mentioned that the accuracy of the derived vertical winds is regarded as semiquantitative. The primary updraft ( $U_1$ ) associated with cell  $C_1$  was located in the southwestward quadrant of the storm. The low level relative inflow was easterly and fed the main updraft of cell  $C_1$  with a core diameter of  $\sim 2$  Km and a maximum about  $18 \text{ m s}^{-1}$  at 6 Km AGL. The updraft peak is due to the positive acceleration of the updraft air due to positive buoyancy and latent heat release, or perhaps due to decreased water load after precipitation particles have fallen out of the updraft. Newton (1963) showed that the buoyant acceleration of convective elements is significantly diminished both by entrainment of inert air and by form or aerodynamic drag. To obtain an estimate of the magnitude of updraft the environment was capable of producing, a one-dimensional cloud model

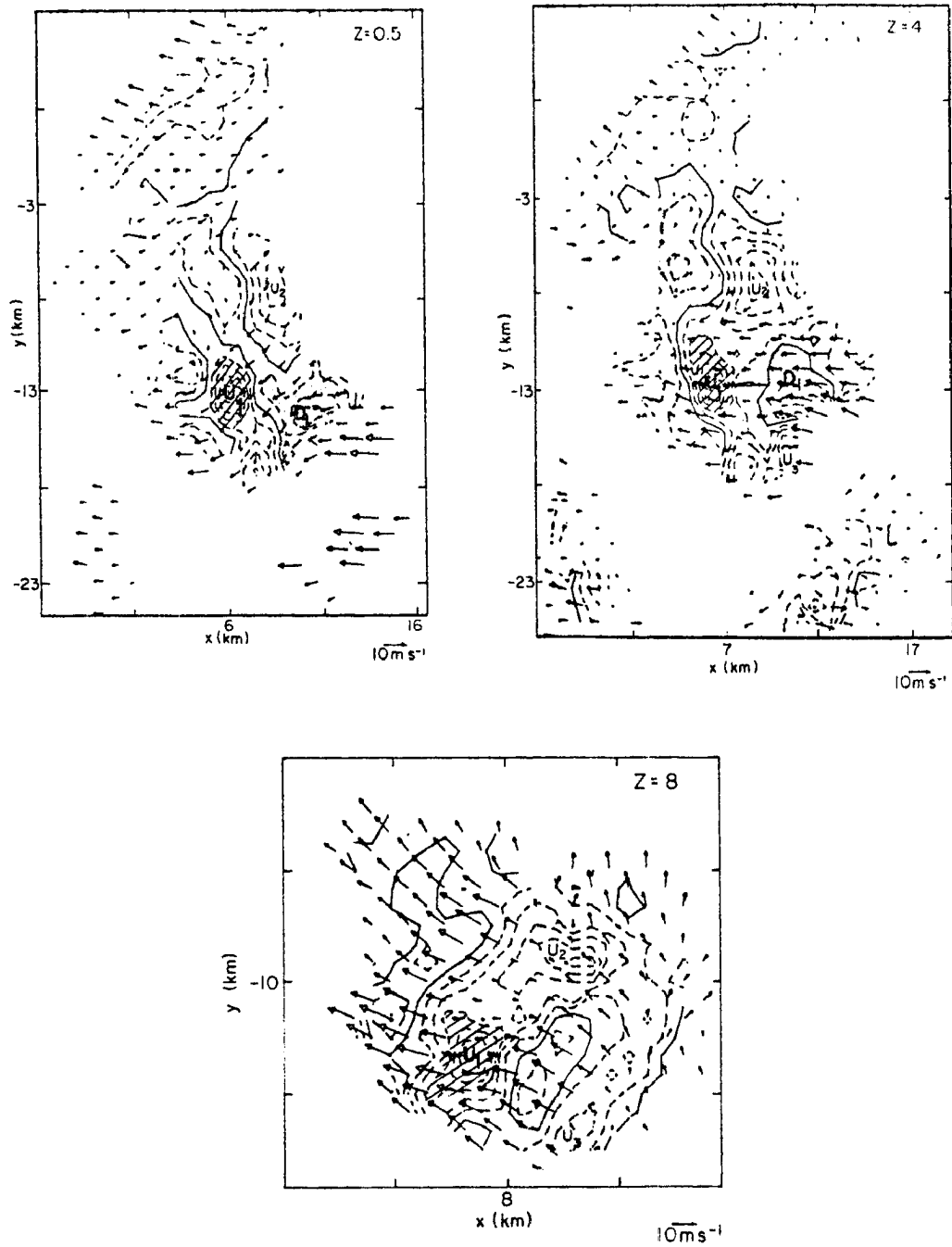


Fig. 5.2. Analyzed vertical motion for 1327 time period. Vertical velocity is in  $4 \text{ ms}^{-1}$  intervals. The main updraft ( $U_1$ ) is cross hatched; and downdrafts are stippled.

(Cotton, 1970) was run using the South Park sounding at 1003 MDT. The updraft size and precipitation scheme was varied in the model. This resulted in a maximum updraft of  $\sim 20 \text{ m s}^{-1}$ , at a height of  $\sim 6 \text{ Km}$ . This maximum vertical velocity is consistent with the observations of cell  $C_1$  in Fig. 5.2. Vertical velocities are  $\sim 4 \text{ m s}^{-1}$  larger at 0.5 Km in the observations, perhaps due to accumulation of errors in the vertical velocity integration. The main updraft ( $U_1$ ) was in the region of high reflectivity, but was strong enough to overcome the water-loading effects. Browning and Ludlum (1962) explain the weak echo region as a region of high-speed updraft, where cloud particles do not have sufficient time to grow to appreciable sizes for detection by radar. Presumably, the absence of such a weak echo region in the present case can be due to the relatively weak updraft compared to typical severe storms with updrafts  $> 25 \text{ m s}^{-1}$ . An east-to-west vertical cross section through the core of updraft  $U_1$  (Fig. 5.3,  $Y = -13$ ) indicated that this updraft tilted westward from lower levels to upper levels. The flow pattern at upper levels (Fig. 5.2) exhibited a diverging behavior, with a maximum analyzed divergence of  $16 \times 10^{-3} \text{ s}^{-1}$  at 10 Km AGL. The strongest upper level horizontal outflow occurred primarily northwest of  $C_1$ 's core, and attained peak analyzed magnitude of  $\sim 22 \text{ m s}^{-1}$ . This divergence is probably due to the updraft penetrating a stable layer found in environmental sounding. Less intense updraft ( $U_2$ ) on the northeast flank of the storm was also evident in Fig. 5.2 at 1327. The air feeding  $U_2$  originated from the northeast, and the maximum analyzed vertical motions within  $U_2$  were  $10 - 14 \text{ m s}^{-1}$ . A east-to-west vertical cross section through the core of updraft  $U_2$  (Fig. 5.3,  $Y = -8.5$ ) indicated westward tilt at upper levels. This vertical cross section

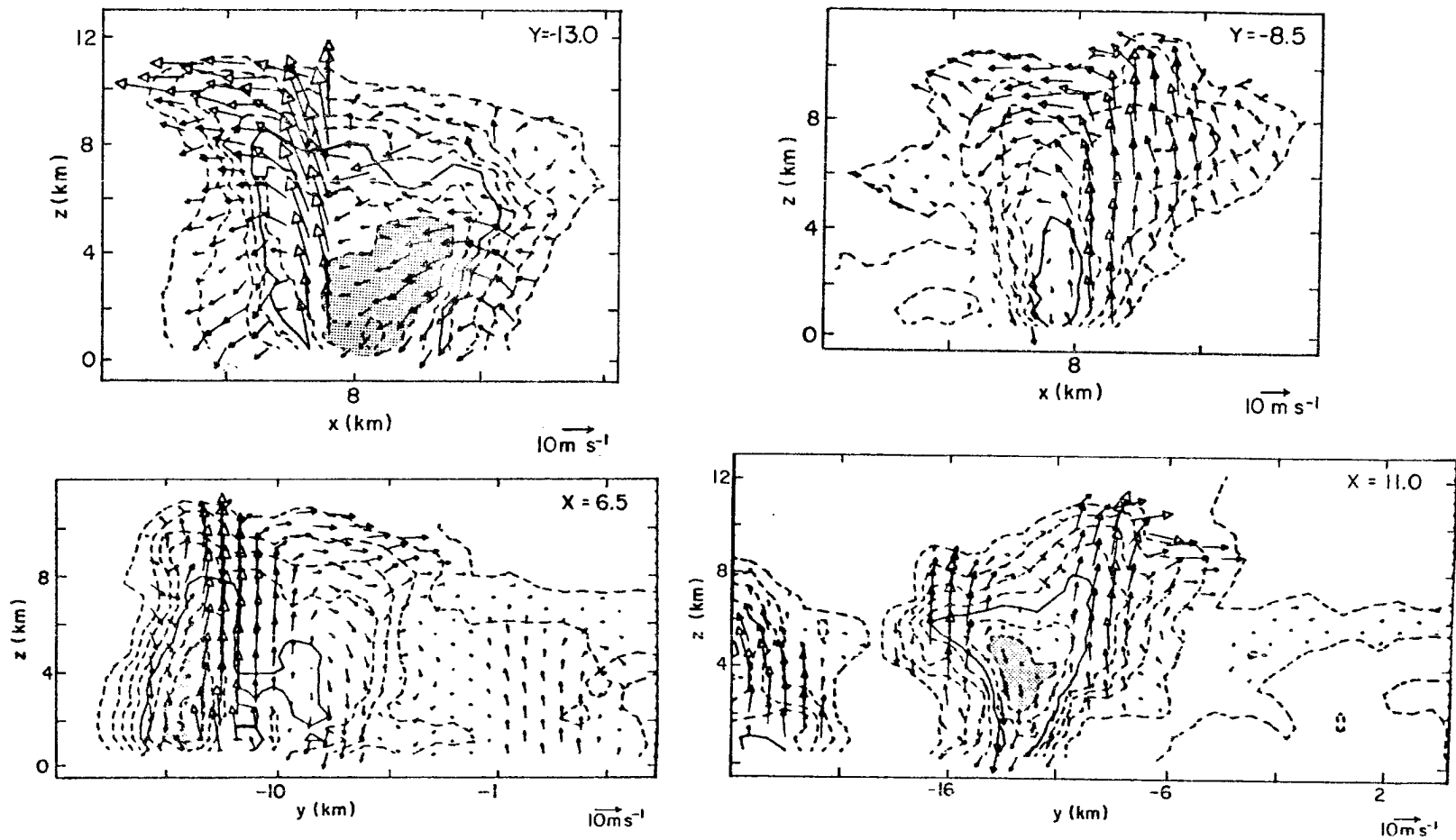


Fig. 5.3. Dual Doppler-derived velocity vectors (storm relative) in east-west and north-south vertical planes at 1327 MDT. Echo contours and vector scales as in Fig. 5.1.

also showed that wind patterns at upper levels exhibited slightly lower outflow and divergence magnitude, thus verifying the analyzed lower updraft magnitude for  $U_2$ . These two updrafts ( $U_1$  and  $U_2$ ) exhibited a storm splitting characteristic. But in this case, the storm did not split, probably because of very weak environmental wind shear. Klemp and Wilhelmson (1978) showed that the tendency of an initial storm to split into two self-sustaining storms is strongly dependent on the intensity and distribution of the low-level shear. In their study it was also found that splitting can occur when low-level convergence produced by interaction between the downdraft-induced gust front and the low-level environmental wind moves with the storm, rather than out ahead of it (similar to July 20 case). The extreme southern  $5-10 \text{ m s}^{-1}$  updraft ( $U_3$ ) was apparently associated with quasi-discrete cell growth along  $C_1$ 's southeastern borders.

Analyzed downdrafts are displayed in Fig. 5.2, and exhibited cellular patterns. The main downdraft ( $D_1$ ) originated at  $\sim 4 \text{ Km}$ , and was located on the leading edge (eastern) of the storm. This downdraft was associated with high reflectivity, and maximum analyzed downdraft magnitude was about  $13 \text{ m s}^{-1}$  at 1-2 Km AGL. The preferred southeastward propagation of the storm at this time might be due to the inhibiting effects of the right flank downdraft on the low level inflow. Thus, instead of a solid eastward propagation line, this downdraft helped to force low level convergence on the southeast flank, also helped to maintain a weaker updraft ( $U_2$ ) on the northeast flank. As mentioned earlier, at midlevels ( $Z = 4 \text{ Km}$ ), potentially cool, easterly and southeasterly, relative flow entered the southeastern portion of the storm and apparently maintained the downdraft  $D_1$  on this flank. The

downward transport of SE flow explained why air behind the gust front had a strong northwesterly component of motion. The vertical east-to-west cross section (Fig. 5.3,  $Y = -13$ ) through the core of this downdraft revealed vertical continuity and an origin at midlevels east of the primary updraft ( $U_1$ ). A north-to-south vertical cross section ( $X = 11.0$ ) showed an overhanging echo structure and sharp reflectivity gradient on the southeast storm quadrant. The right flank downdraft was associated with high reflectivity, and thus, precipitation loading was important in its sustenance. However, negative buoyancy due to evaporational cooling also appeared to be an important mechanism for sustaining this downdraft.

The mid-level inflow did not appear to well represent the storm-relative environmental flow (according to 10 MDT sounding). The 4 km southeasterly inflow into the right flank downdraft (Fig. 5.2,  $Z = 4$ ) can be a diverted flow. The diversion of the ambient flow at midlevels around cell  $C_1$  can be hypothesized as follows. The southeastward propagation of  $C_1$  allowed the western updraft regions to be exposed to the midlevel ambient environmental airflow. Since low-level momentum within updrafts tends to be conserved (as suggested by Knupp and Cotton 1982, and Browning and Foote, 1976) interaction of the updraft air with environmental air produced inferred pressure perturbations which diverted and accelerated the midlevel flow around the western region of  $C_1$ 's updraft. Other possibilities could be that the quasi-discrete cell growth to the southeast modified midlevel flow, or slight evaporational cooling in the relatively inactive western and northwestern portions of  $C_1$  may have created a pressure excess which diverted the flow at greater distances from the storm (Knupp and Cotton 1982).

Analyzed divergence patterns for the 1327 time period are shown in Fig. 5.4. Horizontal flow at 0.5 km AGL produced a convergence zone oriented in the southeastern portion of  $C_1$ 's reflectivity core. This boundary evidently marked the leading edge of  $C_1$ 's gust front. The convergent region at 4 km was coincident with the downdraft originating at that level, and was indicative of the deceleration of the flow in the horizontal plane as the mid-level strong easterly inflow was incorporated into the downdraft. A relatively strong divergence at upper level ( $Z = 8$  km) was associated with upper level horizontal outflow occurred at that level.

By 1343, the development of an elongated N-S reflectivity axis resulted in a corresponding N-S downdraft (Fig. 5.5). Thus, the cellular downdraft at 1327, which helped to maintain updrafts  $U_1$  and  $U_2$  (with updraft  $U_1$  being stronger and preferentially propagating cell  $C_1$  to the southeast), became more N-S, with the forcing also assuming more of a N-S orientation on the leading edge of the cluster. This eastward forcing subsequently resulted in a eastward acceleration of the storm system. Thus, the southeastward and northeastward propagation that was earlier observed was no longer possible with the merged N-S reflectivity line.

Analyzed downdrafts displayed in Fig. 5.5 are consistent with other studies of mature thunderstorms (Knupp and Cotton 1982, Kropfli and Miller, 1976). Downdraft  $D_3$  associated with cell  $C_3$ , exhibited the greatest vertical depth. Downdraft  $D_3$ , attained maximum analyzed speeds of  $10 - 12 \text{ ms}^{-1}$  at about 3 km AGL. The vertical east-to-west (Fig. 5.6,  $Y = -15$ ) and north-to-south (Fig. 5.6,  $X = 13$ ) cross section through the core of this downdraft revealed vertical continuity and originated at

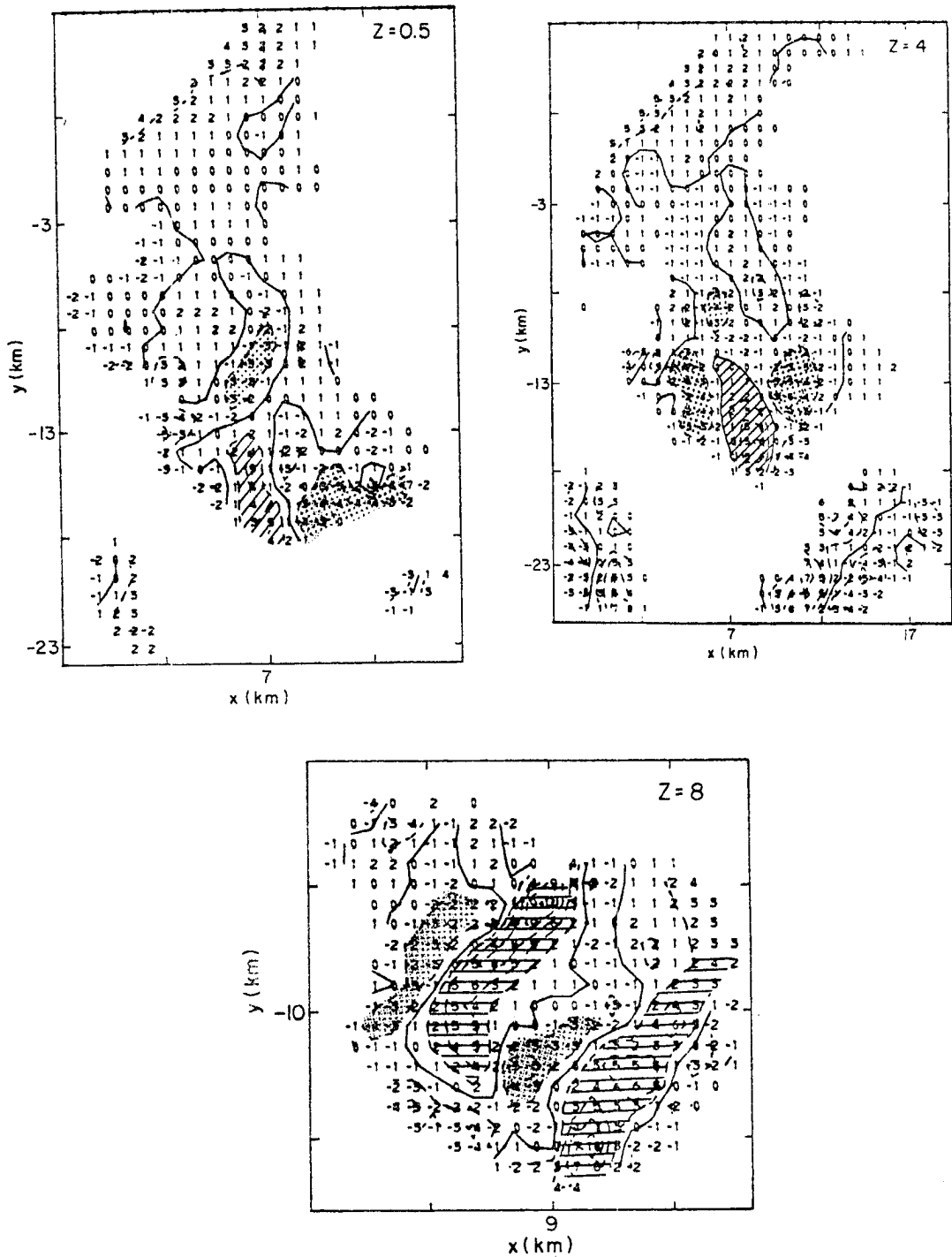


Fig. 5.4. Analyzed divergence patterns for 1327 time period. Contours are in  $2.0 \times 10^{-3}$  intervals. Divergence  $> 2 \times 10^{-3}$  are cross hatched; and  $< -2.0 \times 10^{-3}$  are stippled.

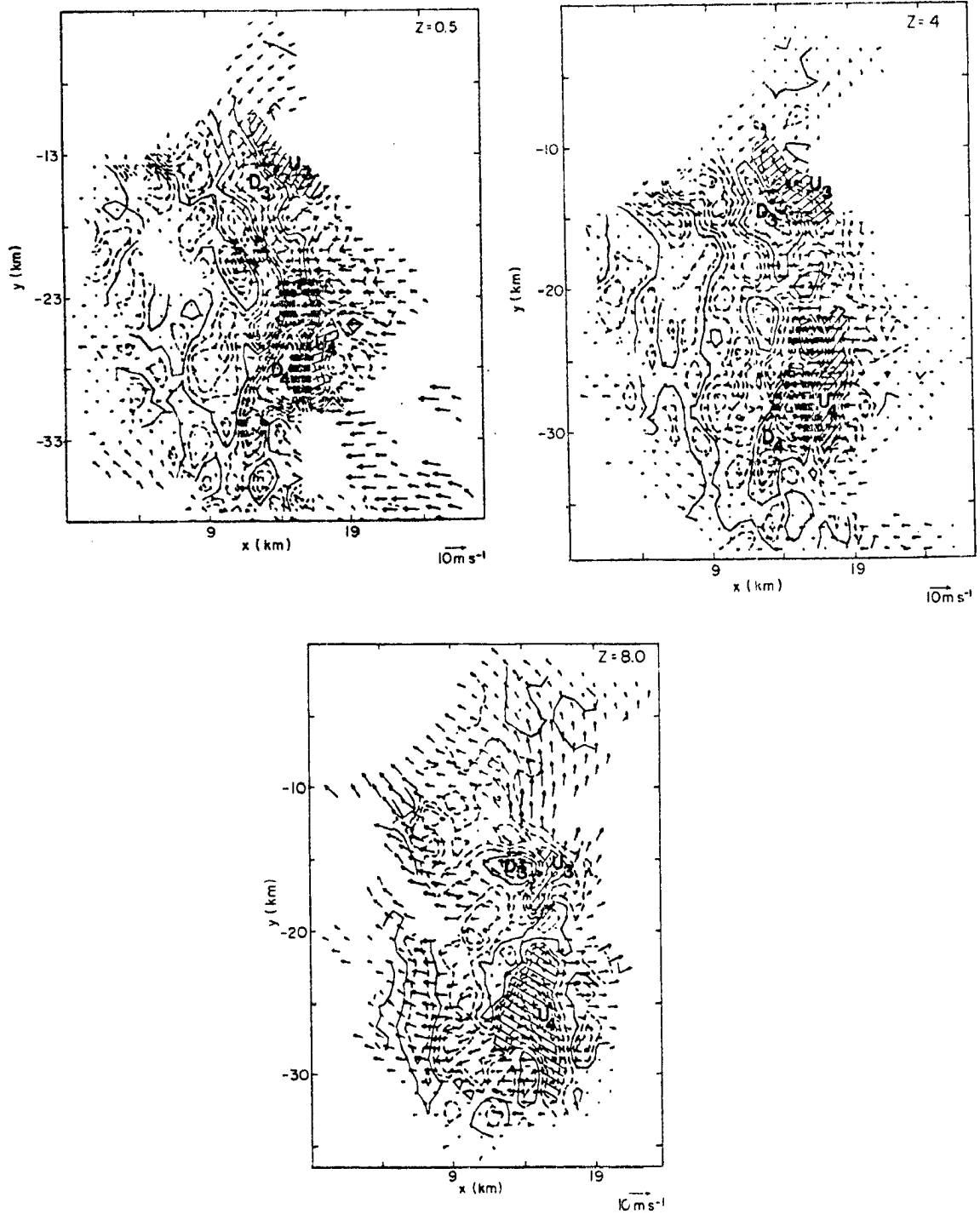


Fig. 5.5. Analyzed vertical motion for 1343 time period. Vertical velocity is in  $4 \text{ m s}^{-1}$  intervals. Updrafts  $U_3$  and  $U_4$  are cross hatched; and downdrafts  $D_3$  and  $D_4$  are stippled.

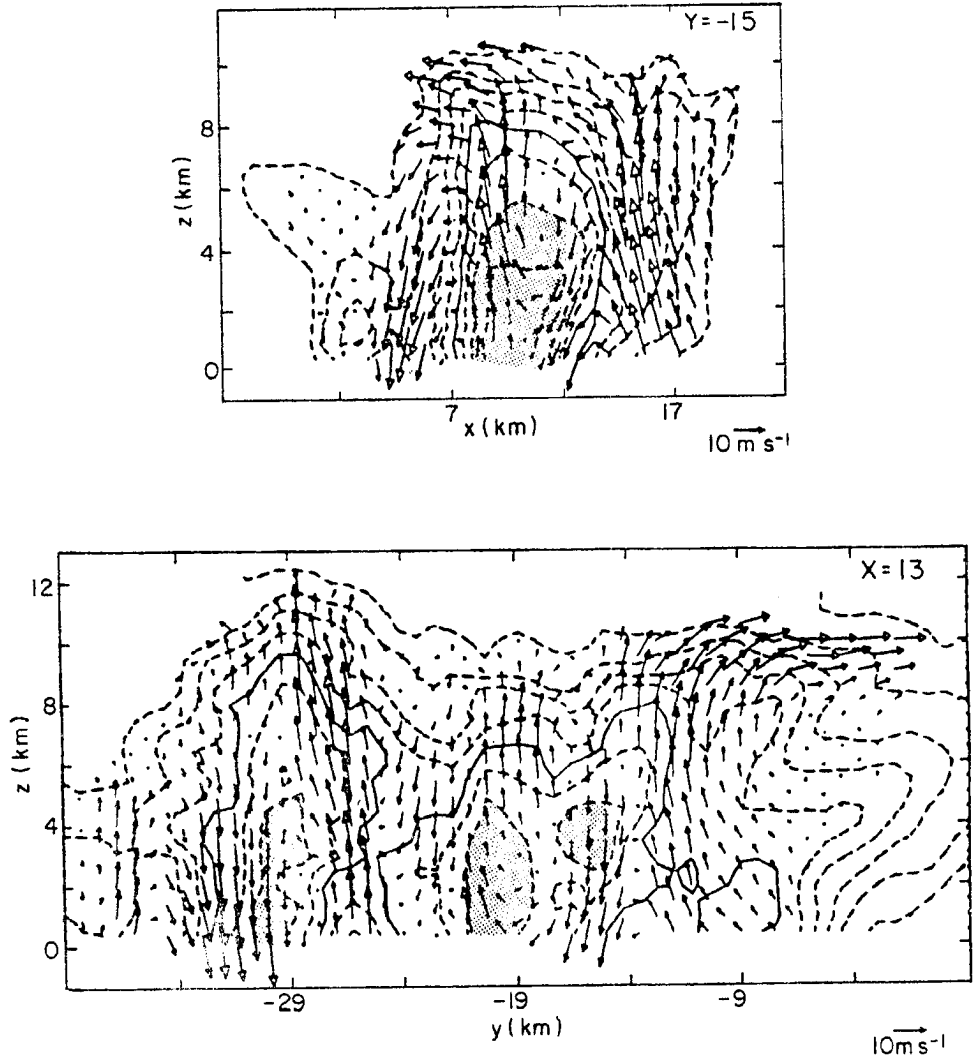


Fig. 5.6. Dual Doppler-derived velocity vectors (storm relative) in east-west and north-south planes at 1343 MDT. Echo contours and vector scales as in Fig. 5.1.

midlevels west of the updraft  $U_3$ . Downdraft  $D_4$  associated with  $C_4$  attained maximum analyzed speed of  $16 - 20 \text{ ms}^{-1}$  at 3 km AGL. The vertical cross section (E-W, N-S) through the core of downdrafts  $D_4$  are shown in Fig. 5.7. The location of the downdrafts  $D_3$  and  $D_4$  resemble rear flank downdrafts commonly observed within severe hailstorms and tornadic storms (Barnes, 1982; Lemon and Doswell, 1979). This downdraft was suggested to be important in mesocyclone intensification.

Downdrafts  $D_3$  and  $D_4$  were confined almost beneath the level of maximum updraft velocity (Fig. 5.6,  $X = 13$ ). The most intense portion of these downdrafts reached the ground to the south and west underneath the updrafts ( $U_3$  and  $U_4$ ). The resulting gust fronts forming along the right flank of the storm produced strong low-level convergence which forced up-lifting of the moist inflow from the east to sustain the updrafts  $U_3$  and  $U_4$  (Fig. 5.5). Mesonet PAM stations did indicate well-defined gust fronts as cells  $C_3$  and  $C_4$  passed nearby. This gust front induced convergence which appeared to govern the storm's propagation toward the east as discussed by Moncrieff and Miller (1976), based on the simulation of a tropical storm. Subsequently, the strongest development occurred with the merger of  $C_3$  and  $C_4$  as a consequence of the approach or collision of the downdrafts  $D_3$  and  $D_4$ . Downdrafts  $D_3$  and  $D_4$  have been maintained by precipitation loading, since they are associated with high reflectivity (see Figs. 5.6 and 5.7). However, these downdrafts also appear to have been partially maintained by evaporation from relative easterly and southeasterly inflow of potentially cold (low-level  $\theta_e$ ) midlevel air. This airflow entered the downdrafts  $D_3$  and  $D_4$  either by a direct trajectory into the eastern storm flank, or by inflow into the downstream 'wake' of updrafts  $U_3$  and  $U_4$  (Fig. 5.5). The

updraft downdraft relative flow patterns observed here resemble the process of entrainment described in the conceptual model of Heymsfield et al. (1978) and in the numerical model experiments of Tripoli and Cotton (1980) for individual towering cumuli. However, this phenomenon occurred to a lesser extent in the July 20 case study probably because of relatively weak environmental wind shear and speed.

Low-level flow at 1343 was similar to that observed at 1327.

Easterly and southeasterly surface winds continued to feed updrafts  $U_3$  and  $U_4$ . Maximum updraft analyzed for cell  $C_3$  exhibited a peak speed of  $\sim 25 \text{ ms}^{-1}$  at mid to upper level. Updraft  $U_4$ , associated with cell  $C_4$ , exhibited slightly higher peak vertical velocities of  $\sim 29 \text{ ms}^{-1}$  at 4-6 km AGL. The velocity differences are probably due to north-south gradients in the low-level momentum. The easterly component of low-level momentum east of the updraft  $U_4$  was greater than that on the east side of the updraft  $U_3$  (see Fig. 5.5). The presence of this higher maximum seems to be substantiated by the higher reflectivity maximum visible on the  $Z = 8$  plane in Fig. 5.1. An east-to-west vertical cross section through the core of updraft  $U_3$  (Fig. 5.6,  $Y = -15$ ) revealed a slight westward tilt at low to upper levels. Updraft  $U_4$  also tilted westward (Fig. 5.7,  $Y = -27.7$ ). These vertical cross sections indicated that wind patterns at upper levels exhibited slightly lower outflow and divergence magnitudes for updraft  $U_3$  than that for updraft  $U_4$ , thus supporting the analyzed lower updraft magnitude for  $U_3$ . Patterns of analyzed vertical motion at 1343 revealed additional updrafts and downdrafts which were somewhat less prominent. It is possible that these updrafts and downdrafts were associated with subsidiary cells within the multicellular storm at this time.

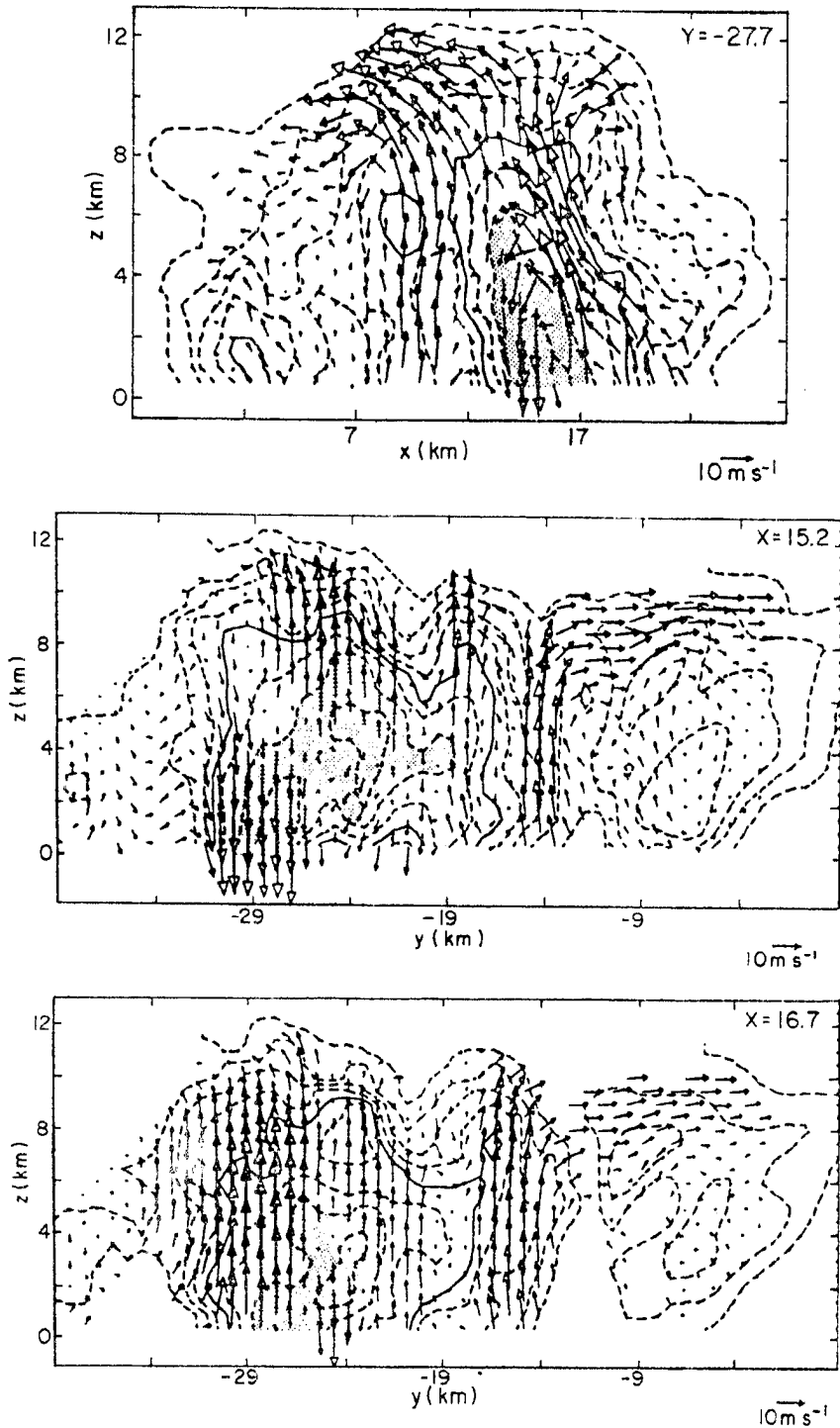


Fig. 5.7. Dual Doppler-derived velocity vectors (storm relative) in east-west and north-south planes at 1343 MDT. Echo contours and vector scales as in Fig. 5.1.

Fig. 5.5 shows that the horizontal inflow on the eastern side of the complex was characterized by weak easterlies at the periphery of the wind data, then accelerated to strong easterlies ( $\sim 10 \text{ ms}^{-1}$ ) through the region of strong updrafts on the leading edge of the storm system, and then sharply decelerated as the flow encountered the reflectivity and downdraft axes. This acceleration can be due to the strong surface inflow (i.e., PAM data  $\sim 10 \text{ ms}^{-1}$ ) being lifted through the low and mid-levels in the eastern updraft region of the system while maintaining its easterly momentum; or non-hydrostatic pressure deficits in the region of the intense vertical acceleration in the updrafts (due to positive buoyancy and latent heat release) created an inward lateral pressure gradient force at low and mid-levels. The deceleration is due to the strong blocking of the downdraft cores. A similar pattern was also observed for the volume scan at 1349 (see Fig. 5.9). Tripoli and Cotton (1980) discussed the relative importance of pressure gradient forces and momentum transport in the horizontal acceleration of winds. The role of the buoyancy-driven updrafts and downdrafts in transporting horizontal momentum in cumulus circulations has been discussed extensively in the literature (e.g., Takeda, 1971; Miller, 1978, etc.). Moncrieff and Miller (1976), however, had shown an upgradient transport of momentum to occur within the deep cumulonimbus squall line in the tropics. This horizontal acceleration of momentum in excess of the amount vertically transported can be attributed to accelerations due to horizontal gradients of pressure on the cloud-scale. The simulations performed by Tripoli and Cotton (1980) showed that horizontal pressure gradient forces were at least as important in accelerating winds as vertical transports of momentum.

Analyzed divergence patterns for the 1343 time period are shown in Fig. 5.8. Maximum divergence magnitudes doubled since 1327 MDT. The N-S convergence axis, with maximum magnitudes of  $-12 \times 10^{-3} \text{ s}^{-1}$ , in general was located east of the reflectivity and maximum downdraft axis. Several E-W cross sections (Fig. 5.6 and 5.7) suggest that the precipitation dominated downdraft along the reflectivity axis acted as a block to the easterly inflow ( $\sim 10 \text{ ms}^{-1}$ ), which caused these strong convergent regions and possibly helped to divert the horizontal flow into the vertical updrafts. Convergence was strongest from low to mid-levels (much stronger than in previous volume scans) in the region between cells  $C_3$  and  $C_4$ , thus verifying their confluent motion. Subsequent growth occurred near this intersection. Divergence at mid-level, on the leading edge of the storm system, was co-located with the region of strong easterlies. Maximum divergence of  $14 \times 10^{-3} \text{ s}^{-1}$  at upper levels ( $Z = 10 \text{ km}$ ) responded to the development of the updraft and vertical expansion of the storm since 1327 MDT when strong outflow and divergence occurred at 8 km AGL.

At 1349, the updraft and downdraft structure was not as linear as the previous time, the most intense updraft/downdraft couplet was associated with the strongest cell at the merger of cell  $C_3$  and  $C_4$  (Fig. 5.1). Southeasterly surface inflow continued to feed updraft  $U_5$  (Fig. 5.9). Maximum analyzed updraft magnitudes for 1349 were  $36 \text{ ms}^{-1}$  at 6-7 km AGL, stronger by  $6 \text{ ms}^{-1}$  than at 1343. The peak updraft magnitude was due to the positive buoyancy and latent heat release. The vertical east-to-west ( $Y = -19.2$ ) and north-to-south ( $X = 18.2$ ) cross sections through the core of this updraft (Fig. 5.10) revealed vertical continuity, with slight westward tilt at low to upper levels (see  $Y =$

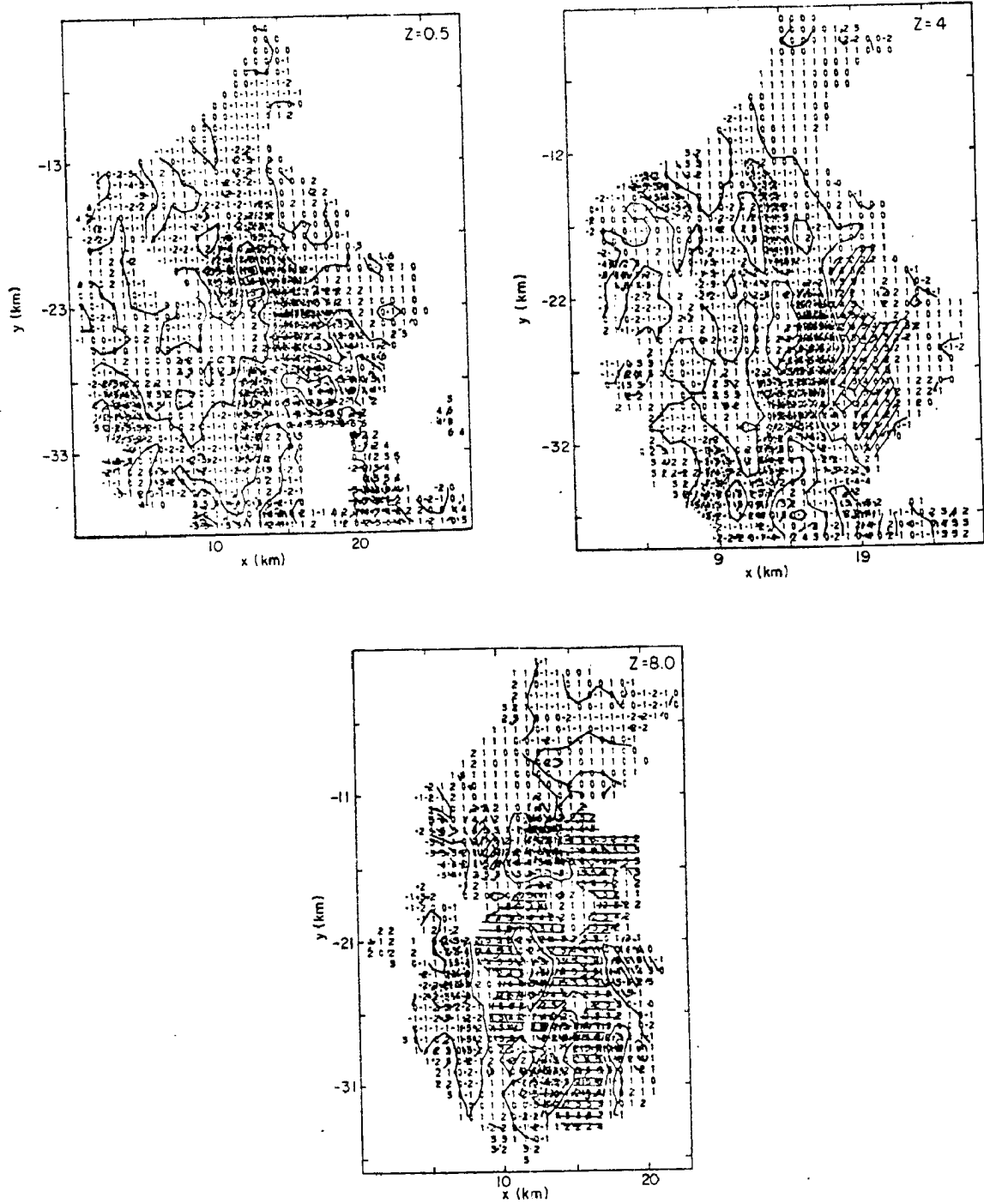


Fig. 5.8. Analyzed divergence patterns for 1343 time period. Contours are in  $2.0 \times 10^{-3}$  intervals. Divergence  $> 2.0 \times 10^{-3}$  are cross hatched; and  $< -2.0 \times 10^{-3}$  are stippled.

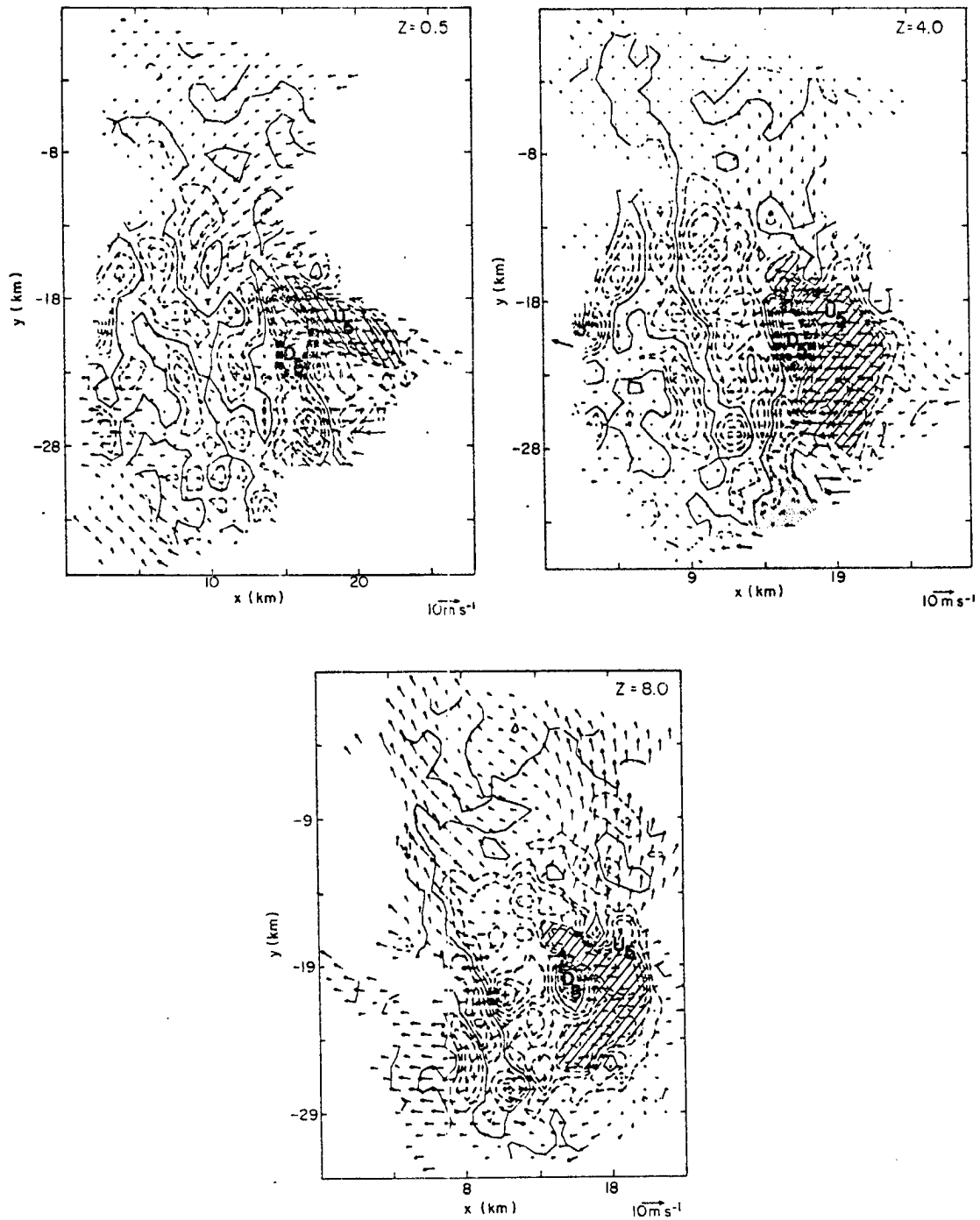


Fig. 5.9. Analyzed vertical motion for 1349 time period. Vertical velocity is in  $4 \text{ m s}^{-1}$  intervals. Updraft  $U_5$  is cross hatched; and downdraft  $D_5$  is stippled.

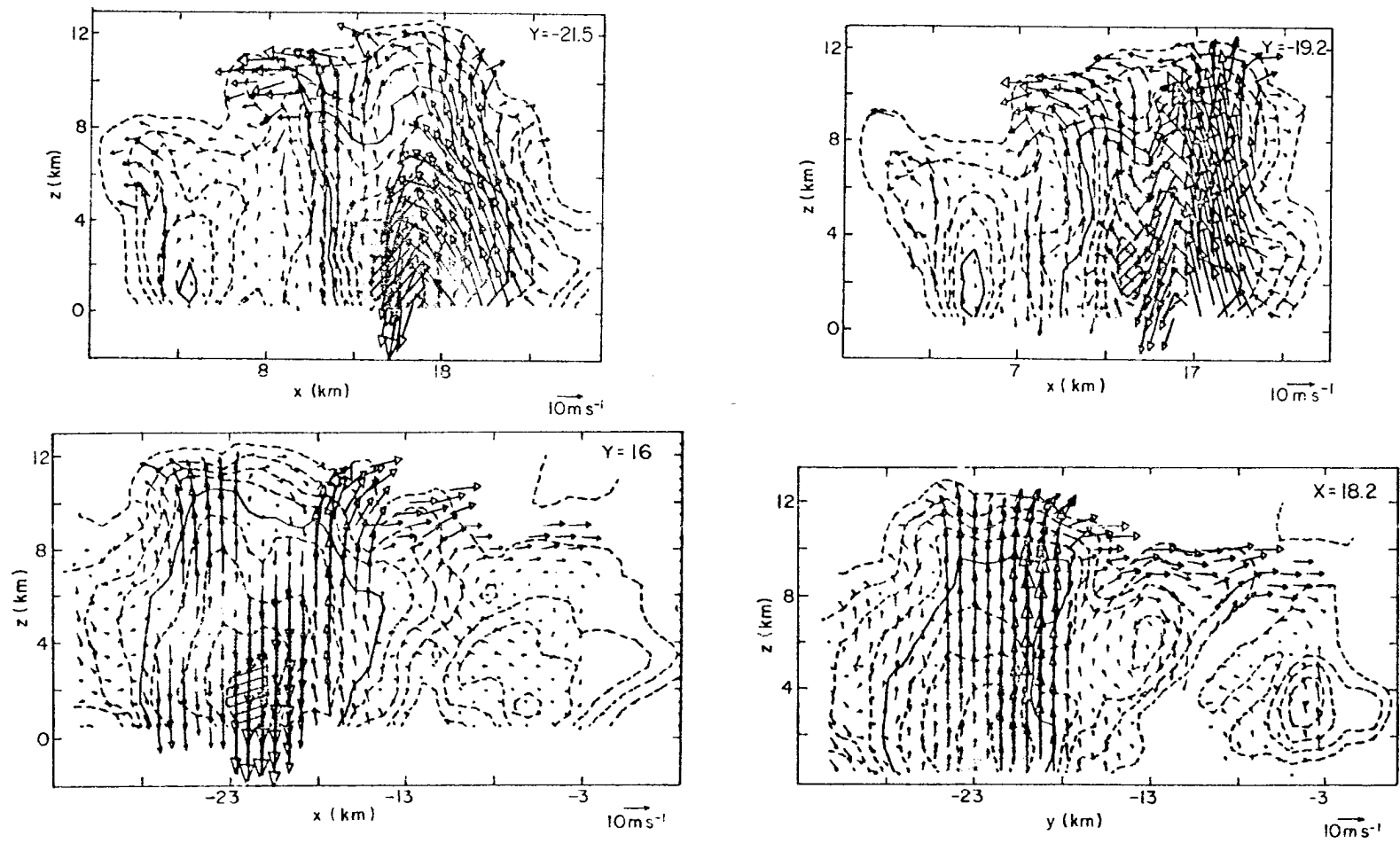


Fig. 5.10. Dual Doppler-derived velocity vectors (storm relative) in east-west and north-south planes at 1343 MDT. Echo contours and vector scales as in Fig. 5.1.

-19.2 plane). A similar configuration was present at earlier times. Mean flow patterns at upper levels ( $Z = 10$ ) exhibited a diverging behavior, with a maximum analyzed divergence of  $13 \times 10^{-3}$  at 10 km AGL. Strongest upper level horizontal outflow occurred primarily west and north of cell  $C_5$ 's core. Downdraft  $D_5$  associated with cell  $C_5$  exhibited the greatest vertical depth since 1343, due to higher water-loading at upper levels (35 dBZ echo intensify at 8 km AGL, see Fig. 5.1). Downdraft  $D_5$  attained a maximum analyzed speed of  $36 \text{ ms}^{-1}$  at midlevels. The vertical east-to-west ( $Y = -21.5$ ) and north-to-south ( $X = 16$ ) cross sections through the core of this downdraft showed the location of  $D_5$  within high reflectivity (50 dBZ). Thus, precipitation loading was an important factor in its maintenance. This downdraft possessed greater strength below cloud base where enhanced evaporational cooling took place. This led to stronger downdraft outflow which produced stronger convergence and enhanced uplifting along the eastern flank of the cell. A portion of downdraft  $D_4$  was still apparent at 1349 to the south of downdraft  $D_5$ . This portion of downdraft  $D_4$  was less prominent, and was weaker than downdraft  $D_5$ . Fig. 5.9 shows that the updraft core ( $U_5$ ) was on the east of downdraft  $D_5$ . This west to east alignment of downdraft and updraft may have been responsible for the subsequent rapid eastward propagation of the storm system which soon began to weaken after this time. Analyzed divergence patterns for 1349 time period are shown in Fig. 5.11. At the 0.5 km AGL, convergence weakened since 1343, perhaps signalling the first signs of weakening of the storm. A convergent region at mid-level was coincident with downdraft ( $D_5$ ) at that level, and was indicative of the deceleration of easterly inflow due to the strong blocking of the downdraft core. Divergence at upper level was

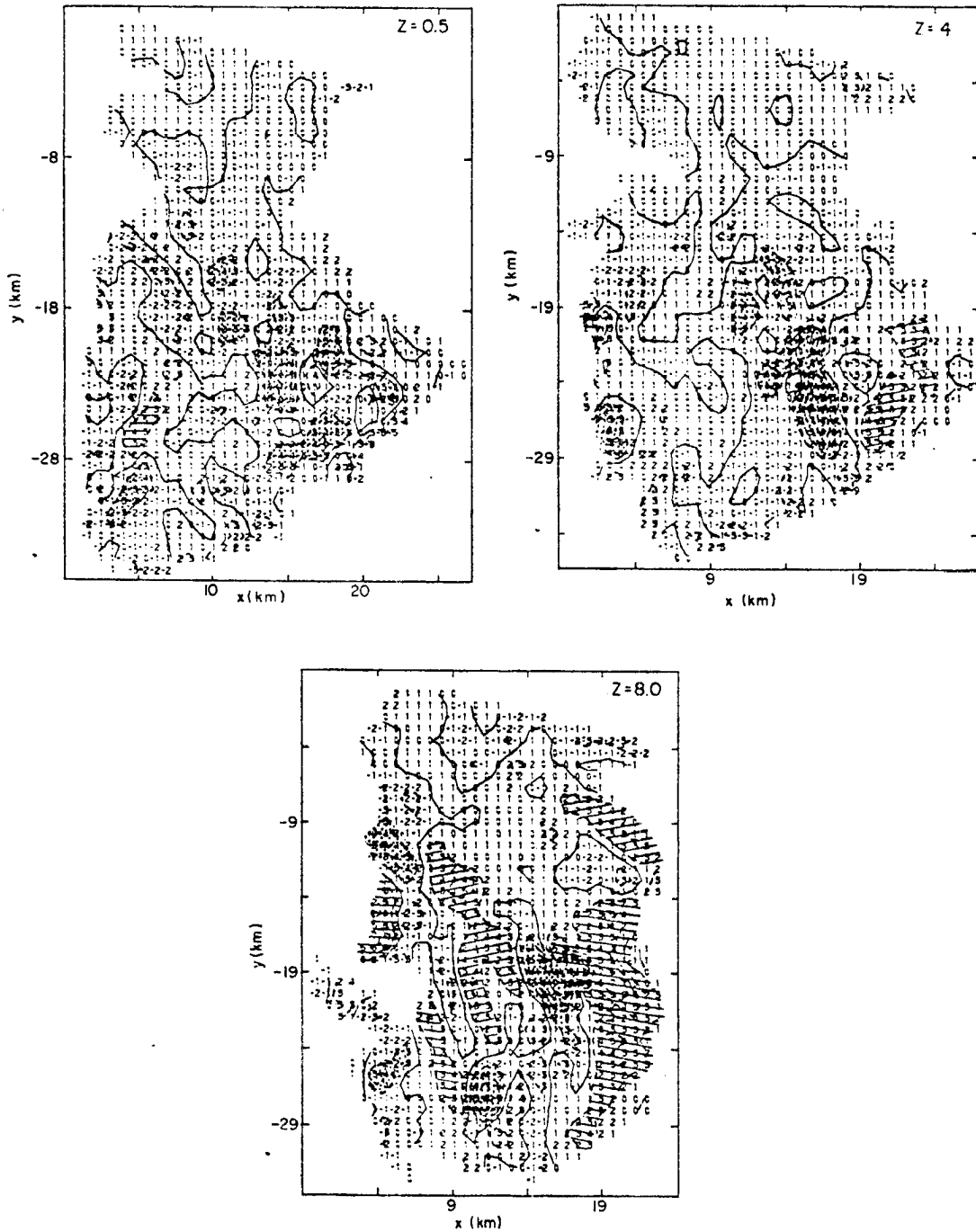


Fig. 5.11. Analyzed divergence patterns for 1349 time period. Contours are in  $2.0 \times 10^{-3}$  intervals. Divergence  $> 2 \times 10^{-3}$  are cross hatched; and  $< -2.0 \times 10^{-3}$  are stippled.

associated with upper level horizontal outflow which occurred at that level.

Analyzed vertical motions were used to calculate vertical profiles of mass flux (Fig. 5.12) at 1327, 1343 and 1349 MDT. While both the updraft and downdraft mass flux profiles are subject to increasing errors at lower heights, the net vertical mass flux profile is not subject to analysis errors (Nelson, 1980). At 1327, the net mass flux peak near 4 km AGL apparently resulted from the combination of the main updraft ( $U_1$ ) and secondary updraft ( $U_2$ ). The analyzed updraft mass flux exhibits a maximum of  $\sim 700 \times 10^6 \text{ kg s}^{-1}$  at  $\sim 3.5$  km AGL. The downdraft mass flux peaks at some level below  $Z = 2$ . By 1343, the net mass flux and updraft mass magnitudes are approximately two times greater than that at 1327. Thus, the approach or collision of gust fronts/downdrafts from adjacent cells ( $C_3$  and  $C_4$ ) at 1343 can force more upward warm moist air into the updrafts. By 1349, the net mass flux peak of  $900 \times 10^6 \text{ kg s}^{-1}$  near 6 km AGL suggests greater upward mass flux than at 1343 (shortly after this time an echo merging occurred). The updraft mass magnitude at 1349 is approximately similar to the magnitude of a Great Plains squall line thunderstorm inferred by Newton (1966). Finally, The updraft speed or mass flux at 1349 suggests that the storm's most vigorous stages occurred during this time.

### 5.3 Precipitation Efficiency

Typically, in observational studies of convective storms, precipitation efficiencies are calculated as the ratio of the measured precipitation rate at the surface to the moisture flux through the cloud base. In the present case, precipitation rates and water vapor fluxes were calculated for these sampling periods at 1327, 1343 and 1349 MDT.

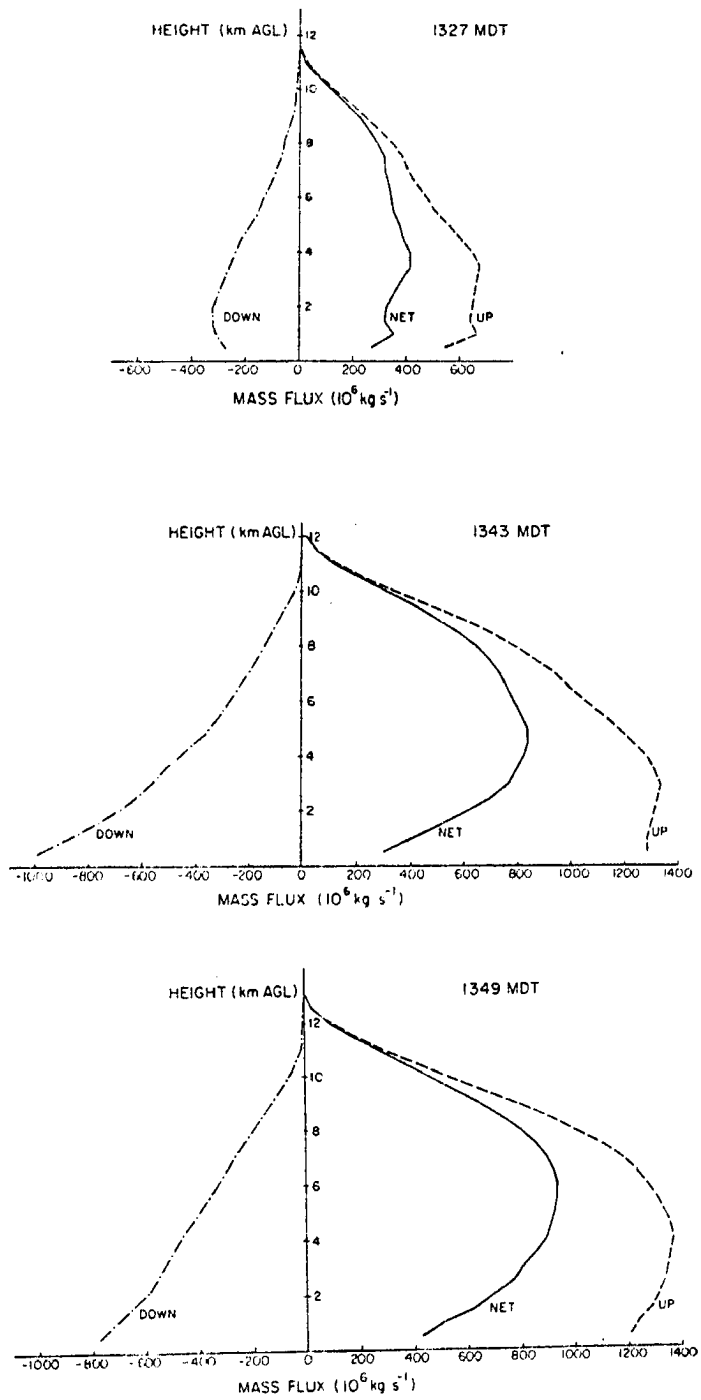


Fig. 5.12. Vertical profiles of mass flux for 1327, 1343 and 1349 time periods.

Precipitation rates were estimated from radar data. Since the CP-3 reflectivity was underestimated because of minor hardware problems, a 5 dBZ correction was added to the processed values to account for this systematic error. No correction was made to account for attenuation by intervening gases ( $O_2$  and  $H_2O$ ) and precipitation. Ground clutter contamination of reflectivities is negligible in most of the cases examined. With these corrections, good agreement between estimated reflectivity factors and observed rainfall rates was found using the relation  $Z = 435 R^{1.48}$  derived for Illinois thunderstorms by Jones and Mueller (1960). Table 5.1 lists reflectivity factor and corresponding rainfall rate values for this relation.

TABLE 5.1. Conversion between reflectivity factor and rainfall rate from  $Z = 435 R^{1.48}$

REFLECTIVITY FACTOR (dBZ)	30	35	40	45	50	55	60	62
RAINFALL RATE ( $\text{mm hr}^{-1}$ )	1.8	3.8	8.3	18	39	86	187	255

If the rainfall rates  $R$  were known, then at a given time the total rate of precipitation from the storm could be computed from

$$P = \rho_w \int R \, dA, \quad (5.1)$$

where  $\rho_w$  is the density of water ( $1000 \text{ kg m}^{-3}$ ) and the integration extends over the region experiencing rain at that time. At this point, it is appropriate to mention that radar estimated rainfall cannot be adjusted with surface rain gauges, because rainfall data were sparse in the region affected by the storm, and most of the PAM stations did not

record the precipitation rates during the period that the CP-3 radar was recording the data.

Values of water vapor flux through the cloud base were computed to be the product of the updraft speed, updraft area, density of the air at the sampling altitude and mixing ratio. Thus, the moisture flux through the cloud base can be given by

$$F = \rho_{\text{air}} W q_v A, \quad (5.2)$$

where  $\rho_{\text{air}}$  is the cloud base air density ( $0.8089 \text{ kg m}^{-3}$ )  $q_v$ , the mixing ratio at the cloud base ( $10.5 \text{ g kg}^{-1}$ )  $W$ , the updraft speed, and  $A$  the updraft area. South Park soundings indicated that the mixing ratio at cloud base had changed little in both time and space. The vertical air motion at the cloud base was determined from upward integration of the anelastic continuity equation using the boundary condition  $W = 0.0 \text{ ms}^{-1}$  at  $Z = 0$ .

The result of calculations of precipitation rates, water vapor fluxes and precipitation efficiencies during the sampling periods of interest appears in Table 5.2.

TABLE 5.2. Rainfall rate, upward water vapor flux, and precipitation efficiency for sampling time.

TIME MDT	RAINFALL RATE KT sec <sup>-1</sup>	WATER VAPOR FLUX KT sec <sup>-1</sup>	PRECIPITATION EFF. %
1327	262	1,416	18.5 %
1343	920	4,823	19.1 %
1349	1,198	3,778	31.7 %

At 1327 MDT, precipitation efficiency was 18.5% which means that only about 18% of the water vapor entering the cloud base is eventually measured as precipitation. Thus, there are other losses which should be considered. A portion of the condensed water can be evaporated in the downdraft which thereby is maintained in nearly saturated descent. The exact amount of water involved depends on the mass of the downdraft, the temperature and pressure of the levels from which it originates, and the temperature and pressure with which it reaches the ground. Other ways include water left behind as cloud water after the major vertical motions of the storm have dissipated, and water loss due to direct evaporation of condensate by entrainment processes. It should be mentioned that these terms cannot be evaluated from the radar. Braham (1952) also calculated precipitation efficiencies by comparing the total amount of measured precipitation at the ground to the total moisture inflow of small, individual, air mass thunderstorms with a typical lifetime of 25 minutes. He inferred that only about 15% of the water vapor entering these thunderstorms is eventually measured as precipitation at the ground.

Table 5.2 indicates that the total precipitation rate increased substantially at 1343, peaking at 1349 when rapid growth, resulting in the merger, was forced by the intersection of the gust fronts. Consistent with these results, Simpson et al. (1980) defined shower merger in south Florida in terms of radar echoes joining at the rain rate of  $1 \text{ mm h}^{-1}$ . This merger study showed first-order mergers produced an order of magnitude more rain than unmerged echoes, while second-order mergers produced another order of magnitude more, primarily owing to greater size and secondarily to longer duration. Although not

specifically mentioned by Simpson et al. (1980), the merged cloud system is also considerably more efficient than its unmerged counterpart.

The vapor flux fluctuation shows a strong growth, peaking at 1343, but maximum rainfall occurred at 1349 or 6 minutes after the maximum water vapor flux. This indicates that there is a time lag between maximum moisture flux into the storm and its subsequent condensation, growth and fall out as rain (McNab and Betts, 1978). This contributes to the rate of storage and its effects on the precipitation efficiency. As noted above, the maximum precipitation efficiency occurred at 1349 following cloud merger.

#### 5.4 Conceptual Models

Fig. 5.13 portrays a conceptual model of flow patterns at 1327 MDT. The major updraft ( $U_1$ ) was due to low level easterly flow rising in organized updrafts, forced by horizontal convergence along a N-S convergence line. Its easterly momentum was maintained in the updraft and as a consequence, updraft  $U_1$  tilted westward from lower level to upper levels. The 1327 time period shows the last stage of a strong updraft  $U_1$ , which has been cut off from its source by downdraft  $D_1$ . This downdraft was formed primarily by precipitation loading on the eastern side of  $U_1$  in a region which was probably updraft a few minutes earlier. The formation of downdraft  $D_1$  was enhanced by evaporational cooling of entrained low-valued  $\theta_e$  mid-level air. At low levels this downdraft effectively blocked the surface inflow of high-valued  $\theta_e$  air and created a detectable gust front propagating southeastward. This may explain the discrete propagation of cell  $C_1$  towards the southeast, where the forced lifting due to the gust front was strongest. This discrete southeastward propagation is depicted by the  $U_3$  arrows in Fig. 5.13,

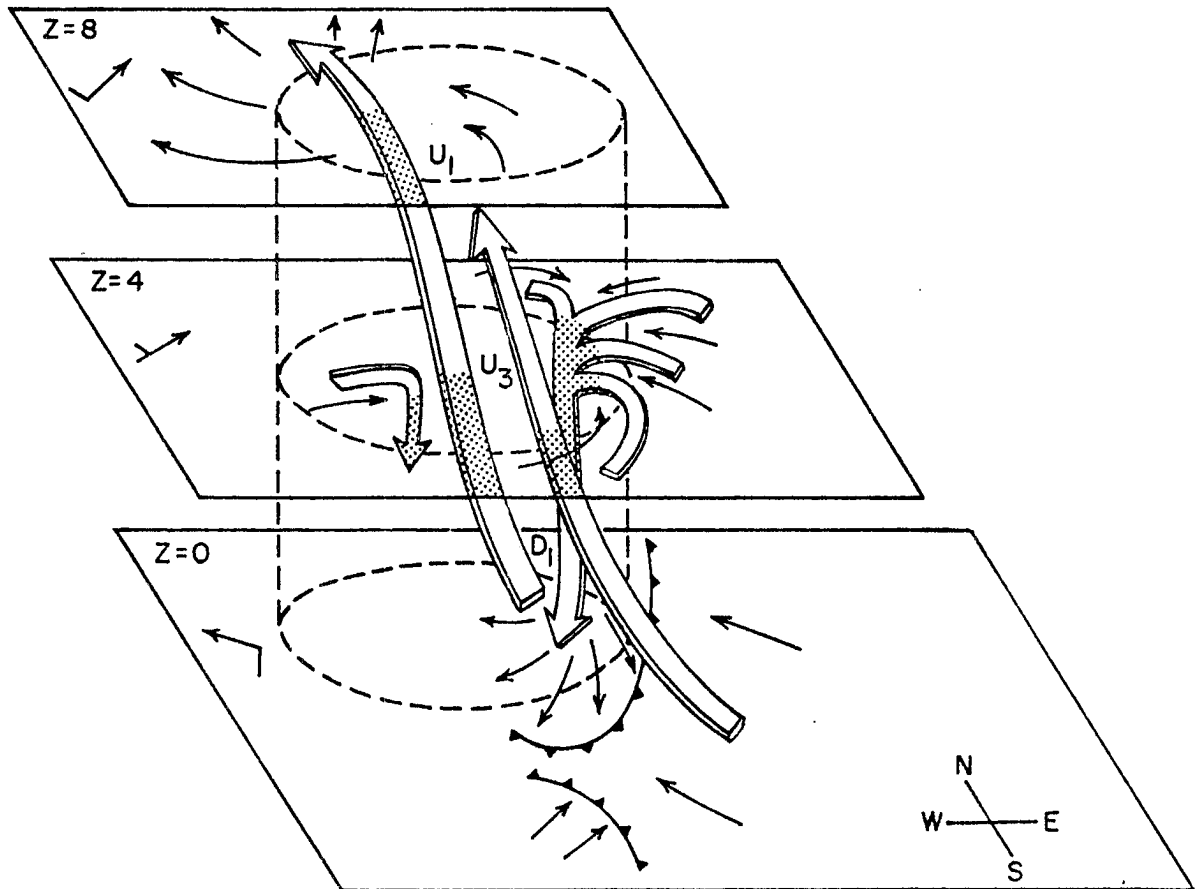


Fig. 5.13. Conceptual model of the flow patterns at 1327 MDT. Streamlines depicts airflow (storm-relative) in the given horizontal planes. The arrowed ribbons represent updraft and downdraft circulations. The shaded portion of ribbons are hidden beneath the depicted planes. Wind barbs at the left of each plane denote undisturbed environmental relative airflow at that level (full barb =  $5 \text{ ms}^{-1}$ ).

which symbolizes a newer updraft penetrating the 4 km level to the southeast of  $U_1$  and not yet reaching the 8 km level. A less intense gust front, associated with a more southern cell complex, is also evident at this time. The PAM data confirmed the existence of this gust front, but the echoes were south of Doppler radar coverage. Horizontal flow within the storm exhibited a divergence pattern at upper level which was associated with upper level horizontal outflow at that level. An approximate circular configuration indicated by the dashed line at this time depicts a single cellular storm structure, with weaker decaying cells from previous multicellular stage to the north.

Fig. 5.14 portrays a conceptual model of flow patterns at 1343 MDT. The formation of updraft  $U_3$ , to the east of the N-S reflectivity core, resulted in a stronger, more sustained cell configuration than at 1327, where the updraft was to the west of the downdraft. At 1343, the location of downdraft  $D_3$  resembles the rear flank downdraft commonly observed within severe hailstorms and tornadic storms (Barnes, 1982; Lemon and Doswell, 1979). This downdraft, located to the west, was a continuous supply of cool air for the expanding gust front, over which unimpeded southeasterly low-level flow could ascent. Although the mid-level storm-relative environmental flow was weak southwesterly (according to 1003 MDT sounding) the Doppler data show easterly flow at this level. This relative easterly flow appears to be the result of a combination of the eastward propagation of the storm system (thereby inducing mid-level easterly-relative flow) and acceleration due to storm-induced, non-hydrostatic pressure deficits through a deep low-to-mid level layer of the storm. As a result deep low-level to mid-level relative easterly flow induced on the east side of the storm, which

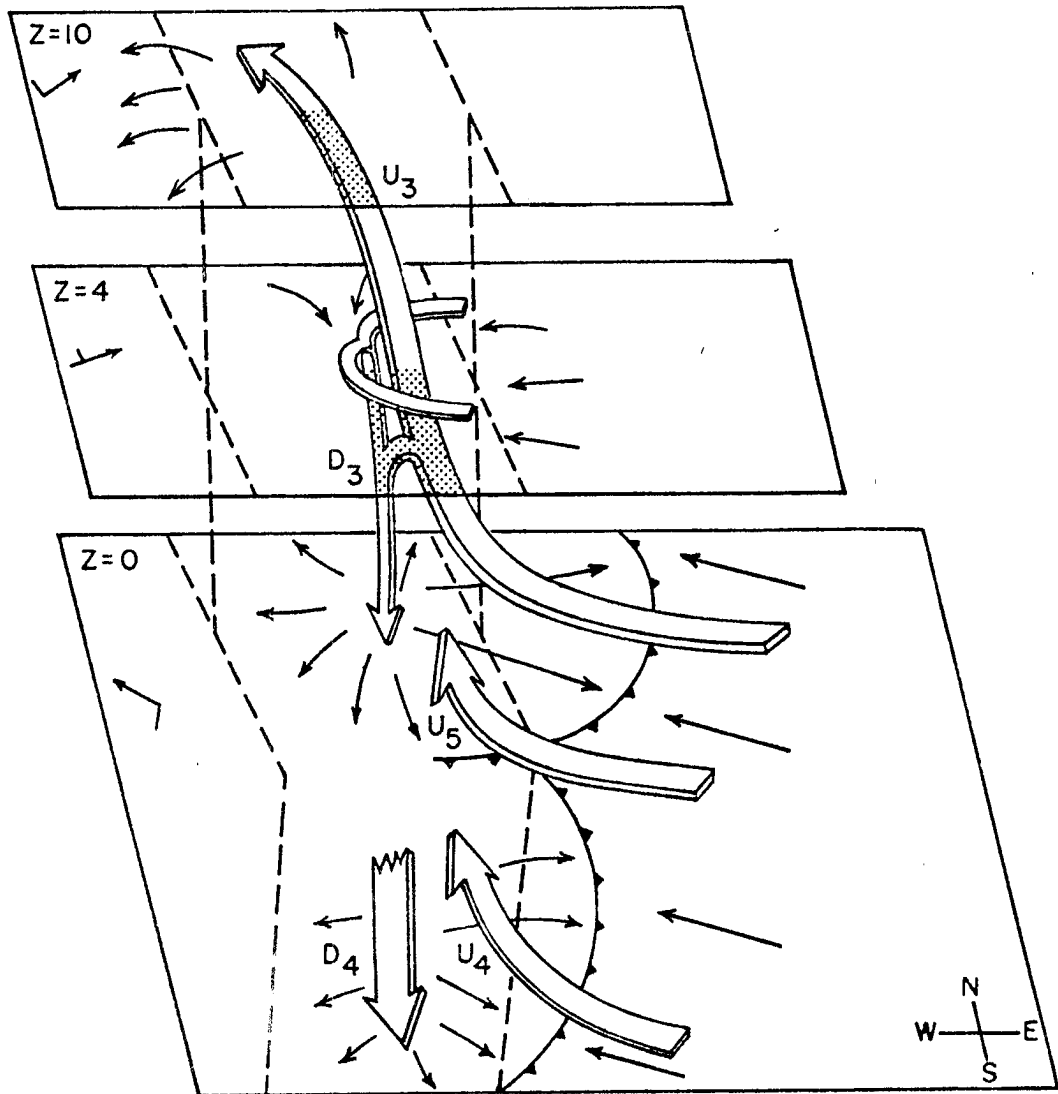


Fig. 5.14. Same as Fig. 5.13, for 1343.

helped to bring low-valued  $\theta_e$  mid level air into the storm at that level and maintained downdraft  $D_3$ . This downdraft was also suggested by precipitation loading beneath updraft  $U_3$ . The persistent downdraft  $D_3$  continually supplied cool air for the expansion of cell  $C_3$ 's gust front east and southeastward, which intersected with cell  $C_4$ 's gust front expanding toward the northeast. The updraft  $U_4$ /downdraft  $D_4$  couplet associated with cell  $C_4$  is only depicted at low levels so as not to interfere with the  $C_3$  schematic pattern, but its configuration is similar to  $C_3$ . The intersection of gust fronts enhanced the forced lifting over the gust fronts, leading to the new development of  $U_5$  near the intersection, which subsequently caused the highest rain observed on this day. This evolution sequence gives the impression of a merger between  $C_3$  and  $C_4$ , through the discrete formation of  $U_5$ . The approximate linear configuration indicated by the dash line at this time depicts the linear stage of the storm. The divergence pattern at upper levels ( $Z = 10$ ) responded to the development of the updraft and vertical expansion of the storm since 1327 MDT which divergence occurred at 8 km AGL.

The following sequence of events are hypothesized to account for the transition of the updraft/downdraft structure depicted in Fig 5.13 to that in 5.14. At the early stage, low level convergence along a N-S line was the main forcing mechanism, and updraft  $U_1$  formed due to low level easterly flow rising in organized updraft, forced by this convergence. The formation of a downdraft on the eastern side of  $U_1$  blocked the surface inflow of high-valued  $\theta_e$  air and created a detectable gust front. As the original downdraft on the eastern side of the storm developed and intensified, the accumulation of evaporationally

chilled air caused the intensification of the mesohigh, which likely destroyed the earlier convergence line and created a stronger convergence line to the east at the interface between the downdraft outflow and the low level easterly flow. The strong low level convergence line forced up-lifting of the moist inflow from the east and caused the formation of the updraft to the east at the later time.

### 5.5 Vorticity Structure

Analyzed vorticity patterns for 1327 time period are shown in Fig. 5.15. At  $Z = 4$ , the main features are the cyclonic vorticity maximum ( $5 \times 10^{-3} \text{ s}^{-1}$ ) in the southeastern quadrant of the storm and the anticyclonic maximum ( $-5 \times 10^{-3} \text{ s}^{-1}$ ) associated with the updrafts. The patterns at 0.5 km AGL appear to follow the same trend. At  $Z = 8$ , anticyclonic vorticity continues to be associated with the updraft. In general, the vorticity patterns are weak, but there is a cyclonic/anticyclonic vorticity couplet from low to mid levels on the south/north side of the strong low-to mid-level inflow.

By 1343, the vorticity maximum increased in magnitude since the 1327 MDT. At low levels, the cyclonic/anticyclonic vorticity couplet (Fig. 5.16) was centered on the leading edge of the strong easterly inflow, with strong cyclonic vorticity on the southern side of the maximum inflow axis. To the south of this cyclonic vorticity region, another anticyclonic vorticity center was co-located with the downdraft and reflectivity core associated with cell  $C_4$ . This configuration suggests an intensification mechanism similar to the Lemon and Doswell's (1979) model of severe storm situations, whereby the anticyclonic surface outflow originated from strong downdrafts, forced the gust front on the southeast flank of the storm, and helped force

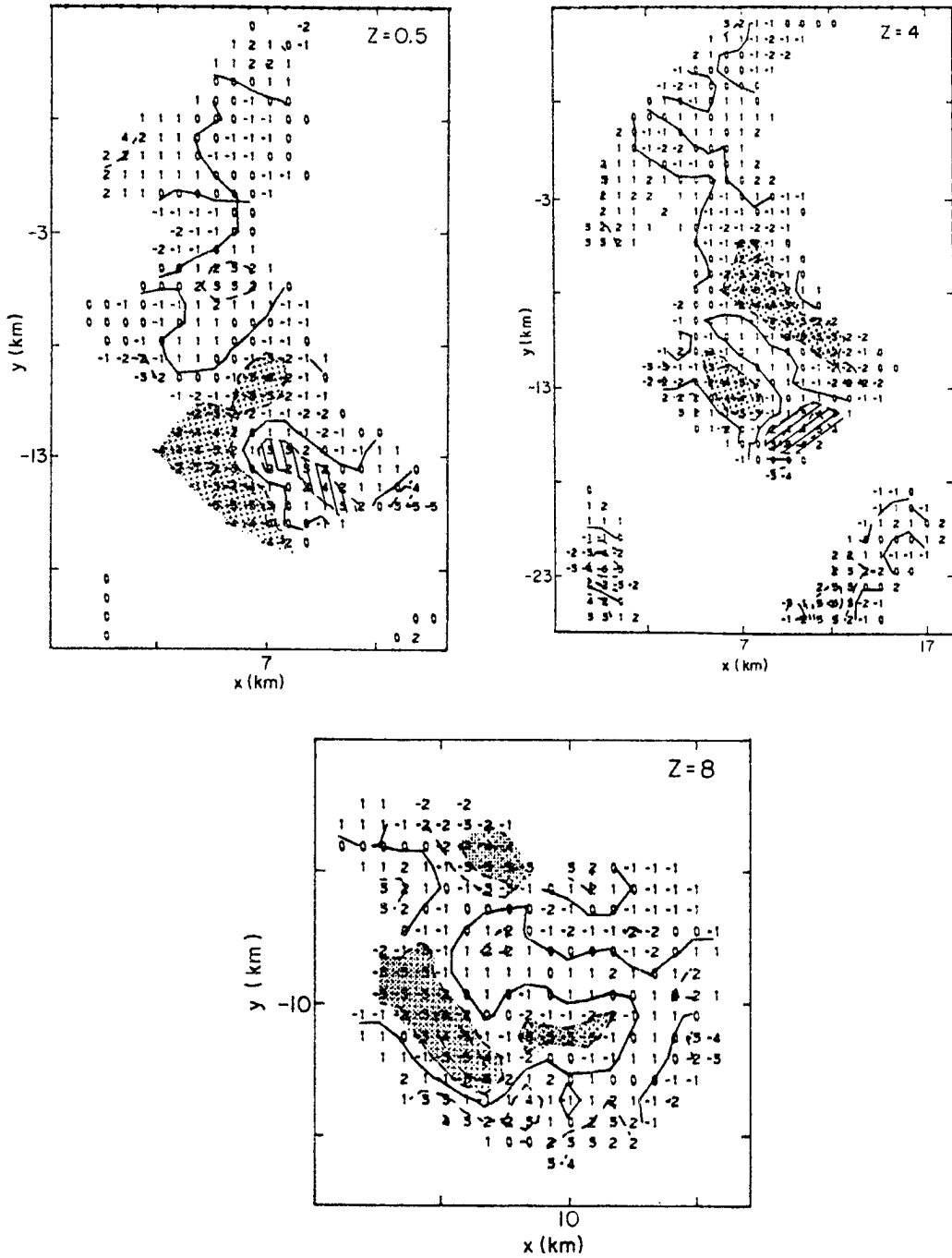


Fig. 5.15. Analyzed vorticity patterns for 1327 time period. Contours are in  $2.0 \times 10^{-3}$  intervals. Hatched and stippled areas represent major cyclonic and anticyclonic vorticity regions, respectively.

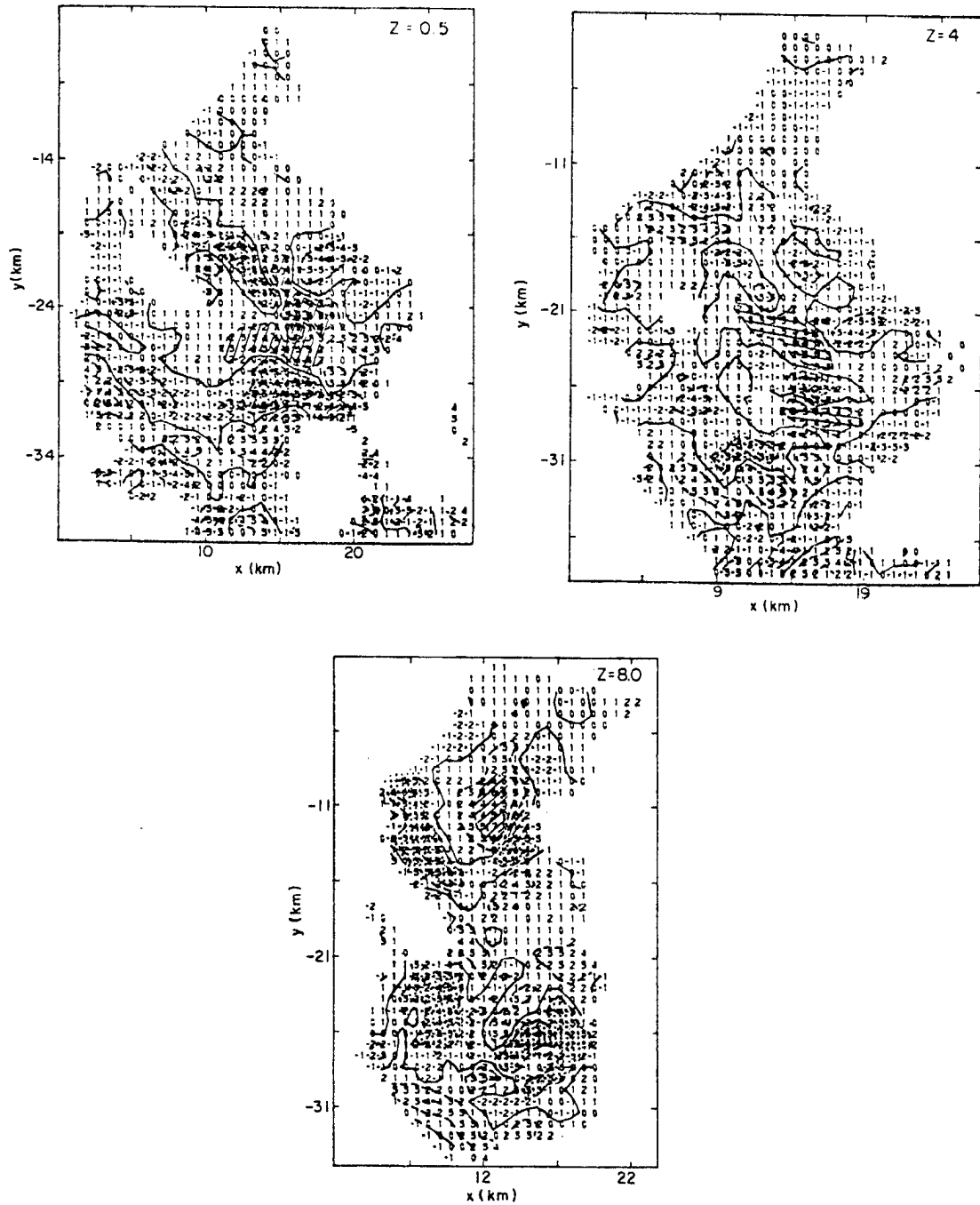


Fig. 5.16. Same as Fig. 5.15, for 1343 MDT.

the low-level environmental inflow upward. This inflow was most enhanced in the cyclonic vorticity region, suggesting a mesolow near the gust front intersection and between cells  $C_3$  and  $C_4$ . The mesolow, however, was not as strong as in a severe storm case. Subsequent storm development was strongest in that region and resulted in a merger of cells  $C_3$  and  $C_4$  by 1349 MDT. The cyclonic inflow/anticyclonic outflow couplet persisted from 1343 to 1349 (Fig. 5.17), which may be partly responsible for the N-S echo orientation becoming shifted more NNW-SSW.

A simple examination of the vorticity equation was made in order to assess which processes may be dominant in the observed vorticity intensification. Following a parcel in the storm relative frame, the vorticity equation may be given as

$$\frac{\partial \xi}{\partial t} + \mathbf{V} \cdot \nabla \xi + w \frac{\partial \xi}{\partial Z} = -(\nabla \cdot \mathbf{V}) \xi + \frac{\partial \mathbf{V}}{\partial Z} \times \nabla W. \quad (5.3)$$

The first three terms on the LHS are the local change, horizontal advection, and vertical advection of the relative vorticity. The last two terms on the RHS are the stretching and tilting terms, respectively. The solenoidal and turbulence terms have been ignored based on scale analysis of the vorticity equation by Heymsfield (1978). These terms cannot be evaluated by radar. The solenoidal term is thought to be of small magnitude in initiation of vorticity at mid-levels because density and pressure gradients tend to be parallel. The tilting term was judged to be small due to very weak environmental wind shear and speed. The horizontal advection term was also small, since vorticity gradients were small at 1327 on both the environmental and storm scales. A rough estimate of low level environmental vorticity based on PAM data ahead of the gust front, suggested that the stretching term could be

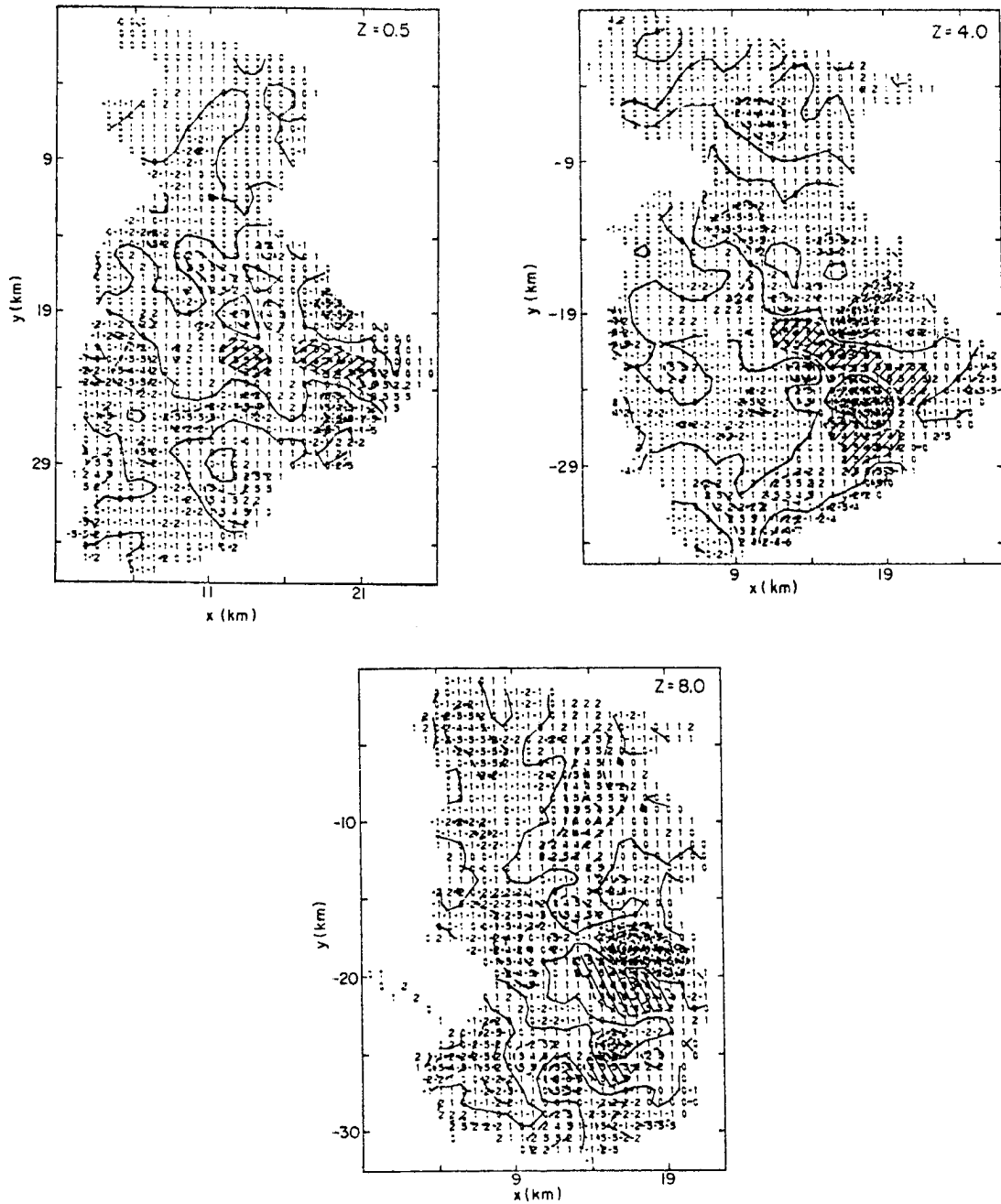


Fig. 5.17. Same as Fig. 5.15, for 1349 MDT.

appreciable in spinning up the environmental vorticity in the region of strong convergence. Vertical advection may then have been significant in transporting cyclonic vorticity at low levels at 1343 (see Fig. 5.16) to upper levels (8 km) by 1349 (Fig. 5.17).

## 6. SUMMARY AND CONCLUSIONS

The present case study has disclosed some of the properties of the evolution of a thunderstorm complex over the South Park region in central Colorado on 20 July 1977. The synoptic flow patterns were weak and confined to the lower elevations over the plains and did not significantly affect the local circulations that evolved over South Park. Likewise, the upper level flow over Colorado was weak ( $\sim 10 \text{ m s}^{-1}$ ) from the south and southwest. Little thermal and moisture advection was occurring, and the polar jet was located well to the north in southern Canada. Thus, the surface flow in South Park on the early morning of 20 July evolved in a manner quite typical for weak summertime synoptic situations. The following scenario accounts for the observed mesoscale and cloud-scale event.

During stage I, a well-established drainage flow (westerly and northwesterly) of cool air was indicated in central South Park at 0600 MDT. After sunrise, surface heating below the cold pool caused a gradual erosion of the nocturnal inversion layer from below and also produced valley/upslope flow within the heated layer next to the ground. When this regime became well established during the later morning hours, the east-facing slopes of South Park were a region where upslope winds with an easterly component met with convectively-mixed winds with a westerly component. The region of intersection between the two wind regimes generated a line of convergence (Banta, 1982).

During stage II, the convergence line subsequently propagated down the slope. Therefore, for the case of July 20, the convective clouds first formed along the eastern slopes of the Mosquito Range. The organized clouds were on the mesoscale, observed to have an updraft/downdraft structure with the major updraft ( $U_1$ ) fed by low level easterly flow rising in organized updrafts and forced by horizontal convergence along a N-S convergence line. This time period shows the last stage of a strong updraft which had been cut off from its source by downdraft  $D_1$ . This downdraft, located on the eastern flank of the updraft, was formed by precipitation loading on the eastern side of  $U_1$ . The formation of this downdraft enhanced by evaporational cooling of entrained low-valued  $\theta_e$  mid-level air, effectively blocked the surface inflow of high-valued  $\theta_e$  air and created a detectable gust front propagating southeastward. This may explain the discrete propagation of the storm towards the SE, where the forced lifting due to the gust front was strongest.

During stage III, as precipitation volume increased, an intense downdraft spread laterally beneath the convective clouds and a strong gust front marked its leading edge. The gust front provided low-level convergence which corresponded to the eastward propagation of the system from the mountain slopes over the flat regions of South Park. As a consequence of the eastward propagation of the storm, a relative easterly flow was induced at mid-levels. Downdrafts thus developed on the western flank of the updraft producing an updraft/downdraft couplet in which downdrafts supplied potentially cool air for the expansion of the gust front, over which unimpeded potentially warm southeasterly flow could then ascend into convective towers. The formation of an updraft

to the east of the N-S reflectivity core, resulted in a stronger, more sustained cell configuration than earlier, when the updraft was to the west of the downdraft. A similar updraft/downdraft couplet associated with cell  $C_4$  was located to the southeast of cell  $C_3$ . The intersection of gust fronts enhanced the forced lifting over the gust fronts, leading to the new development of an updraft near the intersection, where subsequently the strongest development occurred with the merger of cells  $C_3$  and  $C_4$ . This merging process corresponded to an increase in the precipitation efficiency of the storm and a further increase in the precipitation volume of the storm.

The storm also exhibited a vorticity couplet at low-to mid-levels which apparently had some effect on the storm intensification. At the early stage, the vorticity patterns were weak, as time proceeded, the vorticity maximum increased in magnitude. The cyclonic/anticyclonic vorticity couplet was centered on the leading edge of the strong easterly inflow, with strong cyclonic vorticity on the southern side of the maximum inflow axis. To the south of this cyclonic vorticity region, another anticyclonic vorticity center was co-located with the downdraft and forced the gust front on the southeast flank of the storm, and helped force the low-level environmental inflow upward.

Several conclusions can be drawn from the results of this case study analysis. It is concluded that in the environment of weak flow, the storm owed its intensification to the strength of the downdraft which was nearly coincident with the region where the cloud had grown. Downdraft circulations appeared to be driven primarily by precipitation loading and negative buoyancy due to evaporational cooling, in addition to possible dynamic forcing. Interactions of storm outflow with the

low-level winds produced very little relative motion between the storm and gust front. Such a balance maintained the updraft circulation by supplying a constant flux of moist static energy to the updraft and by providing continuous lifting beneath the updraft. In addition, the same interactions produced eastward propagation of the storm at about  $5 \text{ m s}^{-1}$ . Similar to this case, Moncrieff and Miller (1976) also used theory and numerical simulations to discuss the maintenance of tropical cumulonimbi. They argue that under certain conditions a density current due to a diverging downdraft near the ground propagates at the same speed as the cloud and the net result is a convergent region beneath the updraft, forcing continuous uplifting of the moist low-level inflow along the right flank. In this manner the storm maintains its moisture supply and tends to propagate to the right. In the July 20 case, the storm attained its highest intensity as a consequence of merging with a neighboring cloud. The interaction of downdrafts or gust fronts from two intense cells appeared to be the primary mechanism of this merging process as suggested by Simpson et al. (1980). Likewise, the merging process coincided with more rain than occurred in the unmerged echoes.

Finally, due to communication failures and shared use of the radar facilities, coordinated radar scans were not taken as frequently as needed to resolve details in the evolution of updraft/downdraft structure. Likewise, because of the long time lapse between successive scans and, therefore, analysis, it is impossible to adequately quantify the dynamic structure of the storm. Thus, it is necessary to obtain greater temporal resolution in the analysis. Moreover, the numerical simulation of the storm could help to investigate the storm in greater detail.

## REFERENCES

- Amijo, L., 1969: A theory for the determination of wind and precipitation velocities with Doppler radars. J. Atmos. Sci., 26, 570-573.
- Atlas, P., 1964: Advances in radar meteorology. In Advances in Geophysics, Academic Press, New York, 10, 318-478.
- Banta, R., and W.R. Cotton, 1981: An analysis of the structure of local wind systems in a broad mountain basin. J. Appl. Meteor., 20, 1255- 1266.
- Battan, L.S., 1973: Radar Observation of the Atmosphere. University of Chicago Press, 324 pp.
- Baynton, H.W., R.J. Serafin, C.L. Frush, G.R. Gray, P.V. Hobbs, R.A. Houze, Jr., and J.D. Locatelli, 1977. Real-time wind measurement in extra- tropical cyclones by means of Doppler radar. J. Appl. Meteor., 16, 1022-1028.
- Betts, A.K., 1973a: A composite mesoscale cumulonimbus budget. J. Atmos. Sci., 30, 597-610.
- \_\_\_\_\_, 1974: The scientific basis and objectives of the U.S. Convection Subprogram for the GATE. Bull. Amer. Meteor. Soc., 55, 304-313.
- \_\_\_\_\_, 1976: The thermodynamic transformation of the tropical subcloud layer by precipitation and downdrafts. J. Atmos. Soc., 33, 1008-1020.

- \_\_\_\_\_, 1978: Convection in the tropics. Meteorology over the tropical oceans. Bracknell, England. Roy. Meteor. Soc., 105-132.
- Bohne, A.R., and R.C. Srivastava, 1975: Random errors in wind and precipitation fall speed measurements by a triple Doppler radar system. Tech. Rep. No. 37, Lab. Atmos. Probing, Univ. of Chicago, 94 pp.
- \_\_\_\_\_, and R.C. Srivastava, 1976: Random errors in wind and precipitation fall speed measurements by a triple Doppler radar system. Preprints 17th Radar Meteor. Conf., Seattle, Amer. Meteor. Soc., 7-14.
- Braham, R.R., 1952: The water and energy budgets of the thunderstorm and their relation to thunderstorm development. J. Meteor., 9, 227-242.
- Brandes, E.A., 1977: Flow in severe thunderstorms observed by dual Doppler radar. Mon. Wea. Rev., 105, 113-120.
- Brandes, E., 1978: Mesocyclone evolution and tornadogenesis. Some observations. Mon. Wea. Rev., 106, 995-1011.
- Breed, D.W., 1979: Liquid water measurements in high evaluation continental cumuli. NCAR Cooperative Thesis No. 57, Colorado State University and National Center for Atmospheric Research, 104 pp.
- Brock, F.V., and P.K. Govind, 1977: Portable automated mesonet in operation. J. Appl. Meteor., 16, 299-310.
- Brooks, C.F., 1922: The local, or heat, thunderstorm. Mon. Wea. Rev., 50, 281-287.
- Brown, J.M., 1974: Mesoscale motions induced by cumulus convection: A numerical study. Ph.D. thesis, Massachusetts Institute of Technology, 206 pp.

- Brown, J.M., 1979: Mesoscale unsaturated downdrafts driven by rainfall evaporation: A numerical study. J. Atmos. Sci., 36, 313-337.
- Browning, K.A., 1977: The structure and mechanisms of hailstorms. Meteor Monogr. No. 38, 1-43.
- \_\_\_\_\_, 1964: Airflow and precipitation trajectories within severe local storms which travel to the right of the winds. J. Atmos. Sci., 21, 634-639.
- \_\_\_\_\_, and G.B. Foote, 1976: Airflow and hail growth in supercell storms and some implications for hail suppression. Quart. J. Roy. Meteor. Soc., 102, 499-533.
- \_\_\_\_\_, and F.H. Ludlam, 1962: Airflow in convective storms. Quart. J. Roy. Meteor. Soc., 88, 117-135.
- \_\_\_\_\_, and R. Wexler, 1968: The determination of kinematic properties of a wind field using Doppler radar. J. Appl. Meteor., 7, 105-113.
- Burgess, D., L. Hennington, R. Doviak and P.S. Ray, 1976: Multimoment Doppler display for severe storm identification. J. Appl. Meteor., 15, 1302-1306.
- Byers, H.R. and R.R. Braham, 1949: The Thunderstorm. U.S. Weather Bureau, Washington, D.C., 287 pp.
- Clark, T.L., F.I. Harris, and C.G. Mohr, 1979: An error analysis of multiple-Doppler radar and wind retrieval using numerical model data. Preprints 11th Conf. on Severe Local Storms, AMS, 503-508.
- \_\_\_\_\_, F.I. Harris and C.G. Mohr, 1980: Errors in wind fields derived from multiple-Doppler radars: Random errors and temporal errors associated with advection and evolution. J. Appl. Meteor., 19, 1273-1284.

- Cotton, W.R., 1972: Numerical simulation of precipitation development in supercooled cumuli. Mon. Wea. Rev., 100, 764-784.
- \_\_\_\_\_, and G. Tripoli, 1978: Cumulus convection in shear flow three-dimensional numerical model experiments. J. Atmos. Sci., 35, 1503-1521.
- \_\_\_\_\_, R.L. George, P.J. Wetzell, and R.L. McAnelly, 1982: A long-lived mesoscale convective complex, Part I: The mountain generated component. Submitted for publication in Mon. Wea. Rev.
- Danielson, K.S., 1975: Continental mountain cumulus clouds. M.S. Thesis, Colorado State University, Fort Collins, Colorado, 172 pp.
- Das, P., and M.C. Subba Rao, 1972: The unsaturated downdraft. Ind. J. Meteor. Geophys., 23, 135-144.
- Emanuel, K.A., 1981: A similarity theory for unsaturated downdrafts within clouds. J. Atmos. Sci., 38, 1541-1557.
- Fankhauser, J.C., 1971: Thunderstorm-environment interactions determined from aircraft and radar observations. Mon. Wea. Rev., 99, 171-192.
- Fawbush, E.J., and R.C. Miller, 1954: The types of air masses in which North American tornadoes form. Bull. Amer. Meteor. Soc., 35, 154-165.
- Fujita, T.T., 1976: Spearhead echo and downburst near the approach end of a John F. Kennedy airport runway, New York City. SMRP Res. Pap. 137, University of Chicago.
- \_\_\_\_\_, and F. Caracena, 1977: An analysis of three weather-related aircraft accidents. Bull. Amer. Meteor. Soc., 58, 1164-1181.

- George, R.L., and W.R. Cotton, 1978: The characteristics of evolving mesoscale systems over mountainous terrain as revealed by radar and PAM. Preprints of AMS Conf. on Cloud Physics and Atmospheric Electricity.
- Gerrish, M.P., 1969: Intersecting fine lines and a South Florida tornado. Preprints Conf. on Severe Local Storms, Chicago, AMS, 188-191.
- Gray, G.R., R.J. Serafin, D. Atlas, R.E. Rinehart and J.J. Bouajian. 1975: Real-time color Doppler radar display. Bull. Amer. Meteor. Soc., 59, 580-588.
- Henz, J., 1974: Colorado high plains thunderstorm systems--a descriptive radar-synoptic climatology. M.S. Thesis, Dept. of Atmospheric Science, Colorado State University, Fort Collins, Colorado.
- Heymsfield, A.J., D.N. Johnson, and J.E. Dye, 1970: Observations of moist adiabatic ascent in northeast Colorado cumulus congestus clouds. J. Atmos. Sci., 35, 1689-1703.
- Heymsfield, G.M., 1981: Evolution of downdrafts and rotation in an Illinois thunderstorm. Mon. Wea. Rev., 109, 1964-1988.
- \_\_\_\_\_, 1978: Kinematic and dynamic aspects of the Harrah tornadic storm analyzed from Dual-Doppler radar data. Mon. Wea. Rev., 106, 233-254.
- \_\_\_\_\_, and R.C. Srivastava, 1980: Doppler observation of the evolution of a thunderstorm. Preprints 19th Conf. Radar Meteor., AMS, 342-349.

- Holle, R.L., and M. Maier, 1980: Tornado formation from downdraft interaction in the FACE mesonet network. Mon. Wea. Rev., 108, 1010-1028.
- Hookings, G.A., 1965: Precipitation maintained downdrafts. J. Appl. Meteor., 4, 190-195.
- Huggins, A.W., 1975: The precipitation sequence in mountain cumuli. M.S. Thesis, Colorado State University, Fort Collins, Colorado, 158 pp.
- Kamburova, P.L., and F.H. Ludlam, 1966: Rainfall evaporation in thunderstorm downdrafts. Quart. J. Roy. Meteor. Soc., 92, 510-518.
- Klemp, J.B., and R.B. Wilhelmson, 1978: The simulation of three dimensional convective storm dynamics. J. Atmos. Sci., 35, 1070-1096.
- Knupp, K.R., and W.R. Cotton, 1981: An intense, quasi-steady thunderstorm over mountainous terrain. Part II: Doppler radar observations of the storm morphological structure. J. Atmos. Sci., 39, 343-358.
- Kropfli, R.A., and L.J. Miller, 1976: Kinematic structure and flux quantities in a convective storm from dual-Doppler radar observation. J. Atmos. Sci., 33, 520-529.
- LeCompte, J.L., and G.L. Mulvey, 1978: A possible transient ice collections zone in a singular continental mountain cumulus cloud. Preprints, Conf. of Cloud Physics and Atmos. Electricity, AMS, 337-340.
- Lemon, R.L., and C.A. Doswell, III, 1979: Severe thunderstorm evolution and mesocyclone structure as related to tornadogenesis. Mon. Wea. Rev., 107, 1184-1197.

- Lhermitte, R.M. and M. Gilet, 1976: Acquisition and processing of tri-Doppler radar data. Preprints, 17th Radar Meteorology Conf., Seattle, AMS, 133-138.
- Malkus, J.S., 1955: On the formation and structure of downdrafts in cumulus clouds. J. Meteor., 12, 350-357.
- McNab, A.L., and A.K. Betts, 1978: A mesoscale budget study of cumulus convection. Mon. Wea. Rev., 106, 1317-1331.
- Miller, M.J., 1978: The Hampstead storm: A numerical simulation of a quasi-stationary cumulonimbus system. Quart. J. Roy. Meteor. Soc., 104, 413-427.
- \_\_\_\_\_, and A.K. Betts, 1977: Traveling convective storms over Venezuela. Mon. Wea. Rev., 105, 833-848.
- \_\_\_\_\_, and R.P. Pearce, 1974: A three-dimensional primitive equation model of cumulonimbus convection. Quart. J. Roy. Meteor. Soc., 100, 133-154.
- \_\_\_\_\_, and R. Strauch, 1974: A dual Doppler radar method for the determination of wnd velocities within precipitating weather systems. Remote Sensing of Environment, 3, 219-235.
- Moncrieff, M.W., and M.J. Miller, 1976: The dynamic and simulation of tropical cumulonimbus and squall lines. Quart. J. Roy. Meteor. Soc., 102, 373-394.
- Newton, C.W., 1963: Dynamics of severe convective storms. Meteor. Monogr., No. 27, 33-58.
- \_\_\_\_\_, 1950: Structure and mechanism of the prefrontal squall line. J. Meteor., 7, 210-222.

- \_\_\_\_\_, and H.R. Newton, 1959: Dynamical interactions between large convective clouds and environment with vertical shear. J. Meteor., 16, 483-496.
- Ogura, Y., and T. Takahashi, 1971: Numerical simulation of the life cycle of a thunderstorm cell. Mon. Wea. Rev., 99, 895-911.
- Ray, P.S., R.J. Doviak, G.B. Walker, D. Sirmans, J. Carter, B. Bumgarner, 1975: Dual-Doppler observations of a tornadic thunderstorm. J. Appl. Meteor., 14, 1521-1530.
- \_\_\_\_\_, K.K. Wagner, K.W. Johnson, J.J. Stephens, W.C. Bumgarner, and E.A. Mueller, 1978: Tripple-Doppler observations of a convective storm. J. Appl. Meteor., 17, 1201-1212.
- \_\_\_\_\_, and C. Ziegler, 1977: De-aliasing first-moment Doppler estimates. J. Appl. Meteor., 16, 563-564.
- \_\_\_\_\_, C.L. Ziegler, and W. Bumgarner, 1980: Single- and multiple Doppler radar observations of tornadic storms. Mon. Wea. Rev., 108, 1607-1625.
- Reed, R.J., and E.E. Recker, 1971: Structure and properties of synoptic-scale wave disturbances in the equatorial western Pacific. J. Atmos. Sci., 28, 1117-1133.
- Riehl, H., and R.P. Pearce, 1968: Studies on interaction between synoptic and mesoscale weather elements in the tropics. Atmos. Sci. Paper No. 126, Colorado State University, Ft. Collins, CO.
- \_\_\_\_\_, and J.S. Malkus, 1958: On the heat balance in the equatorial trough zone. Geophysica, 6, 503-538.

- Ruskin, R.E., 1967: Measurements of water-ice budget changes at  $-5^{\circ}\text{C}$  in AgI-seeded tropical cumulus. J. Appl. Meteor., 6, 72-81.
- Schlesinger, R.E., 1978: A three-dimensional numerical model of an isolated thunderstorm: Part I. Comparative experiments for variable ambient wind shear. J. Atmos. Sci., 35, 690-713.
- \_\_\_\_\_, 1980: A three-dimensional numerical model of an isolated thunderstorm. Part II: Dynamics of updraft splitting and mesovortex couplet evolution. J. Atmos. Sci., 37, 395-420.
- Simpson, J., 1979: Downdrafts as linkages in dynamic cumulus seeding effects. J. Appl. Meteor., 19, 477-487.
- \_\_\_\_\_, and G. Van Helvoirt, 1980: Gate-subcloud layer interactions examined using a three-dimensional cumulus model. Beit. Phys. Atmos. (in press).
- \_\_\_\_\_, N.E. Westcott, R.J. Clerman, and R.A. Pielke, 1980: On cumulus mergers. Arch. Meteor. Geophys. Bioklim., (in press).
- Sirmans, D. and B. Bumgarner, 1975: Numerical comparison of five mean frequency estimators. J. Appl. Meteor., 14, 991-1003.
- Squires, P., 1958: Penetrative downdraft in cumuli. Tellus, 10, 381-389.
- Takeda, T., 1971: Numerical simulation of a precipitating convective cloud: The formation of a 'long-lasting' cloud. J. Atmos. Sci., 38, 350-376.
- Thorpe, A.J., and M.J. Miller, 1978: Numerical simulations showing the role of the downdraft in cumulonimbus motion and splitting. Quart. J. Roy. Meteor. Soc., 104, 873-893.

- Tripoli, G.J., and W.R. Cotton, 1980: A numerical investigation of several factors contributing to the observed variable intensity of deep convection over South Florida. J. Appl. Meteor., 19, 1037-1063.
- Ulanski, S., and M. Garstang, 1978: The role of surface divergence and vorticity in the life cycle of convective rainfall. Part II: Descriptive Model. J. Atmos. Sci., 35, 1063-1069.
- Warner, C., J. Simpson, D.W. Martin, D. Suchman, F.R. Mosher, and R.F. Reinking, 1976: Shallow convection on day 261 of GATE: Mesoscale arcs. Mon. Wea. Rev., 107, 1617-1635.
- Wilhelmson, R., 1974: The life cycle of a thunderstorm in three dimensions. J. Atmos. Sci., 31, 1629-1651.
- Wilson, D.A., 1970: NOAA Tech. Rept. ERL 187-WPL13, U.S. Government Printing Office, Washington, D.C.
- Wilson, J.W., 1978a: Comparison of C- and S-band radar reflectivities in northeast Colorado hailstorms. Preprints 18th Conf. on Radar Meteorology, AMS, 271-275.
- Zipser, E.J., 1969: The role of organized unsaturated convective downdrafts in the structure and rapid decay of an equatorial disturbance. J. Appl. Meteor., 8, 799-814.
- \_\_\_\_\_, 1970: The Line Islands Experiment, its place in tropical meteorology and the rise of the fourth school of thought. Bull. Amer. Meteor. Soc., 51, 1136-1146.
- \_\_\_\_\_, 1977: Mesoscale and convective-scale downdrafts as distinct components of squall-line structure. Mon. Wea. Rev., 105, 1568-1598.

## APPENDIX A

### DOPPLER RADAR AND RADAR SCANNING CHARACTERISTICS

Three Doppler radars were implemented for the 1977 South Park Experiment observational program. The characteristics of each are given in Table A.1. Two of the three were identical low power X-band radars. Although they suffer from attenuation because of short wave-length and low transmitted power, their relatively narrow beamwidth and well-behaved sidelobes makes them well suited as research tools for cloud dynamics.

The third radar was NCAR's CP-3 Doppler radar system. It exhibited less ideal beam patterns, with a significant amount of power within the side lobes. Because of this, measured radial velocity patterns contained variable and unknown biases. One advantage of CP-3 is that more data (512 gates) could be acquired at a faster rate because time series were not recorded. Instead, reflectivity and radial velocity were computed in real time and recorded on magnetic tape.

TABLE A.1. Doppler radar specifications

Parameter	CP-3	NOAA/C	NOAA/D
Power (kw)	295	10-20	10-20
Pulse Duration ( $\mu$ s)	1.0	0.5	0.5
Antenna Gain (dB)	40	49	49
Pulse Repetition Period ( $\mu$ s)	933	512	512
Frequency (MHz)	5500	9310	9310
Wavelength (cm)	5.45	3.22	3.22
Beamwidth (degrees)	1.15	0.8	0.8
Unambiguous Velocity ( $\text{ms}^{-1}$ )	14.7	15.7	15.7
Unambiguous Range (km)	140	76.8	76.8
Polarization	horizontal	horizontal	vertical
Number of Range Gates	512	32-64	32-64
Sample Size	128	128	128
Data Processing	real time (pulse pair)	recording of time series	recording of time series

The field locations of each radar are given in Table A.2. All radar were placed within 250 m of each other in elevation. Inter-radar distances were as follows: (a) 29.9 Km between NOAA-D and CP-3; (b) 27.3 Km between NOAA-C and NOAA-D; (c) 37.0 km between CP-3 and NOAA-C (see Fig. 3.1).

TABLE A.2. Radar locations

	CP-3	NOAA/C	NOAA/D
Longitude	105.784 <sup>o</sup>	105.717 <sup>o</sup>	105.997 <sup>o</sup> .br
Latitude	39.358 <sup>o</sup>	39.028 <sup>o</sup>	39.145 <sup>o</sup> .br
Elevation (km MSL)	2.860	2.685	2.926
X coord. (km)	18.3	24.0	0.0
Y coord. (km)	23.7	-12.9	0.0
Z coord. (km)	-0.06	-0.24	0.0

\* Coordinates used in presentation of data in main text

Table A.3 gives the times and characteristics of each radar volume scan. The average separation between raw data points was 450 m for NOAA-D and 160 m for CP-3. The average time between successive scans was 11-12 min., and the total time was about 5 min. Scanning of common storm points was not simultaneous. The best data are from the 204 and 205 volume scans, when radar resolution and temporal coordination were most favorable.

TABLE A.3. Doppler radar scanning characteristics during period of analysis

Volume	Begin Time MDT	End Time MDT	Total Time S	EI. Lim.	EI. Inc.	AZ Lim.	AZ Inc.	Range Gate Spacing (m)	
104	1254:30	1301:45	435	2.1-30.1	1.0	260-325	0.91	450	NOAA-C
201	1305:01	1312:00	389	2.1-27.0	1.0	265-325	1.70	225	
202	1316:01	1322:59	418	2.1-29.1	1.04	266-323	2.55	150	
203	1327:31	1329:55	144	2.1-11.0	.99	267-323	.55	150	
204	1342:00	1347:09	309	2.1-47.0	1.50	237-312	5.19	150	
205	1349:00	1354:20	320	2.1-56.5	1.70	237-312	5.20	150	
206	1357:30	1402:29	299	2.1-60.0	2.0	237-312	5.19	150	
104	No data available at this time								NOAA-D
201	No data available at this time								
202	1316:16	1322:29	373	4.9-80.0	6.83	240-354	.77	450	
203	1327:42	1332:53	311	4.9-70.0	7.23	230-354	.77	450	
204	1341:55	1346:44	289	1.9-44.0	1.50	101-178	.58	450	
205	1349:15	1354:04	289	1.9-49.9	1.71	101-178	.58	450	
206	1357:35	1402:34	299	1.9-60.0	2.0	101-178	.58	450	
104	1254:33	1259:36	303	0.4-34.0	1.1	190-230	1.39	160	CP-3
201	1305:32	1310:40	308	0.5-32.0	1.1	190-230	1.4	160	
202	1316:10	1319:49	219	0.6-24.0	1.1	190-230	1.3	160	
203	1327:30	1331:44	254	0.4-22.5	1.1	180-230	1.3	160	
204	1343:05	1347:10	245	0.5-23.7	1.1	170-220	1.3	160	
205	1349:00	1355:19	379	0.5-22.4	1.1	170-220	1.3	160	
206	1357:30	1403:34	364	0.5-20.7	1.1	170-220	1.3	160	

## APPENDIX B

### ERROR PROPAGATION FROM INTEGRATION OF THE CONTINUITY EQUATION

Information for this section has been taken from Ray et al. (1980). It can be demonstrated theoretically that downward integration may yield more accurate  $w$  estimates than those obtained from upward integration. Due to the atmospheric density stratification, the propagation of the error of  $w$  (or alternatively the variance of  $w$  error) tends to amplify during upward integration and damp during downward integration. Given estimates of horizontal divergence  $D$  at equally spaced levels  $N$  in number and one kinematic boundary condition, and utilizing the layer-averaged divergence, the expression for  $w$  from upward integration (index  $k$  increasing upward) is

$$w_k = (\beta/\alpha)^{k-1} w_1 - (\delta/\alpha) \sum_{i=1}^{k-1} (\beta/\alpha)^{k-i-1} (D_i + D_{i+1}),$$

while for downward integration ( $k$  increasing downward) there follows

$$w_{N-k} = (\alpha/\beta)^k w_N + (\delta/\beta) \sum_{i=1}^{k-1} (\beta/\alpha)^{k-i} (D_{N-i} + D_{N-i+1}).$$

Here  $\alpha = 1 - (k\Delta z)/2$ ,  $\beta = 1 + (k\Delta z)/2$ ,  $\delta = \Delta z/2$ ,  $\Delta z$  is the vertical grid spacing,  $k$  is the negative gradient of  $\log$  air density, and  $w_1$  and  $w_N$  are the kinematic lower and upper boundary conditions, respectively. Neglecting covariance between adjacent  $D$  values and assuming zero mean

error, the appropriate expression for the  $w$  random error variance with upward integration is

$$\sigma^2 (w_k) = (\beta/\alpha)^{2(k-1)} \sigma^2 (w_1) + (\delta/\alpha)^2 \sum_{i=1}^{k-1} (\beta/\alpha)^{2(k-i-1)} \times [\sigma^2 (D_i) + \sigma^2 (D_{i+1})], \quad (B1)$$

while for downward integration

$$\sigma^2 (w_{N-k}) = (\alpha/\beta)^{2k} \sigma^2 (w_N) + (\delta/\beta)^2 \sum_{i=1}^k (\alpha/\beta)^{2(k-i)} \times [\sigma^2 (D_{N-i}) + \sigma^2 (D_{N-i+1})]. \quad (B2)$$

Since the covariances of  $D$  estimates at adjacent levels will usually be positive, they will only augment the effect of the variances of divergence and may be overlooked in this discussion. Typically  $\alpha < 1$  while  $\beta > 1$ , so that  $\alpha/\beta < 1$  while  $\beta/\alpha > 1$ . We first consider  $\sigma^2 (w_1) \sim \sigma^2 (w_N)$  and  $\sigma^2 (D) = 0$ . For upward integration the variance increases from its boundary value in the direction of integration, and downward integration results in smaller errors than upward integration. If the upper boundary condition is poorly estimated and  $\sigma^2 (w_N) \gg \sigma^2 (w_1)$ , this conclusion is likely to be invalid. In the case of significant divergence error, vertical integration accumulates error although at a lesser rate for downward as opposed to upward integration. Vertical profiles of  $w$  error variance as computed from Eqs. (B1) and (B2) are presented in Fig. B.1. The divergence error variances are the central grid-point values obtained from upward integration (Fig. B.1a) and downward integration (Figs. B.1b and c). Radar observation uncertainty

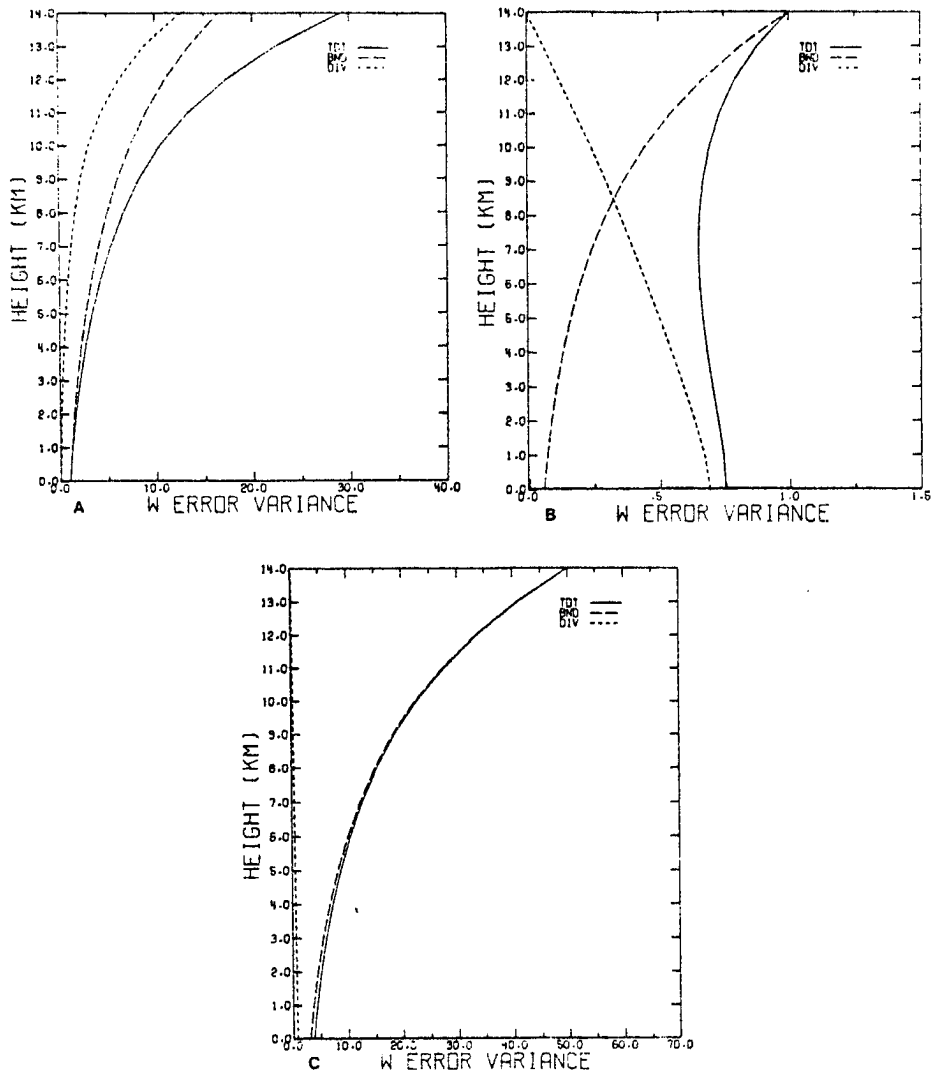


Fig. B.1. Vertical profiles of  $w$  error variance. Random errors in horizontal divergence are derived from two-radar analysis (curve labeled DIV) while uncertainty of boundary condition (curve labeled BND) is specified. Total  $w$  error variance profile (TOT) is sum of profiles DIV and BND. (A) error profiles for upward integration, with  $\sigma^2 w_1 = 1 \text{ m}^2 \text{ s}^{-2}$ ; (B) for downward integration; (C) as in Fig. B.1B,  $\sigma^2 w_N = 50 \text{ m}^2 \text{ s}^{-2}$ . From Ray et al. (1980)

is the only source of random error included. Contributions to the total variance (TOT) by the first and second right-hand side terms in Eqs. (B1) and (B2) are illustrated by curves labelled BND and DIV, respectively. In Fig. B.1a [ $\sigma^2 (w_1) = 1.0 \text{ m}^2 \text{ s}^{-2}$ ], the increase of variance with height is evident. The accumulation of divergence error during vertical integration is significant, and should be allowed for in subsequent adjustments. For downward integration with  $\sigma^2 (w_N) = 1.0 \text{ m}^2 \text{ s}^{-2}$  (Fig. B.1b), boundary error decreases with decreasing height while divergence error accumulates at a decreasing rate. The total error has a minimum in mid-levels. Thus, accumulation of divergence error is significant. For downward integration with  $\sigma^2 (w_N) = 50.0 \text{ m}^2 \text{ s}^{-2}$ , which may apply to an upper boundary within a penetrating or collapsing storm top (Fig. B.1c), boundary error dominates divergence error. With an expanded error specification, the divergence errors would be significant at low levels as illustrated in Fig. B.1b.

It can be concluded that  $w$  estimates obtained by downward integration are likely to have the least error. Minimizing the  $w$  error variance is particularly important for the iterative solution of Eq. (3.8) in the text. Here errors in horizontal divergence are linearly related to the horizontal variability of the  $w$  estimate.